Materials & Design 257 (2025) 114354

Contents lists available at ScienceDirect

Materials & Design

journal homepage: www.elsevier.com/locate/matdes

Reshaping anisotropic behavior in metallic sheets under complex stress states: Symmetric and asymmetric polynomial models with advanced convexity analysis approach

Yanqiang Ren [a], Kai Du [a,c,*], Yong Hou [d,*], Liying Song [e], Liang Sun [a], Yanfeng Yang [f], Wentao Zheng [a,c,*], Xiaoguang Yuan [b,c]

[a] School of Materials Science and Engineering, Shenyang University of Technology, Shenyang 110870, China
[b] Liaoning Vocational University of Technology, Jinzhou 121007, China
[c] Shenyang Key Laboratory of Precision Forming and Intelligence for Complex Components, Shenyang 110870, China
[d] Institute of Forming Technology and Lightweight Components (IUL), TU Dortmund University, Dortmund 44227, Germany
[e] School of Mechanical and Power Engineering, Shenyang University of Chemical Technology, Shenyang 110142, China
[f] State Key Lab of Solidification Processing, School of Materials Science and Engineering, Northwestern Polytechnical University, Xi'an 710072, China

ARTICLE INFO

Keywords:
Yield criterion
Analytical calibration
Convexity analysis
Non-associated flow rule
Subsequent yielding
Sheet metal forming

ABSTRACT

Fourth-order polynomial-related analytical symmetric and asymmetric anisotropic yield criteria under the non-associated flow rule, are proposed to cover a wider range of stress states. The new model can be directly calibrated using selected experimental data. Additionally, a modified geometry-inspired numerical convexity proof method is developed to demonstrate that the proposed model satisfies the convexity condition. Compared the newly proposed and existing advanced convexity proof methods and yield criteria, and evaluated the applicability and effectiveness of the new framework. The results indicate that the new convexity proof method provides highly accurate convexity identification, consistent with the Hessian matrix method, while maintaining the user-friendliness of the GINCA method. The new symmetric model exhibits the highest accuracy in characterizing the plastic anisotropy of DP490 and AA6016-T4 compared to other investigated yield criteria. Furthermore, the new asymmetric model effectively predicts the strength differential effect under complex stress states. Precise modeling of near-plane strain and pure shear stress states significantly enhances the characterization of stress states in tensile-tensile and tension–compression regions. Applying the anisotropic hardening concept enables continuous capture of the subsequent yielding behavior of metallic sheets.

1. Introduction

Lightweight and high-performance metallic sheets are widely used in the automotive and aerospace industry to replace cast iron and conventional steel [1,2]. This substitution not only reduces fuel consumption, CO_2 emissions, and environmental pollution but also enhances crash safety, recyclability, and braking performance [3]. However, polycrystalline structured metallic sheets typically exhibit significant anisotropic yield and plastic flow behavior due to their complex thermal processing history [4]. To achieve accurate analysis of sheet metal forming processes and facilitate engineering applications, precise characterization of the plastic deformation behavior of metallic sheets based on phenomenological yield criteria has become essential [5]. Sheet metals are often subjected to various stress states during plastic forming [6], such as uniaxial tension (UT), equi-biaxial tension (e-BT), near-plane strain (NPS), simple shear (SS), and uniaxial compression (UC), as illustrated in Fig. 1. The diverse nature of these forming conditions necessitates that constitutive models accurately describe anisotropy, tension–compression asymmetry, and differential hardening behavior over a wide range of stress states, posing an ongoing challenge [7]. Consequently, to pre-evaluate the forming process of components and shorten the development cycle through virtual manufacturing technology, it is necessary to establish high-fidelity anisotropic yield criteria that cover a broader range of stress states.

To date, numerous yield criterion modeling methods have been developed to characterize the plastic anisotropy of materials. The most famous yield criterion is the quadratic Hill48, which introduces aniso-

* Corresponding authors at: School of Materials Science and Engineering, Shenyang University of Technology, Shenyang 110870, China (K. Du and W.T. Zheng); Institute of Forming Technology and Lightweight Components (IUL), TU Dortmund University, Dortmund 44227, Germany (Y. Hou).
E-mail addresses: dukai@sut.edu.cn (K. Du), Yong.Hou@iul.tu-dortmund.de (Y. Hou), wtzheng@alum.imr.ac.cn (W. Zheng).

https://doi.org/10.1016/j.matdes.2025.114354
Received 4 March 2025; Received in revised form 6 June 2025; Accepted 4 July 2025
Available online 16 July 2025

Nomenclature

AFR	**A**ssociated **f**low **r**ule
BCC	**B**ody-**c**entered **c**ubic
DD	**D**iagonal **d**irection
DPSR	**D**irection of **p**lastic **s**train **r**ate
DP-YL	**Y**ield **l**ocus in the **d**iagonal **p**lane
e-BC	**E**qui-**b**iaxial **c**ompression
e-BT	**E**qui-**b**iaxial **t**ension
EPS	**E**quivalent **p**lastic **s**train
FCC	**F**ace-**c**entered **c**ubic
GINCA	**G**eometry-**i**nspired **n**umerical **c**onvex **a**nalysis
HCP	**H**exagonal **c**lose-**p**acked
NAFR	**N**on-**a**ssociated **f**low **r**ule
NPS	**N**ear-**p**lane **s**train
NP-YL	**Y**ield **l**ocus in the **n**ormal **p**lane
PPF	**P**lastic **p**otential **f**unction
RD	**R**olling **d**irection
SD	**S**trength **d**ifferential
SS	**S**imple **s**hear
TD	**T**ransverse **d**irection
UC	**U**niaxial **c**ompression
UT	**U**niaxial **t**ension
VPSC	**V**isco-**P**lastic **S**elf-**C**onsistent
YSF	**Y**ield **s**tress **f**unction

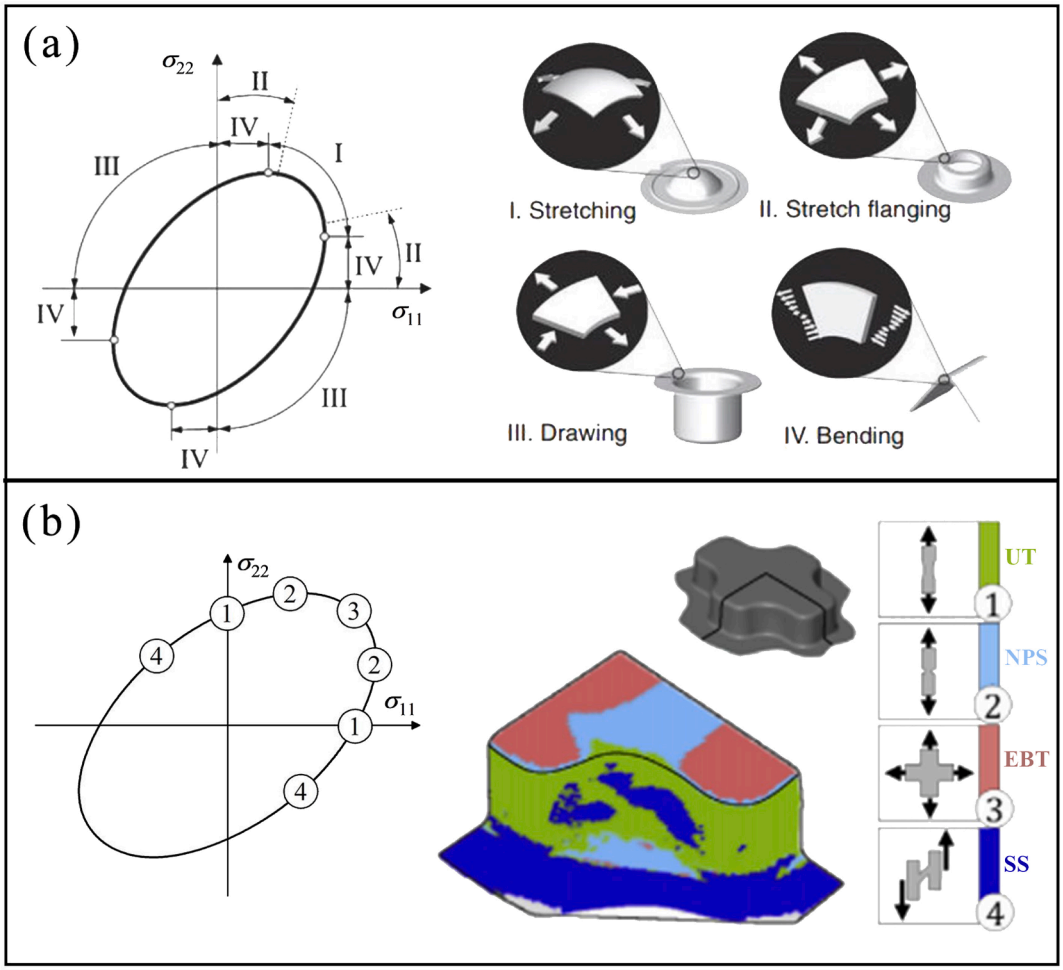

Fig. 1. Typical stress states of (a) sheet metal [8], (Copyright 2014, Elsevier), and (b) deep drawing of a cross-cup [9], (Copyright 2018, Elsevier).

tropic coefficients into the von Mises isotropic yield criterion. Due to its simplicity in parameter identification and low calibration cost, Hill48 remains widely used in finite element analysis for steel sheets. Gotoh et al. [10] further extended Hill48 to fourth-order (Gotoh77). The Gotoh77 yield criterion employs a comprehensive set of nine anisotropic coefficients, achieving enhanced precision in characterizing the in-plane anisotropic plastic deformation behavior of sheet metals. Banabic et al. [11,12] developed a series of BBC family yield criteria by adding weighting factors to the Hershey 1954 isotropic yield criterion, significantly improving the description ability of the yield function for aluminum alloy sheets. In contrast to extending isotropic yield criteria by introducing material parameters, Barlat et al. [13] proposed the classical Yld2000-2d yield criterion using two linear transformations on the Cauchy stress tensor. However, due to the limited *r*-value anisotropic data used for calibration, it usually fails to predict the six or eight-earing phenomena during deep drawing tests. To further enhance the characterization of materials with strong in-plane anisotropy, Barlat and collaborators (Barlat et al. [14] & Aretz and Barlat [15]) developed Yld2004-18p and Yld2011-27p using the linear transformation method, effectively enhancing the flexibility of the yield function. Cazacu and

Barlat [16] proposed a yield criterion associated with the second (J_2) and third (J_3) invariants of stress deviator. Cazacu [17] extended the stress invariant-related isotropic yield criterion to anisotropy based on the theory of the representation of tensor functions. Notably, yield criteria associated with stress invariants can significantly reduce the computational cost by 20–40 % during numerical simulations compared to criteria based on the linear transformation method [18]. Another interesting modeling method constructs yield surfaces through geometric relationships. Vegter et al. [19] developed an anisotropic yield criterion under plane stress conditions using quadratic Bezier curve interpolation. Peng et al. [20] proposed constructing the yield locus in the normal plane based on Hermite interpolation. Although geometric methods are easier to implement for satisfying convexity conditions, they often do not fully consider data related to the shear stress component of the deviatoric stress tensor, limiting their application depth. Lee et al. [21] proposed the CQN2017 yield criterion under the non-associated flow rule (NAFR), coupling quadratic anisotropic and non-quadratic isotropic yield criteria. The anisotropic part captures the anisotropic hardening (AH) behavior, while the isotropic part controls yield surface curvature. Moreover, the YSF and PPF of CQN2017 independently characterize the anisotropic yield and plastic flow behavior of sheet metals, respectively. Hu et al. [22] replaced the anisotropic part of the CQN2017 with the Poly4 yield criterion, further extending the coupled-type yield criteria to describe materials with highly plastic anisotropy under the associated flow rule (AFR).

Although the aforementioned modeling methods can accurately characterize the plastic behavior of materials under UT and e-BT stress states, most yield criteria struggle to effectively describe the anisotropic response properties dominated by NPS, SS, and UC stress states. Considering that these typical loading conditions significantly influence the plastic forming process and the quality of the finished components, a review of existing research will be presented, focusing on NPS, SS, and UC stress states.

1.1. Near-plane strain (NPS) stress state

NPS stress state plays a crucial role in many sheet metal forming processes. For instance, automotive body panels are subjected to NPS during stretching [23] and flanging [24]. NPS is also prevalent in roll bending [25], skin pulling [26], and hole expansion tests [27]. In addition, NPS is the main strain path for metallic sheets entering the necking stage [28], relating to the lowest principal strain point on forming limit curves [29,30] and the highest principal stress point on yield loci [31]. Therefore, understanding the plastic anisotropy under NPS loadings is critical. To optimize the description ability of yield criteria using NPS experimental data, various measurement methods have been proposed. The plane strain tensile test is a convenient method to obtain work-hardening properties under NPS loadings by clamping specimens with different notch sizes on an electronic universal testing machine [32]. However, edge effects in notched specimens may cause stress calculation deviations [33], which can be mitigated by pre-evaluating the specimen geometry using finite element simulation. Another common method is biaxial tensile testing of cruciform specimens to measure biaxial hardening relationships [34,35]. To understand the plastic response at higher strain levels, the strength of cruciform arms can be enhanced by laser deposition [36] or by thinning the central area of the specimen. Kuwabara and Sugawara [37] developed a novel method to measure the directions of plastic strain rate (DPSRs) and yield stresses under large plastic strains using a multiaxial tube expansion test. Given that pre-deformation is introduced during specimen preparation, work-hardening behavior in the small strain stage needs to be derived from cruciform biaxial tension tests as a standard. In the last decade, calibrating yield criteria with NPS data to achieve better modeling accuracy has gained attention. Izadpanah et al. [38] accurately described the anisotropic yield behavior of AA3105, AA5XXX, and AlMgSi sheets by using NPS yield stress instead of e-BT properties to calibrate the BBC2003 and Yld2000-2d criteria. Considering the generalized plane strain constraint on plastic flow in FCC and BCC materials [39], Lee et al. [40] extended the parameter identification strategy using plastic strain ratios under NPS loadings, successfully reproducing phenomena such as local thinning and crack initiation in mild steel specimens. Since the e-BT stress state is located at the “tip of the nose” on the yield surface, it is critical to accurately characterize the plastic anisotropy, especially for materials with strong anisotropy [41]. They designed six calibration procedures for the BBC2008 to ensure the simultaneous calibration of NPS and e-BT data. The concept has been recognized in recent modeling reports, either by using NPS data to directly identify the anisotropic coefficients [42,43] or by optimizing exponents or weighting factors of the shape control term [44,45]. In addition, Hakoyama et al. [46] found that NAFR is more accurate than AFR yield criterion in describing the deformation process of 6000 series aluminum alloy sheets under NPS stress state.

1.2. Simple shear (SS) stress state

In the deep drawing test of cylindrical parts, the flange region primarily experiences shear loadings [8]. Similar shear-dominated stress states are observed in tube hydroforming with axial feeding. For example, Hu et al. [47] found that three typical cells on a tubular specimen were subjected to shear stresses during the forming process. Given the significant influence of mechanical properties under shear loadings on plastic forming, it is essential to pay close attention to the typical SS stress state to achieve overall characterization accuracy. Modeling the yield criterion can be seen as interpolating the yield loci (or 3D yield surface) of sheet metals using experimental sampling points [41]. In the orthogonal anisotropic framework, the SS stress state is centrally located in the shear region on the yield surface. It plays a critical role in controlling the width of the yield surface (SS45: SS yield stress along the diagonal direction (DD)) and the height of the yield surface (SS0: SS yield stress along the rolling direction (RD)). Therefore, accurately determining mechanical properties under SS stress states is crucial for adjusting the yield surface shape. To obtain mechanical properties under SS stress states, in-plane shear tests based on ASTM specimens are often used [48]. Although ASTM specimens tend to rotate during testing, this can be mitigated by designing appropriate fixtures to apply sufficient clamping force [49]. The double shear test, as mentioned by Panchal et al. [50], effectively reduces specimen rotation and stress concentration at the edges due to its slit design. However, different rotations in the principal stress direction in the two shear zones can lead to incomplete representation of anisotropic behavior [51]. The in-plane torsion test is another popular measurement method for obtaining SS test data but struggles to capture anisotropic properties under SS loadings[52]. Brosius et al. [53] and Panchal et al. [50] employed a double-bridge shear test to accurately measure SS mechanical properties of anisotropic materials, although this method involves a complex testing procedure and higher costs compared to ASTM in-plane shear tests. The accuracy of macro-phenomenological constitutive models is strongly influenced by the input mechanical properties during calibration [54]. To address this, Hou et al. [55] developed the CQI2022 yield criterion, which effectively controls the yield locus curvature by calculating the shape control parameter c through an error minimization function associated with SS and NPS experimental data. However, using test data from multiple stress states to identify c results in imprecise SS stress state predictions. Lou et al. [56] developed a plasticity model that accurately predicts the SS stress state based on J_2 and J_3. However, this approach neglects the importance of the e-BT stress state in shaping the yield surface. He et al. [57] proposed the EYld2000-2d yield criterion, based on Yld2000-2d, which significantly improved prediction accuracy in the second and fourth quadrants of the yield locus after SS loadings calibration. Due to the complexity of calibrating anisotropic coefficients in linear transformation yield criteria, accurately characterizing the distortion hardening behavior remains

challenging. To address this, Du et al. [58] developed the Analytical Poly6 II-2 yield criterion, using SS0 yield stress for analytical calibration of anisotropic coefficients. However, this model did not fully consider plastic anisotropy under SS stress, limiting its ability to control yield surface width variation effectively. To compensate, Hu et al. [47] proposed the Analytical Poly6-18p yield criterion, which controls both yield surface width and height after calibration with SS0 and SS45 data. Hou et al. [59] developed a comprehensive plasticity framework to simulate complex plastic behavior, with a particular focus on capturing the plastic anisotropy under SS in sheet metal materials. Meanwhile, Sun et al. [60] proposed a yield criterion that significantly improved the accuracy of describing SS load based on an exponential assignment strategy. Recently, Du et al. [61] proposed a coupled yield criterion that breaks the specific correspondence between SS and NPS.

1.3. Uniaxial compression (UC) stress state

UC stress state is a primary loading condition on the concave surfaces of sheet metals, especially as they flow through the rounded corners of forming tools [8]. This stress state is critical for capturing the strength differential (SD) effect observed in many engineering materials such as quenching and partitioning steels [62], aluminum alloys [63], magnesium alloys [64], and titanium alloys [65,66]. Accurately characterizing the asymmetric plastic deformation behavior of strongly anisotropic materials through UC tests is essential for experimental plasticity. During UC tests, normal lateral pressure is typically required in the thickness direction of the specimen to prevent buckling. The additional friction and biaxial effects introduced into the measurement system can be corrected using data processing methods, such as those proposed by Joo et al. [67] and Yang et al. [68]. Lou et al. [69] incorporated the pressure effect into a symmetric yield criterion, developing a hydrostatic pressure-dependent asymmetric yield criterion. However, yield criteria based on the first stress invariant (I_1) generally only describe the SD effect along the RD and the transverse direction (TD). To improve the accuracy of asymmetric yield criteria in characterizing anisotropic behavior under UC stress state, Cazacu and Barlat [70] modified the Drucker1949 yield criterion from an even function to an odd function, establishing an asymmetric anisotropic yield criterion based on J_2 and J_3 through the theory of representation of tensor functions. Hu et al. [42] proposed an asymmetric yield criterion incorporating more material parameters based on three stress invariants ($I_1 - J_2 - J_3$), enhancing the description accuracy of plastic anisotropy under UC loading. In addition, Hu et al. [71] developed a polynomial form yield function, converting the $I_1 - J_2 - J_3$ framework into a stress triaxiality, normalized third stress invariant, and equivalent stress ($\eta - \xi - \overline{\sigma}$) framework, and verified the flexibility of the model by comparing the predicted yield locus with the visco-plastic self-consistent (VPSC) model. Yield criteria based on the linear transformation method of the Cauchy stress tensor also provide good description accuracy for the asymmetric anisotropic behavior of sheet metals. Plunkett et al. [72] extended the anisotropic yield function proposed by Cazacu et al. [73] to develop the CPB06ex2 asymmetric yield criterion, accurately predicting the behavior of hexagonal close-packed (HCP), face-centered cubic (FCC), and body-centered cubic (BCC) crystal structures. Distinct from the above, Park et al. [74] developed asymmetric yield stress functions based on ξ and η, respectively, considering the SD effect, anisotropic yield, and distortional hardening of materials at different temperatures and equivalent plastic strain (EPS) levels. Hou et al. [31] proposed the CFI2023 asymmetric yield criterion under NAFR, which couples a polynomial function and stress invariants, but this model could only describe UC yield stresses under RD and TD. To address this limitation, Zhou et al. [75] developed the ZHC2023 anisotropic yield criterion under NAFR, capable of predicting the SD effect of sheet metals and accurately describing UC loading along the DD. Furthermore, Lou et al. [4] extended the quadratic Hill48 yield criterion by incorporating a normalized third stress invariant correlation weight factor, proposing the Lode angle correlation anisotropic asymmetric LAA2023 yield criterion. However, the weighting factor in LAA2023 poses challenges in satisfying the convexity theorem. To overcome this, Hou et al. [76] developed a novel form of a general modeling framework for asymmetric yield models, suggesting the use of a η−dependent fifth-order polynomial function to describe the variation of the weighting factor, thus achieving the convexity requirement of the yield function. Based on the above literature review, it is concluded that none of models to date can simultaneously provide an accurate prediction of the deformation behavior including yield stress and plastic flow under all six stress states in Table 1.

Table 1
The incorporated stress states in the parameter identification of various yield criteria.

Yield criteria	Stress states for parameter identification					
	UT	EBT	NPS	SS	UC	EBC
Hill (1948)	√	×	×	×	×	×
Barlat et al. (2003) [13]	√	√	×	×	×	×
Banabic et al. (2005) [12]	√	√	×	×	×	×
Cazacu et al. (2006) [73]	√	√	×	×	√	×
Soare et al. (2008) [77]	√	√	×	×	×	×
Min et al. (2016) [78]	√	√	√	×	×	×
Lee et al. (2017) [21]	√	√	√	×	×	×
Hu et al. (2021) [79]	√	√	×	×	√	√
He et al. (2022) [57]	√	√	√	√	×	×
Lou et al. (2023) [4]	√	√	×	×	√	√
Hou et al. (2024) [59]	√	√	√	√	×	×
Sun et al. (2025) [60]	√	√	√	√	×	×
Du et al. (2025) [61]	√	√	√	√	×	×
The newly proposed model	√	√	√	√	√	√

The yield criterion must satisfy the convexity theorem to ensure a one-to-one relationship between the stress state and the ratio of plastic strain rate [80]. This requirement is crucial for solving elastoplastic constitutive equations using regression mapping algorithms [81]. While accurate characterization of stress states using various modeling methods is essential, examining the convexity of the yield function is equally critical. Yield criteria modeled through linear transformations of the stress tensor typically satisfy the convexity condition naturally. However, this is not always the case for models based on polynomials, couplings, and tensor function representation theories. Therefore, demonstrating convexity effectively during the development phase of the yield criterion is necessary. Although convexity can be determined from eigenvalues, deriving these for complex yield criteria can be challenging due to the lack of explicit forms for the eigenvalues in some cases [74]. A more straightforward method involves verifying convexity using the principal minors of the Hessian matrix, a widely used approach [58]. According to Tong [82], the Hessian matrices satisfy the semi-positivity requirement (and thus convexity) if all possible principal minors (not just the sequential ones) are non-negative. Raemy et al. [83] demonstrated convexity by multiplying the principal curvatures (Gaussian curvature) at any point of the yield surface. However, all these methods rely on second-order partial derivatives of the stress components, making convexity proof increasingly complex as the yield function becomes more intricate. To address this complexity, Lou et al. [84] proposed a geometry-inspired numerical convex analysis (GINCA) method, which avoids complex numerical operations. Despite its simplicity, GINCA may struggle to identify partially concave surfaces in high-order polynomial yield criteria, indicating the need for further refinement. In summary, although various methods have been proposed to prove the convexity of yield surface, existing approaches face challenges related to complicated formula derivation or unclear identification results. Developing a concise and accurate convexity identification method remains a significant challenge in the field.

In this work, new fourth-order polynomial-based analytical symmetric and asymmetric anisotropic yield criteria under NAFR are established to accurately describe plastic anisotropy and SD effects across a broader range of stress states (**Section 2**). In addition, a newly

modified geometry-inspired numerical convex analysis method is developed to verify that the yield and plastic potential surfaces predicted by the new model meet convexity requirements, as shown in Section 3. To ensure unique calibration results, an analytical procedure for calibrating both the yield stress function (YSF) and plastic potential function (PPF) of the new model is provided (Section 4). The new symmetric (Section 5) and asymmetric models (Section 6) are applied to dual-phase steel DP490 and aluminum alloy AA6016-T4 to validate performance. Comparative assessments are conducted against advanced symmetric yield criteria (NAFR-Poly4, EYld2000-2d, and AFR-Poly6) and asymmetric criteria (CFI2023, LAA2023, and ZHC2023), focusing on yield loci in the normal (NP-YLs) and diagonal planes (DP-YLs), DPSRs in both planes, and uniaxial yield stresses and *r*-values. The capability of the new models to describe the plastic anisotropy at various EPS levels is also thoroughly evaluated (Section 7).

2. New analytical symmetric and asymmetric anisotropic yield criteria under NAFR

In recent years, researchers have shown that including a wider range of stress states greatly improves the accuracy of numerical simulations [59,61]. However, as more loading conditions are incorporated, the mathematical complexity of these criteria increases, often necessitating optimization or interpolation methods to calibrate anisotropic coefficients effectively. However, the use of these methods comes with several drawbacks: (1) The yield and plastic potential surfaces are the inherent property of sheet metals. However, the anisotropic coefficients calculated using numerical optimization algorithms often yield different results, leading to varied yield or plastic potential surfaces, especially for advanced yield criteria. This non-unique solution violates the physical principle that the yield and plastic potential surfaces of a metal sheet should be unique [85]; (2) Unlike analytical methods, optimization techniques do not reliably yield exact values for anisotropic coefficients in a single computational process. Instead, they require multiple iterations, adjusting weighting factors each time to compute the coefficients [14]. Ultimately, the solution with the smallest error is selected as the final set of anisotropic coefficients. Additionally, these steps must be repeated at multiple EPS levels to accurately describe the evolutionary behavior. This calculation process is cumbersome, and the final solution based on minimizing error often introduces non-negligible inaccuracies; (3) To effectively characterize the distortion hardening behavior of materials at any EPS level, it is necessary to interpolate anisotropic coefficients at different EPSs. However, the accuracy of the interpolation is positively correlated with the number of EPS values used, which can lead to further prediction errors [86]; (4) Furthermore, optimization techniques often generate anisotropic coefficients that lack regularity across different EPS levels. As a result, the relationship curve between the anisotropic coefficients and EPS obtained through interpolation can introduce additional errors [87]. To date, there are no advanced yield criteria that incorporate strong anisotropic behaviors, broad stress states, and an analytical calibration strategy simultaneously.

To address above technical challenge, this section introduces a fourth-order polynomial-based analytical symmetric (**AS-Poly4**) anisotropic yield criterion and generalizes it to an asymmetric yield criterion (**AA-Poly4**). The YSF of the new asymmetric model was developed by coupling the asymmetric term of PSY2019 [74]. In addition, Lou et al. [4] proposed a modeling method for asymmetric PPF based on a weight factor, with the main advantage being that it retains the analytical parameter identification capability of the original function even after generalization. For this purpose, the PPF of the new asymmetric model is constructed by coupling two fourth-order polynomial functions through weight factor.

2.1. Analytical symmetric fourth-order polynomial yield criterion (AS-Poly4)

The newly proposed symmetric model developed based on the plane stress condition under the NAFR hypothesis, is expressed as follows:

$$F_{\text{Sym.}}(\boldsymbol{\sigma}) = f^{2/3}_{\text{Principal}}(\boldsymbol{\sigma}) + f_{\text{Shear}}(\boldsymbol{\sigma}) = \overline{\sigma}^4(\overline{\varepsilon}^{\text{p}}) \tag{1a}$$

with

$$f_{\text{Principal}}(\boldsymbol{\sigma}) = \kappa_1\sigma_{11}^6 + \kappa_2\sigma_{11}^5\sigma_{22} + \kappa_3\sigma_{11}^4\sigma_{22}^2 + \kappa_4\sigma_{11}^3\sigma_{22}^3 + \kappa_5\sigma_{11}^2\sigma_{22}^4 + \kappa_6\sigma_{11}\sigma_{22}^5 + \kappa_7\sigma_{22}^6 \tag{1b}$$

$$f_{\text{Shear}}(\boldsymbol{\sigma}) = \left(\kappa_8\sigma_{11}^2 + \kappa_9\sigma_{11}\sigma_{22} + \kappa_{10}\sigma_{22}^2\right)\sigma_{12}^2 + \kappa_{11}\sigma_{12}^4 \tag{1c}$$

where $\overline{\varepsilon}^{\text{p}}$ is an EPS; $\boldsymbol{\sigma}$ denotes the Cauchy stress tensor; $\sigma_{ij}(i,j=1,2)$ indicates the stress components of the stress tensor; $\kappa_i(i=1,2,\ldots,11)$ are anisotropic coefficients; $\overline{\sigma}$ is the effective stress, defined as the UT yield stress along the RD; To ensure the successful implementation of the analytical calibration strategy, the coefficients $\kappa_i(i=1,2,\ldots,7)$ can be identified using experimental sampling points in the normal plane, while the coefficients $\kappa_i(i=8,9,10,11)$ can be calculated using the mechanical properties associated with the non-zero shear stress component. Note that when $F_{\text{Sym.}}(\boldsymbol{\sigma}) < \overline{\sigma}^4(\overline{\varepsilon}^{\text{p}})$, material is in the elastic deformation stage, and the material is in the plastic deformation stage when $F_{\text{Sym.}}(\boldsymbol{\sigma}) = \overline{\sigma}^4(\overline{\varepsilon}^{\text{p}})$.

One of the reasons for successfully calibrating the anisotropic coefficients is that the YSF of the new symmetric model has the same and simple functional form as the PPF. It is worth noting that previous research has not reported any PPFs that facilitate both analytically calibrated anisotropic coefficients and accurate predictions of plastic flow behavior under complex loading conditions.

2.2. Analytical asymmetric fourth-order polynomial yield criterion (AA-Poly4)

In this study, the YSF of the new symmetric model is further extended to an asymmetric model. It consists of three components: (1) $g_{\text{Principal}}(\boldsymbol{\sigma})$ for controlling the NP-YL, (2) $g_{\text{Shear}}(\boldsymbol{\sigma})$ for regulating the yield surfaces associated with the shear stress component, and (3) $f_{\text{TC}}(\boldsymbol{\sigma})$ for describing the tension–compression asymmetry, as shown in Eq. (2).

$$F_{\text{Asym.}}(\boldsymbol{\sigma}) = \left[g^{2/3}_{\text{Principal}}(\boldsymbol{\sigma}) + g_{\text{Shear}}(\boldsymbol{\sigma})\right] f^4_{\text{TC}}(\boldsymbol{\sigma}) = \overline{\sigma}^4(\overline{\varepsilon}^{\text{p}}) \tag{2a}$$

with

$$g_{\text{Principal}}(\boldsymbol{\sigma}) = A_1\sigma_{11}^6 + A_2\sigma_{11}^5\sigma_{22} + A_3\sigma_{11}^4\sigma_{22}^2 + A_4\sigma_{11}^3\sigma_{22}^3 + A_5\sigma_{11}^2\sigma_{22}^4 + A_6\sigma_{11}\sigma_{22}^5 + A_7\sigma_{22}^6 \tag{2b}$$

$$g_{\text{Shear}}(\boldsymbol{\sigma}) = \left(A_8\sigma_{11}^2 + A_9\sigma_{11}\sigma_{22} + A_{10}\sigma_{22}^2\right)\sigma_{12}^2 + A_{11}\sigma_{12}^4 \tag{2c}$$

$$f_{\text{TC}}(\boldsymbol{\sigma}) = \exp[h(\boldsymbol{\sigma})I(\boldsymbol{\sigma})] \tag{2d}$$

with

$$h(\boldsymbol{\sigma}) = \frac{\left(\sigma_{11}^2 - \sigma_{11}\sigma_{22}\right)\chi_{\text{U0}} + 4\sigma_{12}^2\chi_{\text{U45}} + \left(\sigma_{22}^2 - \sigma_{11}\sigma_{22}\right)\chi_{\text{U90}} + \left(\sigma_{11}\sigma_{22} - \sigma_{12}^2\right)\chi_{\text{EB}}}{\overline{\sigma}^2_{\text{vM}}} \tag{2e}$$

$$\begin{cases} \chi_{\text{U}\alpha} = \ln\left|\dfrac{\text{UC}\alpha(\overline{\varepsilon}^{\text{p}})}{\text{UT}\alpha(\overline{\varepsilon}^{\text{p}})}\right|, \text{ for } \alpha = 0,\ 45,\ 90 \\ \chi_{\text{EB}} = \ln\left|\dfrac{\text{EBC}(\overline{\varepsilon}^{\text{p}})}{\text{EBT}(\overline{\varepsilon}^{\text{p}})}\right| \end{cases} \tag{2f}$$

$$I(\boldsymbol{\sigma}) \equiv I(L) = -1 \text{ or } 0 \text{ for } L = -1 \text{ or } 1 \tag{2g}$$

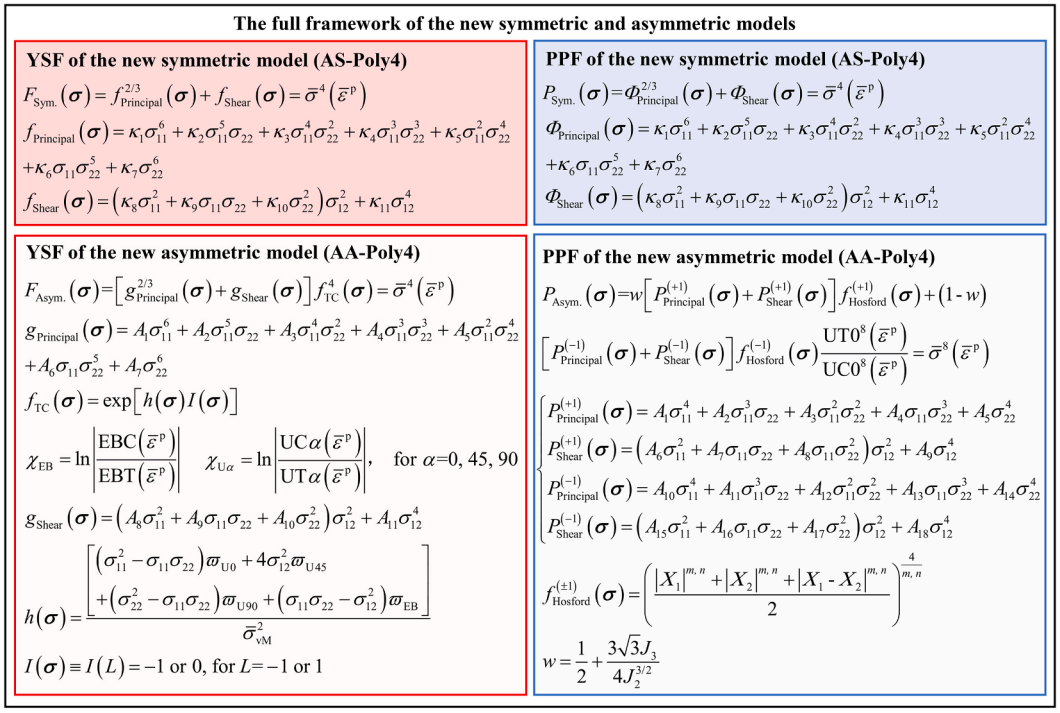

Fig. 2. The full framework of the new symmetric and asymmetric models.

where $A_i (i = 1, 2, \ldots, 11)$ is anisotropic coefficients; $\bar{\sigma}_{\mathrm{vM}}$ represents the normalized Mises equivalent stress; α is the angle to the RD; χ_{EB} and $\chi_{\mathrm{U}\alpha}$ are the tension–compression asymmetry coefficients associated with equi-biaxial loading and uniaxial stress states along the α angle to the RD, respectively; UTα and UCα represent yield stresses under UT and UC stress states along the α angle to the RD, respectively; EBT and EBC represent yield stresses under e-BT and e-BC, respectively; L is the Lode parameter, When L is expressed as a function related to η; $f_{\mathrm{TC}}(\boldsymbol{\sigma})$ will be identical to the asymmetric function proposed in PSY2019 [74].

Simultaneously, there is a research gap in PPFs that can effectively capture the complex anisotropic plastic flow behavior of metallic sheets under NAFR while ensuring an accurate description of the tension–compression asymmetry. To address this gap, the PPF of the new asymmetric model is further developed. The expression for the PPF of the new asymmetric model is shown as follows:

$$\begin{aligned} P_{\mathrm{Asym.}}(\boldsymbol{\sigma}) &= w\left[P^{(+1)}_{\mathrm{Principal}}(\boldsymbol{\sigma}) + P^{(+1)}_{\mathrm{Shear}}(\boldsymbol{\sigma})\right] f^{(+1)}_{\mathrm{Hosford}}(\boldsymbol{\sigma}) + \\ (1-w)&\left[P^{(-1)}_{\mathrm{Principal}}(\boldsymbol{\sigma}) + P^{(-1)}_{\mathrm{Shear}}(\boldsymbol{\sigma})\right] f^{(-1)}_{\mathrm{Hosford}}(\boldsymbol{\sigma}) \frac{\mathrm{UT0}^8(\bar{\varepsilon}^{\mathrm{p}})}{\mathrm{UC0}^8(\bar{\varepsilon}^{\mathrm{p}})} = \bar{\sigma}^8(\bar{\varepsilon}^{\mathrm{p}}) \end{aligned} \tag{3}$$

where UT0 and UC0 are the UT and UC yield stresses along the RD, respectively. $P^{(\pm1)}_{\mathrm{Principal}}(\boldsymbol{\sigma})$ and $P^{(\pm1)}_{\mathrm{Shear}}(\boldsymbol{\sigma})$ are written as

$$\begin{cases} P^{(+1)}_{\mathrm{Principal}}(\boldsymbol{\sigma}) = A_1\sigma_{11}^4 + A_2\sigma_{11}^3\sigma_{22} + A_3\sigma_{11}^2\sigma_{22}^2 + A_4\sigma_{11}\sigma_{22}^3 + A_5\sigma_{22}^4 \\ P^{(+1)}_{\mathrm{Shear}}(\boldsymbol{\sigma}) = \left(A_6\sigma_{11}^2 + A_7\sigma_{11}\sigma_{22} + A_8\sigma_{11}\sigma_{22}^2\right)\sigma_{12}^2 + A_9\sigma_{12}^4 \\ P^{(-1)}_{\mathrm{Principal}}(\boldsymbol{\sigma}) = A_{10}\sigma_{11}^4 + A_{11}\sigma_{11}^3\sigma_{22} + A_{12}\sigma_{11}^2\sigma_{22}^2 + A_{13}\sigma_{11}\sigma_{22}^3 + A_{14}\sigma_{22}^4 \\ P^{(-1)}_{\mathrm{Shear}}(\boldsymbol{\sigma}) = \left(A_{15}\sigma_{11}^2 + A_{16}\sigma_{11}\sigma_{22} + A_{17}\sigma_{22}^2\right)\sigma_{12}^2 + A_{18}\sigma_{12}^4 \end{cases} \tag{4}$$

where $A_i (i = 1, 2, \ldots, 18)$ are anisotropic coefficients. In addition, w in Eq. (3) is the weighting factor used to construct the LAA2023 asymmetric yield criterion reported in Lou et al. [4], with the following expressions:

$$w = \frac{1}{2} + \frac{3\sqrt{3}J_3}{4J_2^{3/2}} \tag{5}$$

Note that polynomial-type PPFs cannot always satisfy convexity, and the use of weighting factors will exacerbate the concave tendency of the plastic potential surface. Therefore, to facilitate satisfying the convexity requirement, Hosford curvature control functions are further incorporated into Eq. (3), as shown below:

$$f^{(\pm1)}_{\mathrm{Hosford}}(\boldsymbol{\sigma}) = \left(\frac{|X_1|^{m,n} + |X_2|^{m,n} + |X_1 - X_2|^{m,n}}{2}\right)^{\frac{4}{m,n}} \tag{6a}$$

with

$$X_{1,2} = \frac{\sigma_{11} + \sigma_{22}}{2} \pm \sqrt{\left(\frac{\sigma_{11} - \sigma_{22}}{2}\right)^2 + \sigma_{12}^2} \tag{6b}$$

where m and n are the exponents.

The complete analytical calibration procedures for the new symmetric and asymmetric models are elaborated in **Section 4**. To provide readers with an intuitive understanding of the NAFR plasticity model proposed in this work, Fig. 2 summarizes the complete framework of the new symmetric and asymmetric models.

3. A modified geometry-inspired numerical convexity analysis method with user-friendliness and high-fidelity

The convexity analysis of the yield criteria surface with a simple mathematical structure (such as the SY2004 and Poly4) is easily achieved using the traditional Hessian matrix method. However, for yield criteria with complex functional forms like Barlat91 and PSY2019, calculating the first-order and second-order partial derivatives is usually challenging. As a result, accurately determining whether these yield criteria strictly satisfy the convexity condition poses a significant challenge. In response, Lou et al. [84] proposed the geometry-inspired numerical convex analysis (GINCA) method, which introduced a pioneering approach to address this issue. While the GINCA method

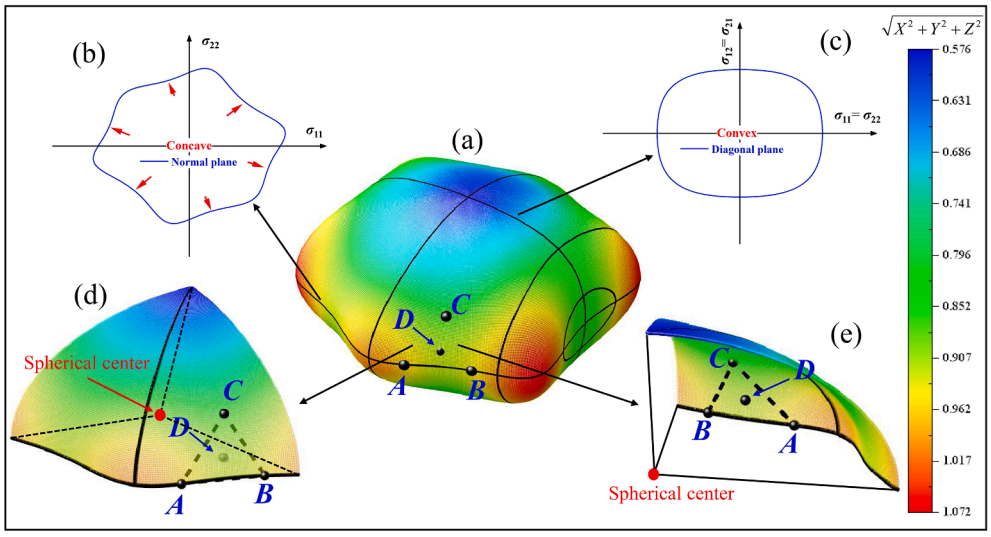

Fig. 3. (a) The 3D yield surface, (b-c) yield loci, and (d-e) partially enlarged images predicted by the new symmetric model when $\kappa_4 = 12.392$ and other anisotropic coefficients are kept in Mises condition.

provides relatively accurate convexity identification results for yield criteria such as CB2004 and Cazacu2018, it tends to over-describe the convex domain for polynomial yield criteria. Consequently, this section aims to delve into the reasons behind the ambiguous identification results from the GINCA method and propose a modified GINCA method.

3.1. Limitations of existing convexity proof methods

3.1.1. Hessian matrix method

The Hessian matrix stands out as the predominant method for validating the convexity of a yield criterion. It establishes the convexity of a yield surface by ensuring that the sequential principal minors of the Hessian matrix are strictly greater than 0, thus meeting the positive semidefinite condition. The Hessian matrix is mathematically defined as follows:

$$\boldsymbol{H} = \begin{bmatrix} H_{11} & H_{12} & H_{13} \\ H_{21} & H_{22} & H_{23} \\ H_{31} & H_{32} & H_{33} \end{bmatrix} = \begin{bmatrix} \frac{\partial^2 \Theta}{\partial\sigma_{11}\partial\sigma_{11}} & \frac{\partial^2 \Theta}{\partial\sigma_{11}\partial\sigma_{22}} & \frac{\partial^2 \Theta}{\partial\sigma_{11}\partial\sigma_{12}} \\ \frac{\partial^2 \Theta}{\partial\sigma_{22}\partial\sigma_{11}} & \frac{\partial^2 \Theta}{\partial\sigma_{22}\partial\sigma_{22}} & \frac{\partial^2 \Theta}{\partial\sigma_{22}\partial\sigma_{12}} \\ \frac{\partial^2 \Theta}{\partial\sigma_{12}\partial\sigma_{11}} & \frac{\partial^2 \Theta}{\partial\sigma_{12}\partial\sigma_{22}} & \frac{\partial^2 \Theta}{\partial\sigma_{12}\partial\sigma_{12}} \end{bmatrix} \tag{7}$$

where Θ is the YSF or PPF.

Although the accuracy of the Hessian matrix method for providing the convexity conditions of yield criteria is well established, there

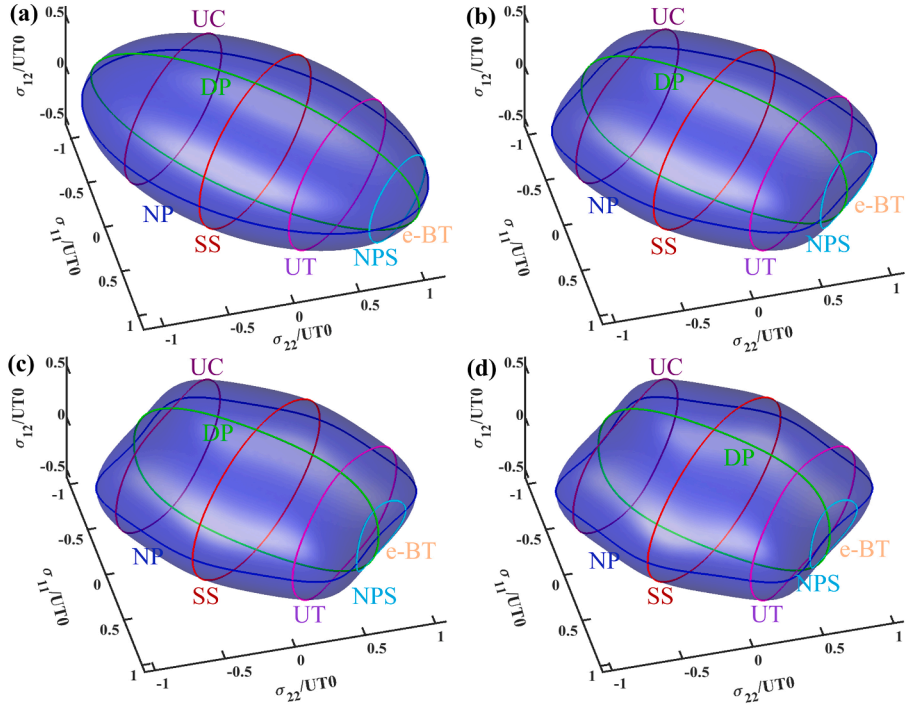

Fig. 4. Normalized 3D yield surfaces predicted using the new symmetric model with (a)κ_4 = -7, (b)κ_4 = -3, (c)κ_4 = 1, and (d)κ_4 = 5, which are taken within the convex domain described by the GINCA method, and the other anisotropic coefficients are maintained in the Mises isotropic condition.

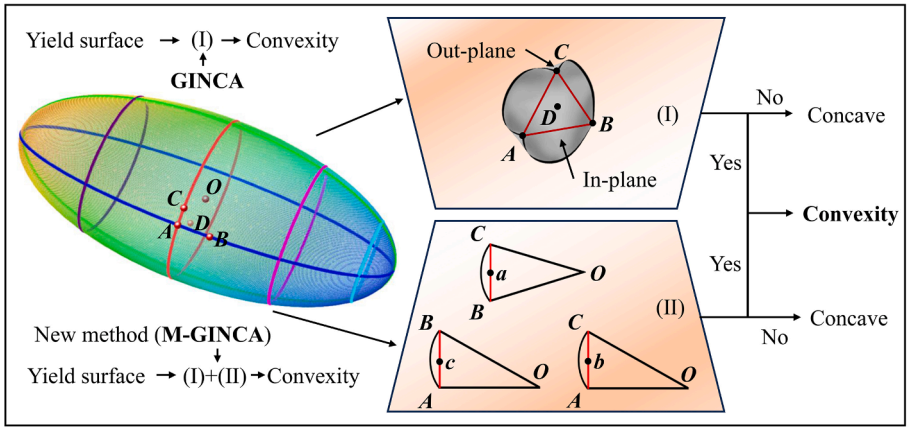

Fig. 5. The convexity proof process and principle of the GINCA and new convexity proof method.

remains a risk of failure when applying this method to certain complex yield criteria. Firstly, the Hessian matrix method can complicate the identification of convexity in the yield criteria with intricate functional expressions, as obtaining the second-order partial derivative information becomes extremely challenging. Secondly, the Hessian matrix method often struggles to verify the Hosford yield criterion, the Hosford coupled yield criteria, and higher-order exponential yield criteria similar to Lou et al. [18]. The results indicate that the smallest principal minor computed by the Hessian matrix method for these yield criteria, when satisfying the convexity condition, consistently falls within the interval [-1*10^{-16}, 0). This failure may stem from exceeding the double-precision range of the numerical analysis software, leading to floating-point errors that result in the smallest principal minor being less than zero.

3.1.2. GINCA method

Lou et al. [84] proposed the GINCA method to address the two failure types associated with the Hessian matrix method by calculating the normalized effective stress of the yield criterion. The theoretical basis of the GINCA method is described in detail. Fig. 3 illustrates the 3D yield surfaces, yield loci, and partially enlarged images predicted by the new symmetric model when $\kappa_4 = 12.392$ and other anisotropic coefficients are maintained in the Mises isotropic condition, i.e., $\{\kappa_1, \kappa_2, \cdots, \kappa_{11}\}$={1, - 3, 6, - 7, 6, - 3, 1, 6, - 6, 6, 9}. First, the side length δb of the triangle and the two angles θ and β in the spherical coordinate system is provided. Next, the coordinates of points $A(X_A, Y_A, Z_A)$, $B(X_B, Y_B, Z_B)$, and $C(X_C, Y_C, Z_C)$ are calculated using Eq. (8a). The coordinates of the midpoint $D(X_D, Y_D, Z_D)$ of the three points A, B, and C are then determined using Eq. (8b). Subsequently, the theoretical effective stress $\overline{\sigma}^{\text{cal.}}$ is calculated by applying the coordinates of point D to the yield function. Following this, the two angles θ and β are incremented by their respective step size δa to divide the yield surface into $64800/\delta a^2$ surfaces arc ABC, and the ranges of θ and β are $[0, 2\pi]$ and $[0, \pi]$, respectively. Finally, the yield surface satisfies the convexity requirement if all surfaces arc ABC fulfill the condition $\overline{\sigma}^{\text{cal.}} < 1$.

$$\begin{cases} X_A = \sin\theta\cos\beta \\ Y_A = \sin\theta\sin\beta \\ Z_A = \sin\theta \end{cases}; \begin{cases} X_B = \sin\theta\cos(\beta + \delta b) \\ Y_B = \sin\theta\sin(\beta + \delta b) \\ Z_B = \sin\theta \end{cases}; \begin{cases} X_C = \sin(\theta + \delta b)\cos\beta \\ Y_C = \sin(\theta + \delta b)\sin\beta \\ Z_C = \sin(\theta + \delta b) \end{cases} \tag{8a}$$

$$\begin{cases} X_D = (X_A + X_B + X_C)/3 \\ Y_D = (Y_A + Y_B + Y_C)/3 \\ Z_D = (Z_A + Z_B + Z_C)/3 \end{cases} \tag{8b}$$

The reasons for the failure of the GINCA method are analyzed next. Examining the local enlarged view of the surface arc ABC from two different viewpoints, it can be found that the midpoint D of the plane triangle $\overline{ABC}$ is inside the surface arc ABC, as shown in Fig. 3(d)-(e). According to the determination principle of the GINCA method, the yield surface should satisfy the convexity requirement. However, while the DP-YL satisfies the convexity requirement, the NP-YL exhibits an obvious concavity, as shown in Fig. 3(b)-(c). This demonstrates that the GINCA method incorrectly evaluates the concavity of the yield surface in the current state. The main reason is that arc ABC provides severe uneven concavity and convexity, with contribution of arc AB to concavity significantly outweighing arcs AC and BC, which leads to the failure of the GINCA method. Only by imposing convexity constraints on all three edges of arc ABC can the failure issue be resolved. To illustrate specific instances where the GINCA method fails, examples are provided based on the new symmetric model. Fig. 4 shows the normalized 3D yield surface predicted by the YSF of the new symmetric model when κ_4 assumes values within the convex domain determined by the GINCA method, while other anisotropic coefficients remain set to the Mises isotropic condition. When κ_4 is equal to -7 and -3, both the Hessian matrix (see Eq. (7)) and GINCA methods are effective in proving that the yield surface satisfies the convexity condition, as shown in Fig. 4(a)-(b). However, when κ_4 is equal to 1 or 5, only the Hessian matrix method provides accurate concave determination results. In contrast, the GINCA method overestimates the anisotropic coefficient, as shown in Fig. 4(c)-(d). Therefore, if there is strong concave-convex variability of the yield surface in different cross sections, it is usually not possible to prove convexity using the GINCA method. Thus, the GINCA method requires further refinement to address its limitations in verifying convexity, particularly when applied to polynomial yield criteria.

3.2. Development and validation of the new convexity proof method

A modified geometry-inspired numerical convexity analysis method (M-GINCA) is newly proposed to address limitations in convexity verification, particularly where the original GINCA and Hessian matrix methods may encounter challenges with certain yield criteria. This section details the foundational principles and procedural steps of the M-GINCA method, with Fig. 5 illustrating its recognition process and principle. Firstly, it must be ensured that the midpoint D of points A, B, and C on the yield surface lies within the interior of the surface arc ABC, i.e. the GINCA method (Condition I). Additionally, all line segments formed by points A, B, and C must be constrained to lie in-plane. This requires that the midpoints a, b, and c of the segments $\overline{AB}$, $\overline{BC}$ and $\overline{AC}$ satisfy $\overline{\sigma}^{cal.} < 1$ (Condition II). If both of these conditions are met, the new convexity proof method determines that the yield surface is convex (Condition I + II). Similarly, if all closely adjacent surfaces on the yield surface satisfy the convexity requirement, the new convexity proof method considers that the yield criterion strictly satisfies the convexity. In this study, yield surface convexity is identified by cutting the surface

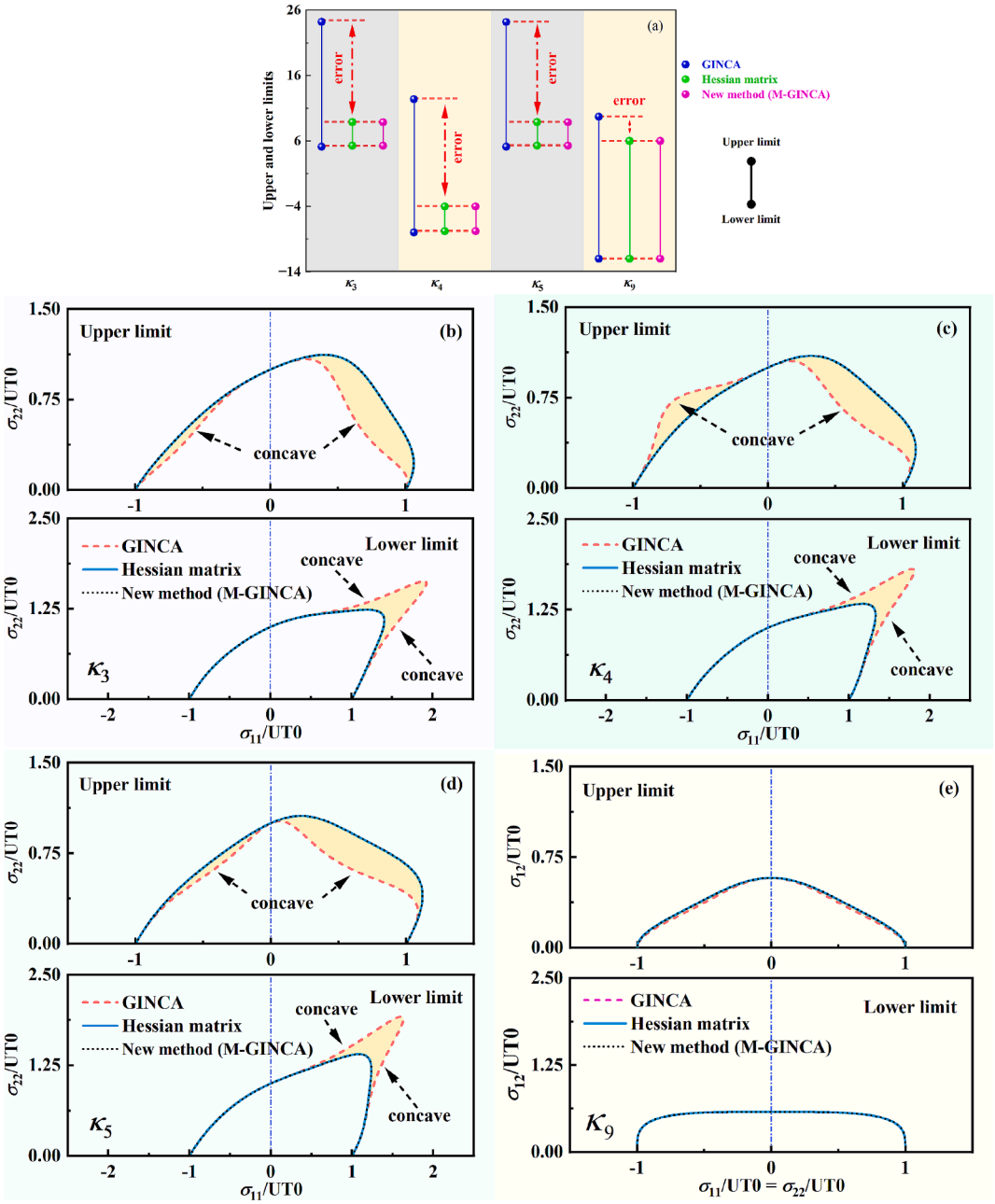

Fig. 6. (a)The upper and lower bounds of the anisotropic coefficients calculated by the Hessian matrix, GINCA, and new convexity proof methods, as well as the yield loci corresponding to the upper and lower bounds of (b)κ_3, (c)κ_4, (d)κ_5, and(e)κ_9.

at a one-degree interval ($\delta a = \pi/180$) and setting the δb to $\pi/18000$. Theoretically, further reducing δa and δb would increase the precision of the analysis. However, an excessively small δa can lead to a significant increase in computation time, and δb values below 0.01 can cause floating-point errors in numerical computation software, such as MATLAB, which potentially leading to incorrect recognition results. For this reason, this study recommends setting δa to $\pi/180$ or $\pi/90$, and choosing δb within the interval $[\pi/18000, \pi/1800]$ for optimal accuracy and efficiency.

To further verify the effectiveness and advancement of the new convexity proof method, this study calculates the upper and lower bounds of individual parameters that satisfy the convexity requirement and compares these results with two other methods. First, anisotropic coefficients $\kappa_i (i = 1, 2, \cdots, 11)$ are set to the Mises isotropic condition. Next, one anisotropic coefficient (κ_i) of the yield criterion is varied while holding the other anisotropic coefficients constant at the Mises isotropic condition. The convexity of the current anisotropic coefficients is then identified using the GINCA, Hessian matrix, and new convexity proof (M−GINCA) methods. Afterward, κ_i is incrementally adjusted, and convexity identification is repeated to determine the maximum (upper limit) and minimum (lower limit) values of κ_i that satisfy the convexity condition. Finally, this process is applied to each anisotropic coefficient to calculate their respective upper and lower limits.

Since the upper and lower bounds of all anisotropic coefficients exhibit similar trends, this study focuses on comparing only the bounds of $\kappa_i (i = 3, 4, 5, 9)$ as computed by the three convexity proof methods to verify the accuracy of the new M−GINCA method. If the upper and lower bounds calculated by either the GINCA or new convexity proof method align with those obtained from the Hessian matrix method, it confirms that the GINCA or new M−GINCA convexity proof method provides accurate convexity results. Conversely, discrepancies indicate an inability of the GINCA or new convexity proof method to accurately

Table 2
Experimental data used to calibrate the anisotropic coefficients of the new symmetric and asymmetric models.

Num.	Conditions	Stress components $(\sigma_{11}, \sigma_{22}, \sigma_{12})$
#1	UT0, r_{T0}	(UT0, 0, 0)
#2	UT30, r_{T30}	$\left(\frac{3}{4}\text{UT30}, \frac{1}{4}\text{UT30}, \frac{\sqrt{3}}{4}\text{UT30}\right)$
#3	UT45, r_{T45}	$\left(\frac{1}{2}\text{UT45}, \frac{1}{2}\text{UT45}, \frac{1}{2}\text{UT45}\right)$
#4	UT60, r_{T60}	$\left(\frac{1}{4}\text{UT60}, \frac{3}{4}\text{UT60}, \frac{\sqrt{3}}{4}\text{UT60}\right)$
#5	UT90, r_{T90}	(0, 0, UT90)
#6	UC0, r_{C0}	(- UC0, 0, 0)
#7	r_{C30}	$\left(-\frac{3}{4}\text{UC30}, -\frac{1}{4}\text{UC30}, -\frac{\sqrt{3}}{4}\text{UC30}\right)$
#8	UC45, r_{C45}	$\left(-\frac{1}{2}\text{UC45}, -\frac{1}{2}\text{UC45}, -\frac{1}{2}\text{UC45}\right)$
#9	r_{C60}	$\left(-\frac{1}{4}\text{UC60}, -\frac{3}{4}\text{UC60}, -\frac{\sqrt{3}}{4}\text{UC60}\right)$
#10	UC90, r_{C90}	(0, 0, − UC90)
#11	EBT, r_b	(EBT, EBT, 0)
#12	EBC	(− EBC, − EBC, 0)
#13	NPS0, ω_0	(NPS0, ρ_0NPS0, 0)
#14	NPS90, ω_{90}	(ρ_{90}NPS90, NPS90, 0)
#15	NPS45, ω_{45}	$\left(\frac{1}{2}(1+\rho_{45})\text{NPS45}, \frac{1}{2}(1+\rho_{45})\text{NPS45}, \frac{1}{2}(1-\rho_{45})\text{NPS45}\right)$
#16	SS45	(− SS45, SS45, 0)

Where $\rho_\alpha(\alpha = 0, 45, 90, r_b)$ represents the tensile load ratio of the NPS0, NPS45, NPS90, and EBT.

determine yield surface convexity. Fig. 6 shows the upper and lower bounds of anisotropic coefficients calculated by the Hessian matrix, GINCA, and new convexity proof methods, along with yield loci corresponding to these bounds for $\kappa_i(i = 3, 4, 5, 9)$. The yellow area represents the error of GINCA. The figure shows that the Hessian matrix and the new M−GINCA convexity proof methods have consistent upper and lower limits, while the upper bounds of the GINCA method deviate significantly, as seen in Fig. 6(a). Although the GINCA and Hessian matrix methods produce only minor numerical deviations for the lower limits, their corresponding yield loci do not overlap, as demonstrated in Fig. 6(b), 6(c), and 6(d). In addition, the GINCA method shows slight deviations in the upper and lower bounds associated with the shear stress component, as illustrated in Fig. 6(e). These findings confirm the accuracy of the new convexity proof method.

In summary, since the Hessian matrix method serves as the mathematic standard for assessing the convexity of yield criteria, the newly proposed convexity proof method, i.e., M−GINCA, that matches the capability of the Hessian matrix method is considered precise. In addition, both the GINCA and new M−GINCA methods are founded on the theoretical principles of geometric method, making the new method straightforward and avoiding the complex process of calculating the second-order partial derivatives. This indicates that the new convexity proof method effectively addresses the limitations of both the GINCA and Hessian matrix methods, offering user-friendly and high-fidelity convexity identification. Notably, the convexity identification time for all three methods is less than 1 s. Furthermore, the new convexity proof method is applicable beyond polynomial yield criteria. Ultimately, this method successfully verifies the convexity of all yield criteria analyzed in this study.

4. Analytical calibration procedure for anisotropic coefficients

Calibration procedures of anisotropic coefficients under the NAFR that incorporate both analytical solutions and a wide range of stress states have yet to be reported. While the traditional method of introducing additional UT mechanical properties improves the characterization accuracy of the yield criterion for in-plane plastic anisotropy, UT loadings cannot fully represent the range of properties required for manufacture, particularly in predicting the plastic response characteristics of sheet metals under complex loadings. This limitation suggests that the conventional strategy may be flawed. Moreover, the analytical identification procedure provides efficient and accurate plastic anisotropy prediction ability, avoiding the redundancy between anisotropic coefficients caused by optimization techniques and addressing the high dependence of interpolation techniques on strain intervals [86]. Therefore, the primary objective of this section is to ensure the explicit expression of the anisotropic coefficients of the new symmetric and asymmetric models, as well as to achieve an accurate description of anisotropic yield and plastic flow behaviors under complex loadings. Additionally, the reasonableness of the parameter calibration procedure is confirmed through a flexible analysis approach, ensuring that the yield criterion easily fulfills the convexity requirement.

Next, the experimental data utilized for the analytical calibration of the new symmetric and asymmetric models are presented. The YSF of the new symmetric model: UT$\alpha(\alpha = 0, 30, 45, 60, 90)$, EBT, NPS$\alpha(\alpha = 0, 45, 90)$, and SS45; The PPF of the new symmetric model: $r_{T\alpha}(\alpha = 0, 30, 45, 60, 90)$, r_b, and $\omega_\alpha(\alpha = 0, 45, 90)$; The YSF of the new asymmetric model: UT$\alpha(\alpha = 0, 30, 45, 60, 90)$, EBT, NPS$\alpha(\alpha = 0, 45, 90)$, SS45, UC$\alpha(\alpha = 0, 45, 90)$, and EBC; The PPF of the new asymmetric model: $r_{T\alpha}(\alpha = 0, 30, 45, 60, 90)$, r_b, $\omega_\alpha(\alpha = 0, 45, 90)$, and $r_{C\alpha}(\alpha = 0, 30, 45, 60, 90)$. Where the $r_{T\alpha}$ and $r_{C\alpha}$ represent the plastic strain ratios under UT and UC loadings, respectively. r_b is the r-value under e-BT stress state. NPSα and ω_α are the NPS yield stresses (maximum principal stress) and DPSRs along an angle α to the RD, respectively. The stress components under various loads can be calculated using the following stress coordinate transformation equation:

$$\begin{cases} \sigma_{11} = \sigma_{xx}\cos^2\alpha + \sigma_{yy}\sin^2\alpha - 2\sigma_{xy}\cos\alpha\sin\alpha \\ \sigma_{22} = \sigma_{xx}\sin^2\alpha + \sigma_{yy}\cos^2\alpha + 2\sigma_{xy}\cos\alpha\sin\alpha \\ \sigma_{12} = (\sigma_{xx} - \sigma_{yy})\sin\alpha\cos\alpha + \sigma_{xy}(\cos^2\alpha - \sin^2\alpha) \end{cases} \tag{9}$$

where σ_{xx}, σ_{yy}, and σ_{xy} are the stress components of loading coordinate system. Under biaxial tensile loading, the ratio of the minimum to maximum stresses of degree α along the RD is defined as ρ_α. In this work, due to the challenges associated with measuring plastic flow data under SS loading conditions, the SS stress state will be excluded from the determination of the anisotropic coefficients in the PPFs of the new symmetric and asymmetric models, in contrast to the loads utilized for

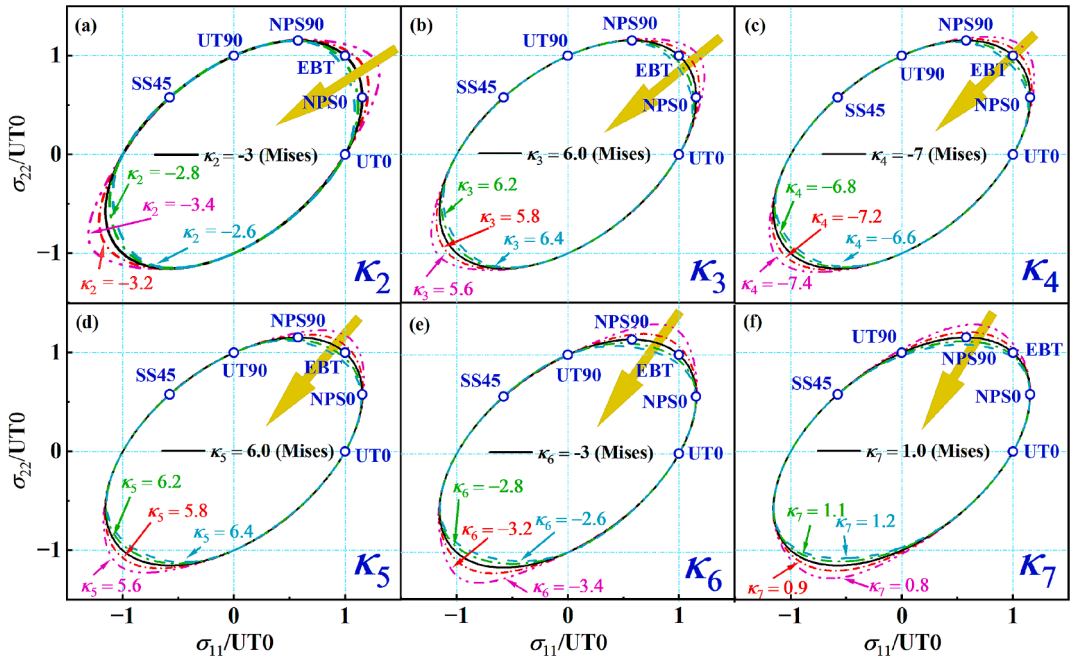

Fig. 7. Normalized NP-YLs predicted by the individual change of the anisotropic coefficients (κ_i) in the new symmetric model: (a) κ_2, (b) κ_3, (c) κ_4, (d) κ_5, (e) κ_6, and (f) κ_7.

the corresponding YSFs. Table 2 presents experimental data used to calibrate the anisotropic coefficients of the new symmetric and asymmetric models.

4.1. Selection of the convexity control parameter

Polynomial-type yield criteria often exhibit a concave tendency in their yield and plastic potential surfaces, posing a challenge in ensuring convexity compliance prior to calibration. While optimized calibration strategies can mitigate such challenges by controlling the range of values of the anisotropic coefficients, this approach is not applicable in the analytical parameter identification strategies. Alternatively, employing a convexity control parameter offers an effective means to enhance the convexity description ability of the yield criterion. When combined with analytical identification procedures, this approach yields explicit, unique, and optimum solutions suitable for fully automated numerical implementation [88]. In this section, the normal principal stress function $f_{\text{Principal}}(\boldsymbol{\sigma})$ of the YSF of the new symmetric model will be used as an example to outline a concise solution for enhancing convexity through flexibility analysis techniques.

The fundamental idea behind controlling the convexity of yield criterion involves selecting a specific anisotropic coefficient from $f_{\text{Principal}}(\boldsymbol{\sigma})$ as a convexity control parameter, therefore enabling the convexity description for various materials. Since κ_1 is a constant, κ_1 cannot be utilized as a convexity control parameter. The selection of an appropriate coefficient from the remaining set requires further exploration of their mapping relationship between typical yield points. Fig. 7 illustrates the normalized NP-YLs predicted by altering individual

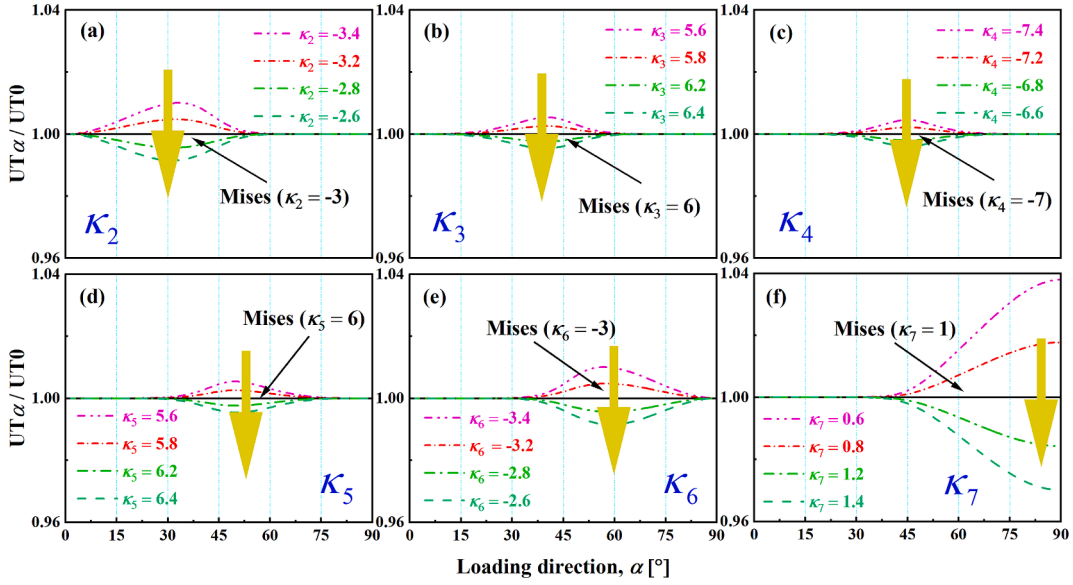

Fig. 8. Normalized UT yield stresses predicted by the individual change of the anisotropic coefficients (κ_i) in the new symmetric model: (a)κ_2, (b)κ_3, (c)κ_4, (d)κ_5, (e)κ_6, and (f)κ_7.

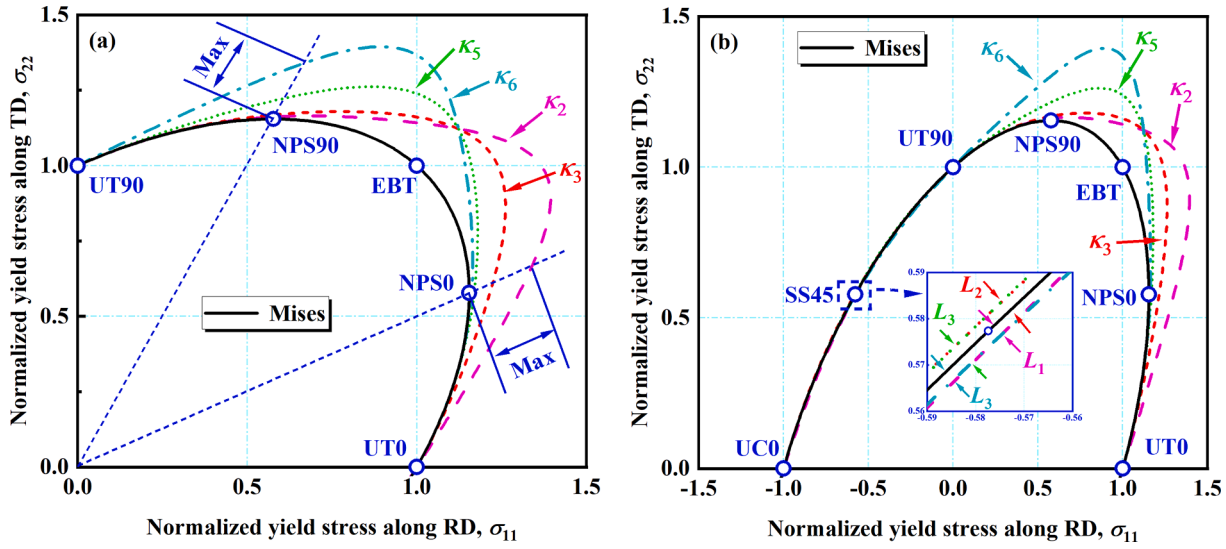

Fig. 9. The predicted normalized NP-YLs related to (a) NPS and (b) SS stress states when $\kappa_i(i=2,3,5,6)$ in the new symmetric model decreases by 0.4 on an isotropic basis.

anisotropic coefficients of the YSF of the new symmetric model. Note that the Mises isotropy condition is adopted when the anisotropic coefficients do not require adjustment. The position and direction of the yellow arrows indicate the region predominantly affected by the anisotropic coefficients and the trend with increasing coefficients, respectively. It is evident that κ_4 is most suitable for regulating the e-BT stress state (see Fig. 7(c)), while the curvature change between EBT and NPS0 is primarily influenced by κ_2 and κ_3 (Fig. 7(a)-(b)). In contrast, the effect of $\kappa_i(i=5,6,7)$ is observed in controlling the yield loci between EBT and NPS90, as shown in Fig. 7(d)-(f).

Given the unclear influence of $\kappa_i(i=2,3,5,6,7)$ in the normal principal stress function on the characteristic yield point, further observations on the role of different anisotropic coefficients in the normal plane-related UT loadings are necessary. Fig. 8 illustrates the normalized UT yield stresses predicted by individually altering the anisotropic coefficients of the YSF of the new symmetric model. Obviously, κ_7 has the most significant effect on UT90, as shown in Fig. 8(f), while $\kappa_i(i=2,3,5,6)$ primarily affects the UT yield stresses in the range of 30°-60° along the RD, independent of NP-YL (see Fig. 8(a)-(e)). Thus far, the alternative anisotropic coefficients that remain suitable as convexity control parameters are $\kappa_i(i=2,3,5,6)$. To determine the optimal choice among them, further comparative analysis is warranted.

Fig. 9 shows the predicted normalized NP-YLs when the $\kappa_i(i=2,3,5,6)$ of the YSF of the new symmetric model is decreased by 0.4 on an isotropic basis. It is evident that κ_2 exhibits a more flexible control of yield loci in the NPS0 region compared to κ_3. Similarly, the adjustment space of κ_6 for yield loci in the NPS90 region is significantly superior to κ_5. Obviously, κ_2 and κ_6 are more suitable for describing the plastic anisotropy under NPS loadings. To select the best convexity control parameter among the only two remaining coefficients, further observation of the influence regularity of κ_3 and κ_5 on the yield loci in the SS region is conducted. The results indicate that the distances L_1 and L_3 between the yield locus corresponding to $\kappa_i(i=3,5)$ and the Mises yield locus are almost the same, as shown in Fig. 9(b). The two coefficients have a consistent effect on curvature control. Consequently, this work employs κ_3 as a convexity control parameter.

4.2. Analytical calibration procedure for yield stress functions

The YSF of the new symmetric model comprises mutually independent functions: normal principal stress function $f_{\text{Principal}}(\boldsymbol{\sigma})$ and shear stress function $f_{\text{Shear}}(\boldsymbol{\sigma})$. $f_{\text{Principal}}(\boldsymbol{\sigma})$ is calibrated through experimental sampling points on the NP-YL, while $f_{\text{Shear}}(\boldsymbol{\sigma})$ will be identified by the yield stresses associated with the shear stress component. The detailed analysis calibration procedure is outlined below.

Bringing the stress components of UT0 and UT90 into Eq. (1), we have

$$\kappa_1 \text{UT0}^6(\bar{\varepsilon}^{\text{p}}) = \bar{\sigma}^6(\bar{\varepsilon}^{\text{p}}) = 1 \tag{10}$$

$$\kappa_7 \text{UT90}^6(\bar{\varepsilon}^{\text{p}}) = \bar{\sigma}^6(\bar{\varepsilon}^{\text{p}}) \tag{11}$$

Under e-BT stress state, combining Eq. (1) and Eq. (9), there is

$$\kappa_1+\kappa_2+\kappa_3+\kappa_4+\kappa_5+\kappa_6+\kappa_7 = \left[\frac{\bar{\sigma}(\bar{\varepsilon}^{\text{p}})}{\text{EBT}(\bar{\varepsilon}^{\text{p}})}\right]^6 \tag{12}$$

According to NPS0, NPS90, and Eq. (1), we have

$$\begin{aligned}&\kappa_1 + p_0(\bar{\varepsilon}^{\text{p}})\kappa_2 + p_0^2(\bar{\varepsilon}^{\text{p}})\kappa_3 + p_0^3(\bar{\varepsilon}^{\text{p}})\kappa_4\\ &+p_0^4(\bar{\varepsilon}^{\text{p}})\kappa_5 + p_0^5(\bar{\varepsilon}^{\text{p}})\kappa_6 + p_0^6(\bar{\varepsilon}^{\text{p}})\kappa_7 = \left[\frac{\bar{\sigma}(\bar{\varepsilon}^{\text{p}})}{\text{NPS0}(\bar{\varepsilon}^{\text{p}})}\right]^6\end{aligned} \tag{13}$$

$$\begin{aligned}&p_{90}^6(\bar{\varepsilon}^{\text{p}})\kappa_1 + p_{90}^5(\bar{\varepsilon}^{\text{p}})\kappa_2 + p_{90}^4(\bar{\varepsilon}^{\text{p}})\kappa_3 + p_{90}^3(\bar{\varepsilon}^{\text{p}})\kappa_4\\ &+p_{90}^2(\bar{\varepsilon}^{\text{p}})\kappa_5 + p_{90}(\bar{\varepsilon}^{\text{p}})\kappa_6 + \kappa_7 = \left[\frac{\bar{\sigma}(\bar{\varepsilon}^{\text{p}})}{\text{NPS90}(\bar{\varepsilon}^{\text{p}})}\right]^6\end{aligned} \tag{14}$$

Similarly, under SS45 loading condition, Eq. (1) is rewritten as

$$\kappa_1-\kappa_2+\kappa_3-\kappa_4+\kappa_5-\kappa_6+\kappa_7 = \left[\frac{\bar{\sigma}(\bar{\varepsilon}^{\text{p}})}{\text{SS45}(\bar{\varepsilon}^{\text{p}})}\right]^6 \tag{15}$$

Combining Eqs. (10) – (15), $\kappa_i(i=1,2,\ldots,7)$ are expressed as

$$\kappa_1 = \left[\frac{\bar{\sigma}(\bar{\varepsilon}^{\text{p}})}{\text{UT0}(\bar{\varepsilon}^{\text{p}})}\right]^6 = 1 \tag{16a}$$

$$\kappa_7 = \left[\frac{\overline{\sigma}(\overline{\varepsilon}^{\mathrm{p}})}{\mathrm{UT90}(\overline{\varepsilon}^{\mathrm{p}})}\right]^6 \tag{16b}$$

$$\begin{bmatrix}\kappa_2\\ \kappa_4\\ \kappa_5\\ \kappa_6\end{bmatrix} = \begin{bmatrix}1 & 1 & 1 & 1\\ -1 & -1 & 1 & -1\\ p_0(\overline{\varepsilon}^{\mathrm{p}}) & p_0^3(\overline{\varepsilon}^{\mathrm{p}}) & p_0^4(\overline{\varepsilon}^{\mathrm{p}}) & p_0^5(\overline{\varepsilon}^{\mathrm{p}})\\ p_{90}^5(\overline{\varepsilon}^{\mathrm{p}}) & p_{90}^4(\overline{\varepsilon}^{\mathrm{p}}) & p_{90}^3(\overline{\varepsilon}^{\mathrm{p}}) & p_{90}(\overline{\varepsilon}^{\mathrm{p}})\end{bmatrix}^{-1} \begin{bmatrix}\Gamma_{\mathrm{EBT}}\\ \Gamma_{\mathrm{SS45}}\\ \Gamma_{\mathrm{NPS0}}\\ \Gamma_{\mathrm{NPS90}}\end{bmatrix} \tag{16c}$$

with

$$\Gamma_{\mathrm{EBT}} = \left[\frac{\overline{\sigma}(\overline{\varepsilon}^{\mathrm{p}})}{\mathrm{EBT}(\overline{\varepsilon}^{\mathrm{p}})}\right]^6 - \kappa_1 - \kappa_3 - \kappa_7 \tag{16d}$$

$$\Gamma_{\mathrm{SS45}} = \left[\frac{\overline{\sigma}(\overline{\varepsilon}^{\mathrm{p}})}{\mathrm{SS45}(\overline{\varepsilon}^{\mathrm{p}})}\right]^6 - \kappa_1 - \kappa_3 - \kappa_7 \tag{16e}$$

$$\Gamma_{\mathrm{NPS0}} = \left[\frac{\overline{\sigma}(\overline{\varepsilon}^{\mathrm{p}})}{\mathrm{NPS0}(\overline{\varepsilon}^{\mathrm{p}})}\right]^6 - \kappa_1 - p_0^2(\overline{\varepsilon}^{\mathrm{p}})\kappa_3 - p_0^6(\overline{\varepsilon}^{\mathrm{p}})\kappa_7 \tag{16f}$$

$$\Gamma_{\mathrm{NPS90}} = \left[\frac{\overline{\sigma}(\overline{\varepsilon}^{\mathrm{p}})}{\mathrm{NPS90}(\overline{\varepsilon}^{\mathrm{p}})}\right]^6 - p_{90}^6(\overline{\varepsilon}^{\mathrm{p}})\kappa_1 - p_{90}^4(\overline{\varepsilon}^{\mathrm{p}})\kappa_3 - \kappa_7 \tag{16g}$$

The shear stress function of the YSF of the new symmetric model contains four anisotropic coefficients, which are further analytically calibrated using UT30, UT45, UT60, and NPS45. Under NPS loadings, Eq. (9) is simplified to

$$\begin{cases}\sigma_{11} = \sigma_{xx}\left(\cos^2\alpha + p_\alpha \sin^2\alpha\right)\\ \sigma_{22} = \sigma_{xx}\left(\sin^2\alpha + p_\alpha \cos^2\alpha\right)\\ \sigma_{12} = \sigma_{xx}(1 - p_\alpha)\sin\alpha\cos\alpha\end{cases} \tag{17}$$

By combining Eqs. (1) and (17), there is

$$\nu_8(\alpha,p)\kappa_8 + \nu_9(\alpha,p)\kappa_9 + \nu_{10}(\alpha,p)\kappa_{10} + \nu_{11}(\alpha,p)\kappa_{11} = \delta_y(\alpha,p) \tag{18a}$$

with

$$\begin{cases}\delta_y(\alpha,p) = \left[\frac{\overline{\sigma}(\overline{\varepsilon}^{\mathrm{p}})}{\mathrm{NPS}\alpha(\overline{\varepsilon}^{\mathrm{p}})}\right]^4 - \left[\kappa_1\nu_1 + \kappa_2\nu_2 + \kappa_3\nu_3 + \kappa_4\nu_4 + \kappa_5\nu_5 + \kappa_6\nu_6 + \kappa_7\nu_7\right]^{\frac{2}{3}}\\ \nu_1(\alpha,p) = \left[\cos^2\alpha + p_\alpha(\overline{\varepsilon}^{\mathrm{p}})\sin^2\alpha\right]^6\\ \nu_2(\alpha,p) = \left[\cos^2\alpha + p_\alpha(\overline{\varepsilon}^{\mathrm{p}})\sin^2\alpha\right]^5\left[\sin^2\alpha + p_\alpha(\overline{\varepsilon}^{\mathrm{p}})\cos^2\alpha\right]\\ \nu_3(\alpha,p) = \left[\cos^2\alpha + p_\alpha(\overline{\varepsilon}^{\mathrm{p}})\sin^2\alpha\right]^4\left[\sin^2\alpha + p_\alpha(\overline{\varepsilon}^{\mathrm{p}})\cos^2\alpha\right]^2\\ \nu_4(\alpha,p) = \left[\cos^2\alpha + p_\alpha(\overline{\varepsilon}^{\mathrm{p}})\sin^2\alpha\right]^3\left[\sin^2\alpha + p_\alpha(\overline{\varepsilon}^{\mathrm{p}})\cos^2\alpha\right]^3\\ \nu_5(\alpha,p) = \left[\cos^2\alpha + p_\alpha(\overline{\varepsilon}^{\mathrm{p}})\sin^2\alpha\right]^2\left[\sin^2\alpha + p_\alpha(\overline{\varepsilon}^{\mathrm{p}})\cos^2\alpha\right]^4\\ \nu_6(\alpha,p) = \left[\cos^2\alpha + p_\alpha(\overline{\varepsilon}^{\mathrm{p}})\sin^2\alpha\right]\left[\sin^2\alpha + p_\alpha(\overline{\varepsilon}^{\mathrm{p}})\cos^2\alpha\right]^5\\ \nu_7(\alpha,p) = \left[\sin^2\alpha + p_\alpha(\overline{\varepsilon}^{\mathrm{p}})\cos^2\alpha\right]^6\\ \nu_8(\alpha,p) = \left[\cos^2\alpha + p_\alpha(\overline{\varepsilon}^{\mathrm{p}})\sin^2\alpha\right]^2\left\{\left[1 - p_\alpha(\overline{\varepsilon}^{\mathrm{p}})\right]\sin\alpha\cos\alpha\right\}^2\\ \nu_9(\alpha,p) = \left[\cos^2\alpha + p_\alpha(\overline{\varepsilon}^{\mathrm{p}})\sin^2\alpha\right]\left[\sin^2\alpha + p_\alpha(\overline{\varepsilon}^{\mathrm{p}})\cos^2\alpha\right]\\ \quad\cdot\left\{\left[1 - p_\alpha(\overline{\varepsilon}^{\mathrm{p}})\right]\sin\alpha\cos\alpha\right\}^2\\ \nu_{10}(\alpha,p) = \left[\sin^2\alpha + p_\alpha(\overline{\varepsilon}^{\mathrm{p}})\cos^2\alpha\right]^2\left\{\left[1 - p_\alpha(\overline{\varepsilon}^{\mathrm{p}})\right]\sin\alpha\cos\alpha\right\}^2\\ \nu_{11}(\alpha,p) = \left\{\left[1 - p_\alpha(\overline{\varepsilon}^{\mathrm{p}})\right]\sin\alpha\cos\alpha\right\}^4\end{cases} \tag{18b}$$

When $p_\alpha(\overline{\varepsilon}^{\mathrm{p}}) = 0$ and NPSα are replaced with UTα, Eq. (18) will degenerate into a function related to the UTα stress component. Under UT and NPS stress states, according to Eq. (18), the analytical expression of $\kappa_i (i = 8, 9, 10, 11)$ is written as

$$\begin{bmatrix}\kappa_8\\ \kappa_9\\ \kappa_{10}\\ \kappa_{11}\end{bmatrix} = \begin{bmatrix}\nu_8(\alpha_1) & \nu_9(\alpha_1) & \nu_{10}(\alpha_1) & \nu_{11}(\alpha_1)\\ \nu_8(\alpha_2) & \nu_9(\alpha_2) & \nu_{10}(\alpha_2) & \nu_{11}(\alpha_2)\\ \nu_8(\alpha_3) & \nu_9(\alpha_3) & \nu_{10}(\alpha_3) & \nu_{11}(\alpha_3)\\ \nu_8(\alpha_4,p_{\alpha_4}) & \nu_9(\alpha_4,p_{\alpha_4}) & \nu_{10}(\alpha_4,p_{\alpha_4}) & \nu_{11}(\alpha_4,p_{\alpha_4})\end{bmatrix}^{-1} \begin{bmatrix}\delta_y(\alpha_1)\\ \delta_y(\alpha_2)\\ \delta_y(\alpha_3)\\ \delta_y(\alpha_4,p_{\alpha_4})\end{bmatrix} \tag{19}$$

where $\{\alpha_1, \alpha_2, \alpha_3, \alpha_4\} = \{30, 45, 60, 45\}$. Note that the value of the convexity control parameter is not unique when the yield criterion satisfies the convexity condition. This work uses the midpoint of the upper and lower bounds as the final result of κ_3. Meanwhile, the yield surface described by the YSF of the new symmetric model has been verified by the new convexity proof method. For the YSF of the new asymmetric model, under UT and e-BT stress states, $f_{\mathrm{TC}}(\boldsymbol{\sigma})$ is simplified as

$$f_{\mathrm{TC}}(\boldsymbol{\sigma}_{\mathrm{UT}\alpha}) = 1 \tag{20a}$$

$$f_{\mathrm{TC}}(\boldsymbol{\sigma}_{\mathrm{EBT}}) = 1 \tag{20b}$$

It indicates that the asymmetric term $f_{\mathrm{TC}}(\boldsymbol{\sigma})$ has no impact on the parameter calibration results of the YSF of the new asymmetric model under UT and e-BT loadings. However, $f_{\mathrm{TC}}(\boldsymbol{\sigma}_{\mathrm{NPS/SS}}) \neq 1$ under the NPS and SS stress states. Therefore, the contribution of $f_{\mathrm{TC}}(\boldsymbol{\sigma})$ needs to be considered in the parameter identification procedure. Detailed analytical calibration procedures for the YSF of the new asymmetric model can be found in Appendix A.

4.3. Analytical calibration procedure for plastic potential functions

The normal principal stress function $\Phi_{\mathrm{Principal}}(\boldsymbol{\sigma})$ of the PPF of the new symmetric model possesses seven anisotropic coefficients $\kappa_i (i = 1, 2, \ldots, 7)$. Bringing the stress components of UT0 into Eq. (1) leads to

$$\mathrm{UT0}^6(\overline{\varepsilon}^{\mathrm{p}})\kappa_1 = \overline{\sigma}^6(\overline{\varepsilon}^{\mathrm{p}}) \tag{21}$$

Based on the definition of the plastic strain ratio under uniaxial stress state, the intrinsic connection between the r-value and the loading direction can be expressed as

$$\left(r_\alpha + \sin^2\alpha\right)\frac{\partial P(\boldsymbol{\sigma})}{\sigma_{11}} + \left(r_\alpha + \cos^2\alpha\right)\frac{\partial P(\boldsymbol{\sigma})}{\sigma_{22}} - \sin\alpha\cos\alpha\frac{\partial P(\boldsymbol{\sigma})}{\sigma_{12}} = 0 \tag{22}$$

where the expressions of $\frac{\partial P(\boldsymbol{\sigma})}{\sigma_{ij}}(i,j = 1,2)$ can be found in Appendix B. Combining Eqs. (1) and (22), r_{T0} and r_{T90} are defined as

$$r_{\mathrm{T0}} = -\frac{\kappa_2}{6 + \kappa_2} \tag{23a}$$

$$r_{\mathrm{T90}} = -\frac{\kappa_6}{6\kappa_7 + \kappa_6} \tag{23b}$$

Under e-BT stress state, we have

$$r_{\mathrm{b}} = \frac{\frac{\partial P(\boldsymbol{\sigma})}{\partial \sigma_{22}}}{\frac{\partial P(\boldsymbol{\sigma})}{\partial \sigma_{11}}} \tag{24}$$

According to Eqs. (1) and (24), there is

$$\psi_3\left(r_{\mathrm{b}}, p_{r_{\mathrm{b}}}\right)\kappa_3 + \psi_4\left(r_{\mathrm{b}}, p_{r_{\mathrm{b}}}\right)\kappa_4 + \psi_5\left(r_{\mathrm{b}}, p_{r_{\mathrm{b}}}\right)\kappa_5 = \delta_r\left(r_{\mathrm{b}}, p_{r_{\mathrm{b}}}\right) \tag{25a}$$

with

$$\begin{cases} \delta_r\left(r_b, p_{r_b}\right) = -\left[\psi_1\left(r_b, p_{r_b}\right)\kappa_1 + \psi_2\left(r_b, p_{r_b}\right)\kappa_2 + \psi_6\left(r_b, p_{r_b}\right)\kappa_6 + \psi_7\left(r_b, p_{r_b}\right)\kappa_7\right] \\ \psi_1\left(r_b, p_{r_b}\right) = 6r_b(\bar{\varepsilon}^p) \\ \psi_2\left(r_b, p_{r_b}\right) = 5r_b(\bar{\varepsilon}^p)p_{r_b}(\bar{\varepsilon}^p) - 1 \\ \psi_3\left(r_b, p_{r_b}\right) = 4r_b(\bar{\varepsilon}^p)p_{r_b}^2(\bar{\varepsilon}^p) - 2p_{r_b}(\bar{\varepsilon}^p) \\ \psi_4\left(r_b, p_{r_b}\right) = 3r_b(\bar{\varepsilon}^p)p_{r_b}^3(\bar{\varepsilon}^p) - 3p_{r_b}^2(\bar{\varepsilon}^p) \\ \psi_5\left(r_b, p_{r_b}\right) = 2r_b(\bar{\varepsilon}^p)p_{r_b}^4(\bar{\varepsilon}^p) - 4p_{r_b}^3(\bar{\varepsilon}^p) \\ \psi_6\left(r_b, p_{r_b}\right) = r_b(\bar{\varepsilon}^p)p_{r_b}^5(\bar{\varepsilon}^p) - 5p_{r_b}^4(\bar{\varepsilon}^p) \\ \psi_7\left(r_b, p_{r_b}\right) = -6p_{r_b}^5(\bar{\varepsilon}^p) \end{cases} \tag{25b}$$

where p_{r_b} represents the practical stress ratio of a cruciform tensile sample under e-BT loading. ω_0 and ω_{90} are defined as

$$\omega_0 = \tan^{-1}\left[\frac{\frac{\partial P(\boldsymbol{\sigma})}{\partial \sigma_{22}}}{\frac{\partial P(\boldsymbol{\sigma})}{\partial \sigma_{11}}}\right] \tag{26a}$$

$$\omega_{90} = \tan^{-1}\left[\frac{\frac{\partial P(\boldsymbol{\sigma})}{\partial \sigma_{11}}}{\frac{\partial P(\boldsymbol{\sigma})}{\partial \sigma_{22}}}\right] \tag{26b}$$

Combining Eqs. (1), (17), and (26), we have

$$\psi_3(\omega_0, p_0)\kappa_3 + \psi_4(\omega_0, p_0)\kappa_4 + \psi_5(\omega_0, p_0)\kappa_5 = \delta_r(\omega_0, p_0) \tag{27a}$$

$$\psi_3(\omega_{90}, p_{90})\kappa_3 + \psi_4(\omega_{90}, p_{90})\kappa_4 + \psi_5(\omega_{90}, p_{90})\kappa_5 = \delta_r(\omega_{90}, p_{90}) \tag{27b}$$

with

$$\begin{aligned} \delta_r(\omega_0, p_0) = & -[\psi_1(\omega_0, p_0)\kappa_1 + \psi_2(\omega_0, p_0)\kappa_2 + \psi_6(\omega_0, p_0)\kappa_6 \\ & + \psi_7(\omega_0, p_0)\kappa_7] \end{aligned} \tag{27c}$$

$$\begin{aligned} \delta_r(\omega_{90}, p_{90}) = & -\psi_1(\omega_{90}, p_{90})\kappa_1 - \psi_2(\omega_{90}, p_{90})\kappa_2 - \psi_6(\omega_{90}, p_{90})\kappa_6 \\ & - \psi_7(\omega_{90}, p_{90})\kappa_7 \end{aligned} \tag{27d}$$

$$\begin{cases} \psi_1(\omega_0, p_0) = 6\tan[\omega_0(\bar{\varepsilon}^p)] \\ \psi_2(\omega_0, p_0) = 5p_0(\bar{\varepsilon}^p)\tan[\omega_0(\bar{\varepsilon}^p)] - 1 \\ \psi_3(\omega_0, p_0) = 4p_0^2(\bar{\varepsilon}^p)\tan[\omega_0(\bar{\varepsilon}^p)] - 2p_0(\bar{\varepsilon}^p) \\ \psi_4(\omega_0, p_0) = 3p_0^3(\bar{\varepsilon}^p)\tan[\omega_0(\bar{\varepsilon}^p)] - 3p_0^2(\bar{\varepsilon}^p) \\ \psi_5(\omega_0, p_0) = 2p_0^4(\bar{\varepsilon}^p)\tan[\omega_0(\bar{\varepsilon}^p)] - 4p_0^3(\bar{\varepsilon}^p) \\ \psi_6(\omega_0, p_0) = p_0^5(\bar{\varepsilon}^p)\tan[\omega_0(\bar{\varepsilon}^p)] - 5p_0^4(\bar{\varepsilon}^p) \\ \psi_7(\omega_0, p_0) = -6p_0^5(\bar{\varepsilon}^p) \end{cases} \tag{27e}$$

$$\begin{cases} \psi_1(\omega_{90}, p_{90}) = -6p_{90}^5(\bar{\varepsilon}^p) \\ \psi_2(\omega_{90}, p_{90}) = p_{90}^5(\bar{\varepsilon}^p)\tan[\omega_{90}(\bar{\varepsilon}^p)] - 5p_{90}^4(\bar{\varepsilon}^p) \\ \psi_3(\omega_{90}, p_{90}) = 2p_{90}^4(\bar{\varepsilon}^p)\tan[\omega_{90}(\bar{\varepsilon}^p)] - 4p_{90}^3(\bar{\varepsilon}^p) \\ \psi_4(\omega_{90}, p_{90}) = 3p_{90}^3(\bar{\varepsilon}^p)\tan[\omega_{90}(\bar{\varepsilon}^p)] - 3p_{90}^2(\bar{\varepsilon}^p) \\ \psi_5(\omega_{90}, p_{90}) = 4p_{90}^2(\bar{\varepsilon}^p)\tan[\omega_{90}(\bar{\varepsilon}^p)] - 2p_{90}(\bar{\varepsilon}^p) \\ \psi_6(\omega_{90}, p_{90}) = 5p_{90}(\bar{\varepsilon}^p)\tan[\omega_{90}(\bar{\varepsilon}^p)] - 1 \\ \psi_7(\omega_{90}, p_{90}) = 6\tan[\omega_{90}(\bar{\varepsilon}^p)] \end{cases} \tag{27f}$$

Through Eqs. (21), (23), (25), and (27), the analytical solutions of $\kappa_i (i = 1, 2, \cdots, 6)$ are written as

$$\kappa_1 = \left[\frac{\bar{\sigma}(\bar{\varepsilon}^p)}{\mathrm{UT0}(\bar{\varepsilon}^p)}\right]^6 = 1 \tag{28a}$$

$$\kappa_2 = -\frac{6r_{T0}(\bar{\varepsilon}^p)}{1 + r_{T0}(\bar{\varepsilon}^p)} \tag{28b}$$

$$\kappa_6 = -\frac{6r_{T90}(\bar{\varepsilon}^p)\chi_7}{1 + r_{T90}(\bar{\varepsilon}^p)} \tag{28c}$$

$$\begin{bmatrix} \kappa_3 \\ \kappa_4 \\ \kappa_5 \end{bmatrix} = \begin{bmatrix} \psi_3\left(r_b, p_{r_b}\right) & \psi_4\left(r_b, p_{r_b}\right) & \psi_5\left(r_b, p_{r_b}\right) \\ \psi_3(\omega_0, p_0) & \psi_4(\omega_0, p_0) & \psi_5(\omega_0, p_0) \\ \psi_3(\omega_{90}, p_{90}) & \psi_4(\omega_{90}, p_{90}) & \psi_5(\omega_{90}, p_{90}) \end{bmatrix} \begin{bmatrix} \delta_r\left(r_b, p_{r_b}\right) \\ \delta_r(\omega_0, p_0) \\ \delta_r(\omega_{90}, p_{90}) \end{bmatrix} \tag{28d}$$

Eq. (30) is utilized to define the relationship between ω_{45} and the stress components.

$$\omega_{45} = \tan^{-1}\left(\frac{\frac{\partial P(\boldsymbol{\sigma})}{\partial \sigma_{yy}}}{\frac{\partial P(\boldsymbol{\sigma})}{\partial \sigma_{xx}}}\right) \tag{29}$$

Experimental ω_{45} is employed for calibration of the anisotropic coefficients of the shear stress function $\Phi_{\mathrm{Shear}}(\boldsymbol{\sigma})$. Based on Eqs. (1), (17), and (29), there is

$$\begin{aligned} & \psi_8(\omega_{45}, p_{45})\kappa_8 + \psi_9(\omega_{45}, p_{45})\kappa_9 + \psi_{10}(\omega_{45}, p_{45})\kappa_{10} + \psi_{11}(\omega_{45}, p_{45})\kappa_{11} \\ & = \delta_r(\omega_{45}, p_{45}) \end{aligned} \tag{30a}$$

with

$$\delta_r(\omega_{45}, p_{45}) = -\frac{2\{\tan[\omega_{45}(\bar{\varepsilon}^p)] - 1\}}{3\Phi_{\mathrm{Principal}}^{1/3}(\boldsymbol{\sigma}_{\omega 45})}\left[\frac{\partial \Phi_{\mathrm{Principal}}(\boldsymbol{\sigma}_{\omega 45})}{\partial \sigma_{11}} + \frac{\partial \Phi_{\mathrm{Principal}}(\boldsymbol{\sigma}_{\omega 45})}{\partial \sigma_{22}}\right] \tag{30b}$$

$$\begin{cases} \psi_8(\omega_{45}, p_{45}) = 2[1 + p_{45}(\bar{\varepsilon}^p)][1 - p_{45}(\bar{\varepsilon}^p)]^2 \\ \bullet\{\tan[\omega_{45}(\bar{\varepsilon}^p)] - 1\} + 2[1 + p_{45}(\bar{\varepsilon}^p)]^2[1 - p_{45}(\bar{\varepsilon}^p)]\{\tan[\omega_{45}(\bar{\varepsilon}^p)] + 1\} \\ \psi_9(\omega_{45}, p_{45}) = 2[1 + p_{45}(\bar{\varepsilon}^p)][1 - p_{45}(\bar{\varepsilon}^p)]^2 \\ \bullet\{\tan[\omega_{45}(\bar{\varepsilon}^p)] - 1\} + 2[1 + p_{45}(\bar{\varepsilon}^p)]^2[1 - p_{45}(\bar{\varepsilon}^p)]\{\tan[\omega_{45}(\bar{\varepsilon}^p)] + 1\} \\ \psi_{10}(\omega_{45}, p_{45}) = 2[1 + p_{45}(\bar{\varepsilon}^p)][1 - p_{45}(\bar{\varepsilon}^p)]^2 \\ \bullet\{\tan[\omega_{45}(\bar{\varepsilon}^p)] - 1\} + 2[1 + p_{45}(\bar{\varepsilon}^p)]^2[1 - p_{45}(\bar{\varepsilon}^p)]\{\tan[\omega_{45}(\bar{\varepsilon}^p)] + 1\} \\ \psi_{11}(\omega_{45}, p_{45}) = 4[1 - p_{45}(\bar{\varepsilon}^p)]^3\{\tan[\omega_{45}(\bar{\varepsilon}^p)] - 1\} \end{cases} \tag{30c}$$

Table 3
Yield stresses of DP490 and AA6016-T4 at the initial yielding point (EPS = 0.002, unit in MPa).

DP490	UT0	UT15	UT30	UT45	UT60	UT75	UT90	EBT	SS0	SS45
	393.83	389.55	383.20	374.98	383.40	389.16	386.14	408.26	228.03	222.84
	NPS0{x}	NPS45{x}	NPS90{x}	$BT_{4:1}^{NP}\{x\}$	$BT_{4:3}^{NP}\{x\}$	$BT_{3:4}^{NP}\{x\}$	$BT_{1:4}^{NP}\{x\}$	$BT_{4:1}^{DP}\{x\}$	$BT_{4:3}^{DP}\{x\}$	
	435.39	448.28	451.82	420.57	430.43	450.82	439.29	426.95	440.68	
	NPS0{y}	NPS45{y}	NPS90{y}	$BT_{4:1}^{NP}\{y\}$	$BT_{4:3}^{NP}\{y\}$	$BT_{3:4}^{NP}\{y\}$	$BT_{1:4}^{NP}\{y\}$	$BT_{4:1}^{DP}\{y\}$	$BT_{4:3}^{DP}\{y\}$	
	218.21	224.89	226.61	105.45	322.56	339.11	111.55	107.23	330.20	
AA6016-T4	UT0	UT15	UT30	UT45	UT60	UT75	UT90	EBT	SS0	SS45
	132.19	128.72	126.20	123.83	122.61	121.70	122.25	125.39	83.06	73.48
	NPS0{x}	NPS45{x}	NPS90{x}	$BT_{4:1}^{NP}\{x\}$	$BT_{4:3}^{NP}\{x\}$	$BT_{3:4}^{NP}\{x\}$	$BT_{1:4}^{NP}\{x\}$	$BT_{4:1}^{DP}\{x\}$	$BT_{4:3}^{DP}\{x\}$	
	141.47	132.44	135.84	138.20	138.83	131.70	130.47	129.76	135.58	
	NPS0{y}	NPS45{y}	NPS90{y}	$BT_{4:1}^{NP}\{y\}$	$BT_{4:3}^{NP}\{y\}$	$BT_{3:4}^{NP}\{y\}$	$BT_{1:4}^{NP}\{y\}$	$BT_{4:1}^{DP}\{y\}$	$BT_{4:3}^{DP}\{y\}$	
	71.11	66.86	68.08	34.86	104.86	99.20	32.84	32.94	102.09	

with

$$\begin{cases} \Phi_{\text{Principal}}(\boldsymbol{\sigma}_{\omega 45}) = [1+p_{45}(\bar{\varepsilon}^{\text{p}})]^6(\kappa_1+\kappa_2+\kappa_3+\kappa_4+\kappa_5+\kappa_6+\kappa_7) \\ \dfrac{\partial \Phi_{\text{Principal}}(\boldsymbol{\sigma}_{\omega 45})}{\partial \sigma_{11}} = [1+p_{45}(\bar{\varepsilon}^{\text{p}})]^5(6\kappa_1+5\kappa_2+4\kappa_3+3\kappa_4+2\kappa_5+\kappa_6) \\ \dfrac{\partial \Phi_{\text{Principal}}(\boldsymbol{\sigma}_{\omega 45})}{\partial \sigma_{22}} = [1+p_{45}(\bar{\varepsilon}^{\text{p}})]^5(\kappa_2+2\kappa_3+3\kappa_4+4\kappa_5+5\kappa_6+6\kappa_7) \end{cases} \tag{30d}$$

The stress components of r_{T30}, r_{T45}, and r_{T60} are brought into Eqs. (1) and (22), we obtain

$$\psi_8(r_{\text{T}\alpha},\alpha)\kappa_8+\psi_9(r_{\text{T}\alpha},\alpha)\kappa_9+\psi_{10}(r_{\text{T}\alpha},\alpha)\kappa_{10}+\psi_{11}(r_{\text{T}\alpha},\alpha)\kappa_{11}=\delta_r(r_{\text{T}\alpha},\alpha) \tag{31a}$$

with

$$\delta_r(r_{\text{T}\alpha},\alpha) = -\frac{2}{3\Phi_{\text{Principal}}^{1/3}(\boldsymbol{\sigma}_{r_{\text{T}\alpha}})}\left\{\left[r_{\text{T}\alpha}(\bar{\varepsilon}^{\text{p}})+\sin^2\alpha\right]\frac{\partial \Phi_{\text{Principal}}(\boldsymbol{\sigma}_{r_{\text{T}\alpha}})}{\partial \sigma_{11}}+\left[r_{\text{T}\alpha}(\bar{\varepsilon}^{\text{p}})+\cos^2\alpha\right]\frac{\partial \Phi_{\text{Principal}}(\boldsymbol{\sigma}_{r_{\text{T}\alpha}})}{\partial \sigma_{22}}\right\} \tag{31b}$$

$$\begin{cases} \Phi_{\text{Principal}}(\boldsymbol{\sigma}_{r_{\text{T}\alpha}}) = \kappa_1\cos^{12}\alpha+\kappa_2\cos^{10}\alpha\sin^2\alpha+\kappa_3\cos^8\alpha\sin^4\alpha+\kappa_4\cos^6\alpha\sin^6\alpha \\ \qquad +\kappa_5\cos^4\alpha\sin^8\alpha+\kappa_6\cos^2\alpha\sin^{10}\alpha+\kappa_7\sin^{12}\alpha \\ \dfrac{\partial \Phi_{\text{Principal}}(\boldsymbol{\sigma}_{r_{\text{T}\alpha}})}{\partial \sigma_{11}} = 6\kappa_1\cos^{10}\alpha+5\kappa_2\cos^8\alpha\sin^2\alpha+4\kappa_3\cos^6\alpha\sin^4\alpha \\ \qquad +3\kappa_4\cos^4\alpha\sin^6\alpha+2\kappa_5\cos^2\alpha\sin^8\alpha+\kappa_6\sin^{10}\alpha \\ \dfrac{\partial \Phi_{\text{Principal}}(\boldsymbol{\sigma}_{r_{\text{T}\alpha}})}{\partial \sigma_{22}} = \kappa_2\cos^{10}\alpha+2\kappa_3\cos^8\alpha\sin^2\alpha+3\kappa_4\cos^6\alpha\sin^4\alpha \\ \qquad +4\kappa_5\cos^4\alpha\sin^6\alpha+5\kappa_6\cos^2\alpha\sin^8\alpha+6\kappa_7\sin^{10}\alpha \end{cases} \tag{31c}$$

$$\begin{cases} \psi_8(r_{\text{T}\alpha},\alpha) = 2\cos^4\alpha\sin^2\alpha\left[r_{\text{T}\alpha}(\bar{\varepsilon}^{\text{p}})+\sin^2\alpha\right]-2\cos^6\alpha\sin^2\alpha \\ \psi_9(r_{\text{T}\alpha},\alpha) = \cos^2\alpha\sin^4\alpha\left[r_{\text{T}\alpha}(\bar{\varepsilon}^{\text{p}})+\sin^2\alpha\right] \\ \quad +\cos^4\alpha\sin^2\alpha\left[r_{\text{T}\alpha}(\bar{\varepsilon}^{\text{p}})+\cos^2\alpha\right]-2\cos^4\alpha\sin^4\alpha \\ \psi_{10}(r_{\text{T}\alpha},\alpha) = 2\cos^2\alpha\sin^4\alpha\left[r_{\text{T}\alpha}(\bar{\varepsilon}^{\text{p}})+\cos^2\alpha\right]-2\cos^2\alpha\sin^6\alpha \\ \psi_{11}(r_{\text{T}\alpha},\alpha) = -4\cos^4\alpha\sin^4\alpha \end{cases} \tag{31d}$$

The anisotropic coefficients in $\Phi_{\text{Shear}}(\boldsymbol{\sigma})$ can be calculated using Eqs. (30) and (31), are displayed as

where $\{\alpha_1,\alpha_2,\alpha_3,\alpha_4\}=\{30,45,60,45\}$. By now, the analytical expressions of the anisotropic coefficients in the PPF of the new symmetric model have been fully derived.

Using a similar approach as described in **Section 4.1**, κ_7 is chosen as the convexity control parameter, and its analytical identification process is similar to κ_3 in the YSF of the new symmetric model. Therefore, the solution process is not reiterated here. Additionally, the convexity of the PPF of the new symmetric model has been confirmed through the proposed convexity identification method. For further details on the analytical identification procedure of the PPF of the new asymmetric model, please refer to Appendix C.

5. Results and discussion of the new symmetric model

To investigate the predictive capability of the new symmetric model in characterizing the deformation response of sheet metals, the new symmetric model and several advanced yield criteria under AFR or NAFR, namely NAFR-Poly4 [43], EYld2000-2d [57], and AFR-Poly6 [58], are employed to characterize the anisotropic yield and plastic flow behaviors of DP490 and AA6016-T4 under various stress states.

A brief description of the experimental procedures is provided. The specimens for the UT test were prepared according to the ISO 6892–1:2019 standard and tested at room temperature with a tensile rate of 0.12 mm/s. The simple shear tests were conducted on a Zwick/Roell Z150 experimental machine at a tensile rate of 0.9 mm/min, in accordance with ASTM B831-19 standards. Uniaxial compression tests were performed using a MTS E45.105 universal electronic test machine with a compression rate of 2 mm/min. Biaxial tensile tests were prepared following the ISO 16842:2014 standard, utilizing cruciform specimens and conducted on a biaxial tensile system at a tensile rate of 0.1 mm/s. In addition, two repeated experiments were conducted for each load to ensure the accuracy of the experiments. Tables 3 and 4 present the mechanical properties of DP490 and AA6016-T4, respectively, as measured at the initial yielding, as reported by Du et al. [58,89]. Note that the stress ratios (k) of the biaxial tensile yield stresses (BT_k^{NP}) and DPSR (ω_k^{NP}) in the normal plane are 4:1, 4:3, 3:4, and 1:4. While k of the biaxial tension yield stress (BT_k^{DP}) and DPSR (ω_k^{DP}) in the diagonal plane are 4:1 and 4:3. Although these mechanical properties were not directly used in the analytical calibration of anisotropic coefficients, they are crucial for verifying the effectiveness of the YSF and PPF. The calibration results of all the yield criteria mentioned above can be found in Tables D1-D4 in Appendix D.

$$\begin{bmatrix}\kappa_8\\ \kappa_9\\ \kappa_{10}\\ \kappa_{11}\end{bmatrix} = \begin{bmatrix}\psi_8(r_{\text{T}\alpha_1},\alpha_1) & \psi_9(r_{\text{T}\alpha_1},\alpha_1) & \psi_{10}(r_{\text{T}\alpha_1},\alpha_1) & \psi_{11}(r_{\text{T}\alpha_1},\alpha_1)\\ \psi_8(r_{\text{T}\alpha_2},\alpha_2) & \psi_9(r_{\text{T}\alpha_2},\alpha_2) & \psi_{10}(r_{\text{T}\alpha_2},\alpha_2) & \psi_{11}(r_{\text{T}\alpha_2},\alpha_2)\\ \psi_8(r_{\text{T}\alpha_3},\alpha_3) & \psi_9(r_{\text{T}\alpha_3},\alpha_3) & \psi_{10}(r_{\text{T}\alpha_3},\alpha_3) & \psi_{11}(r_{\text{T}\alpha_3},\alpha_3)\\ \psi_8(\omega_{\alpha_4},p_{\alpha_4}) & \psi_9(\omega_{\alpha_4},p_{\alpha_4}) & \psi_{10}(\omega_{\alpha_4},p_{\alpha_4}) & \psi_{11}(\omega_{\alpha_4},p_{\alpha_4})\end{bmatrix}\begin{bmatrix}\delta_r(r_{\text{T}\alpha_1},\alpha_1)\\ \delta_r(r_{\text{T}\alpha_2},\alpha_2)\\ \delta_r(r_{\text{T}\alpha_3},\alpha_3)\\ \delta_r(\omega_{\alpha_4},p_{\alpha_4})\end{bmatrix} \tag{32}$$

Table 4
Plastic flow directions of DP490 and AA6016-T4 at the initial yielding point (EPS = 0.002).

DP490	r_{T0}	r_{T15}	r_{T30}	r_{T45}	r_{T60}	r_{T75}	r_{T90}	r_b	ρ_{r_b}
	0.4198	0.6672	0.7410	0.6393	0.9716	0.7620	0.7673	0.8662	0.9993
	ω_0	ω_{45}	ω_{90}	$\omega_{4:1}^{NP}$	$\omega_{4:3}^{NP}$	$\omega_{3:4}^{NP}$	$\omega_{1:4}^{NP}$	$\omega_{4:1}^{DP}$	$\omega_{4:3}^{DP}$
	9.1157	6.0548	9.6631	−10.6497	20.1952	20.4735	−17.0574	−16.1878	18.3661
AA6016-T4	r_{T0}	r_{T15}	r_{T30}	r_{T45}	r_{T60}	r_{T75}	r_{T90}	r_b	ρ_{r_b}
	0.5382	0.4342	0.2143	0.1496	0.2503	0.3259	0.4364	1.5063	0.9999
	ω_0	ω_{45}	ω_{90}	$\omega_{4:1}^{NP}$	$\omega_{4:3}^{NP}$	$\omega_{3:4}^{NP}$	$\omega_{1:4}^{NP}$	$\omega_{4:1}^{DP}$	$\omega_{4:3}^{DP}$
	7.5444	3.9425	5.5889	−14.3679	14.7126	15.9529	−14.3781	−6.4203	11.5428

Table 5
The UCα (unit in MPa) and $r_{C\alpha}$ of DP490 and AA6016-T4 at initial yielding point of EPS = 0.002.

	UC0	UC45	UC90	EBC[b]	r_{C0}	r_{C30}^{a}	r_{C45}	r_{C60}^{a}	r_{C90}
DP490	400.74	416.22	425.92	414.78	0.7549	0.6673	0.6403	0.6750	0.7724
AA6016-T4	133.80	144.96	125.00	137.18	0.3368	0.1932	0.1436	0.1742	0.2736

[a] r_{C30} and r_{C60} were calculated by the LAA2023 yield criterion [4].
[b] EBC = (UC0 + 2UC45 + UC90)/4.

Fig. 10 presents the NP-YLs and DP-YLs of DP490 and AA6016-T4 at the initial yielding point of EPS = 0.002, as predicted by the YSFs of the NAFR-Poly4, EYld2000-2d, AFR-Poly6, and new symmetric model, juxtaposed with the experimental data. For DP490 and AA6016-T4, the UT and biaxial tensile loads of the AFR-Poly6, NAFR-Poly4, and new symmetric model, i.e., the first quadrant of NP-YLs, exhibit similar predictive capabilities, accurately aligning with key calibration data points such as UT0, UT90, EBT, NPS0, and NPS90. However, EYld2000-2d, while accurately capturing UT0, UT90, and EBT, displays significant deviations for complex loadings between UT and e-BT stress states, as depicted in Fig. 10(a) and 10(c). This is attributed to the absence of experimental NPS mechanical properties in its parameter calibration procedure of EYld2000-2d. Meanwhile, the omission of SS yield stresses in the calibration of NAFR-Poly4 and AFR-Poly6 results in unsatisfactory prediction accuracy for the second quadrant of NP-YLs, notably SS45 for DP490 and AA6016-T4, where relative errors exceed 10 % and 15 % in NAFR-Poly4. Moreover, deviations in DP-YLs for all four YSFs are primarily concentrated in SS0, as shown in Fig. 10(b) and 10(d), owing to the exclusion of SS0 in the parameter identification process of any models. However, EYld2000-2d demonstrates insufficient accuracy in predicting the biaxial tensile loading region of DP490 compared to AFR-Poly6, NAFR-Poly4, and the new symmetric model, possibly due to the neglect of NPS45 in constraining the curvature of DP-YLs. It is noteworthy that the new symmetric model and NAFR-Poly4 exhibit highly similar DP-YL shapes, as they share the same shear stress function.

Fig. 11 shows the DPSRs in the normal and diagonal planes of DP490 and AA6016-T4 at the initial yielding point of EPS = 0.002, as predicted by the PPFs of the NAFR-Poly4, EYld2000-2d, AFR-Poly6, and new symmetric model, juxtaposed with the experimental data. Notably, EYld2000-2d and AFR-Poly6 exhibit significant deviations from experimental sampling points for the DPSRs in the normal and diagonal planes across the UT and e-BT stress states, whereas NAFR-Poly4 and the new symmetric model demonstrate more reasonable prediction accuracy. This discrepancy can be attributed to the utilization of $\omega_i (i = 0, 45, 90)$ during the parameter calibration procedures, improving the overall description accuracy of DPSRs around NPS regions in NAFR-Poly4 and the new symmetric model. Despite the consideration of r_b in the parameter identification strategy of NAFR-Poly4, there is still an underestimation of DPSRs, as shown in Fig. 11(a) and 11(c). This discrepancy arises from the tendency of optimization techniques to allocate global errors preferentially, resulting in varying degrees of calibration deviations across selected mechanical properties. Therefore, the new symmetric model with its analytical identification can accurately capture plastic flow behavior under complex loadings, showcasing its advanced predictive capability.

Fig. 12 presents the UT yield stresses of DP490 and AA6016-T4 at the initial yielding point of EPS = 0.002, as predicted by the YSFs of the NAFR-Poly4, EYld2000-2d, AFR-Poly6, and new symmetric model, and compares them with the experimental data. EYld2000-2d demonstrates the lowest accuracy among the YSFs, particularly for UT30 of DP490, where the relative error exceeds 10 % (see Fig. 12(a)). This inaccuracy can be attributed to EYld2000-2d using only three UT yield stresses to calibrate the anisotropic coefficients. In addition, the new symmetric model and NAFR-Poly4 offer more accurate predictions for UT75 compared to AFR-Poly6, despite employing the same number of UT$\alpha (\alpha = 0, 30, 45, 60, 90)$ for YSF calibration. This improvement is likely because a more concise form of the NAFR model allows for independent descriptions of anisotropic yield and plastic flow, significantly reducing over-constraints in YSFs. In summary, incorporating more UT yield stresses into the parameter identification procedure can markedly enhance the ability to describe the in-plane anisotropic yield behavior.

Fig. 13 shows the $r_{T\alpha}$−values of DP490 and AA6016-T4 at the initial yielding point of EPS = 0.002, as predicted by the PPFs of the NAFR-Poly4, EYld2000-2d, AFR-Poly6, and new symmetric model, compared with the experimental data. The $r_{T\alpha}$−value curves of DP490 and AA6016-T4 predicted by AFR-Poly6 align closely with the experimental data due to seven anisotropic coefficients are employed in AFR-Poly6 to describe the plastic flow behavior under UT loadings. Conversely, the NAFR-Poly4 and new symmetric model provide more accurate predictions compared to EYld2000-2d, primarily because they incorporate more $r_{T\alpha}$−values in the calibration process, such as r_{T30} and r_{T60}. Furthermore, while both NAFR-Poly4 and new symmetric model utilize experimental r_{T0} and r_{T90} values for calibrating the anisotropic coefficients of DP490, only the new symmetric model accurately characterizes these values, as shown in Fig. 13(a). Therefore, for PPFs with numerous anisotropic coefficients, an analytical method is recommended to accurately capture the in-plane anisotropic plastic flow behavior of sheet metals, thereby avoiding such issues.

To further systematically evaluate the prediction accuracy of the YSFs of the NAFR-Poly4, EYld2000-2d, AFR-Poly6, and new symmetric model on the stress-related plastic behavior of DP490 and AA6016-T4, Eq. (33) is used to quantitatively calculate the prediction errors of NP-YL (Δ_{YSF}^{NP}), DP-YL (Δ_{YSF}^{DP}), UT (Δ_{YSF}^{UT}), e-BT ($\Delta_{YSF}^{e\text{-}BT}$), NPS ($\Delta_{YSF}^{NPS}$), and SS ($\Delta_{YSF}^{SS}$).

$$\Delta_{YSF}^{\Omega} = \sqrt{\frac{1}{k}\sum_{i=1}^{k}\left\{\frac{F[\sigma_{11}^{exp.}(i), \sigma_{22}^{exp.}(i), \sigma_{12}^{exp.}(i)]}{UT0} - 1\right\}^2} (\Omega = NP,\ DP,\ UT,\ e\text{-}BT,\ NPS,\ SS) \quad (33a)$$

$$\Delta_{YSF}^{ALL} = \Delta_{YSF}^{NP} + \Delta_{YSF}^{DP} \quad (33b)$$

where the superscript "exp." represents the measurement data. Δ_{YSF}^{ALL} is the total error of Δ_{YSF}^{NP} and Δ_{YSF}^{DP}; i represents the i-th load; k represents the number of loads required for the error calculation. Note that the k values corresponding to $\Delta_{YSF}^{\Omega}(\Omega = NP, DP, UT, e\text{-}BT, NPS, SS)$ are 10, 6, 7, 1, 3, and 2, respectively.

Fig. 14 shows the prediction errors associated with the yield stresses of DP490 and AA6016-T4 calculated by the YSFs of the NAFR-Poly4, EYld2000-2d, AFR-Poly6, and new symmetric model. The new symmetric model provides the lowest level of Δ_{YSF}^{ALL} for two materials, with 2.96 % and 3.72 %, respectively. Compared to the other three YSFs, the new model improves the overall prediction accuracy by 54.53 %, 40.20 %, and 56.21 % for DP490, and 45.05 %, 53.67 %, and 49.39 % for AA6016-T4, respectively, as shown in Fig. 14**(a1)** and **14(b1)**. This can be attributed to the excellent description ability of the new symmetric model for both Δ_{YSF}^{NP} and Δ_{YSF}^{DP} of metallic sheets. Although the Δ_{YSF}^{NP} of AA6016-T4 calculated by EYld2000-2d decreased by 66.06 % compared to NAFR-Poly4, the Δ_{YSF}^{ALL} increased by 8.57 %, as shown in Fig. 14**(b1)**.

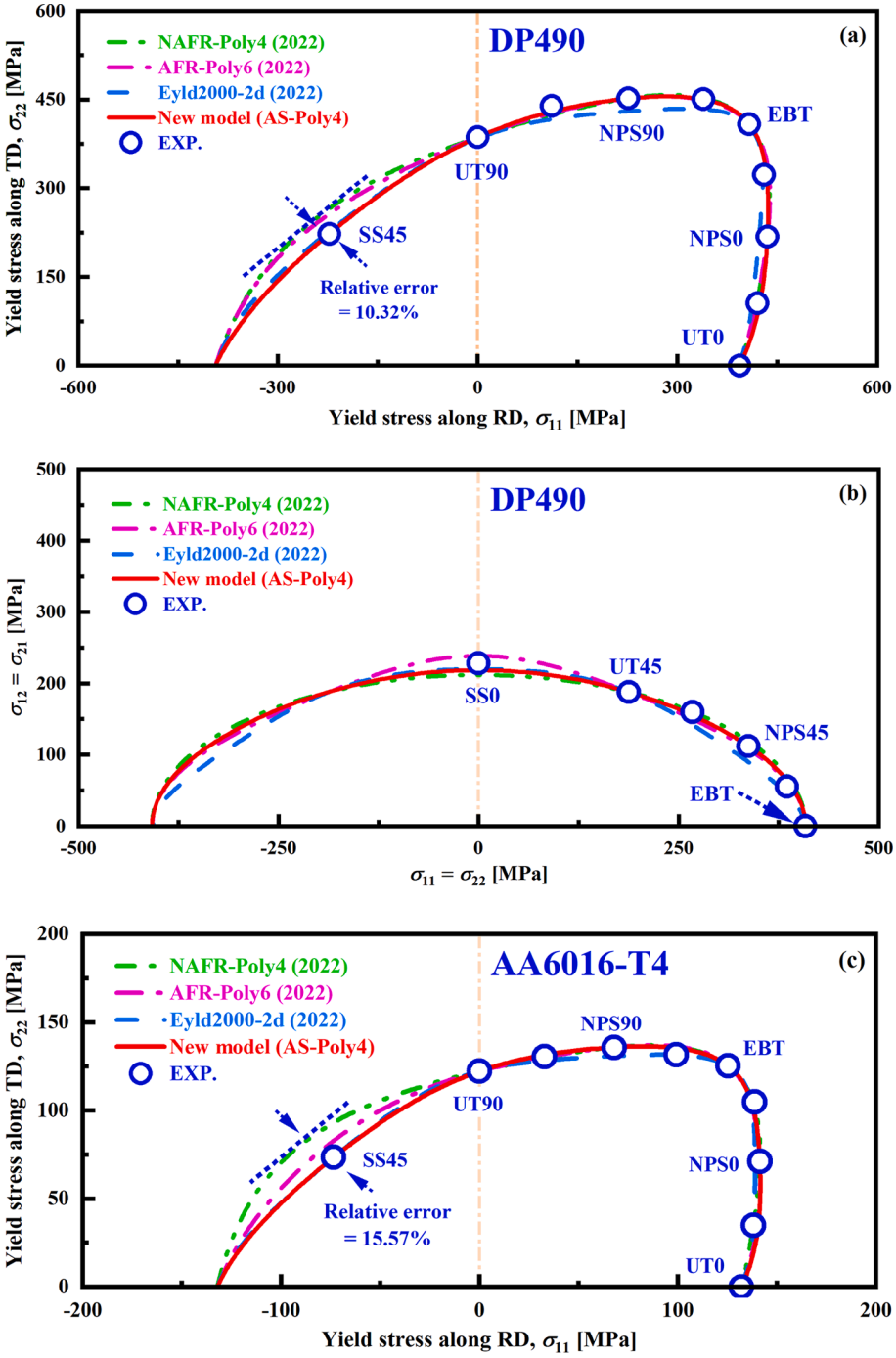

Fig. 10. NP-YLs and DP-YLs of (a-b) DP490 and (c-d) AA6016-T4 at the initial yielding point, predicted by the YSFs of the NAFR-Poly4, EYld2000-2d, AFR-Poly6, and new symmetric model.

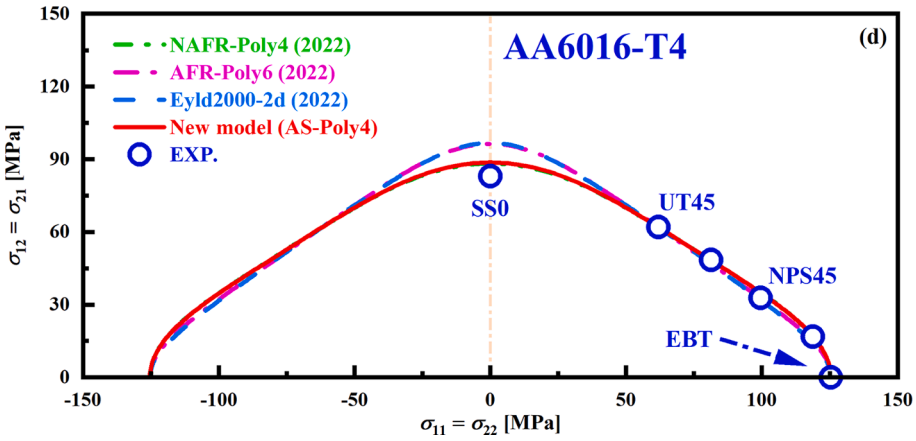

Fig. 10. (*continued*).

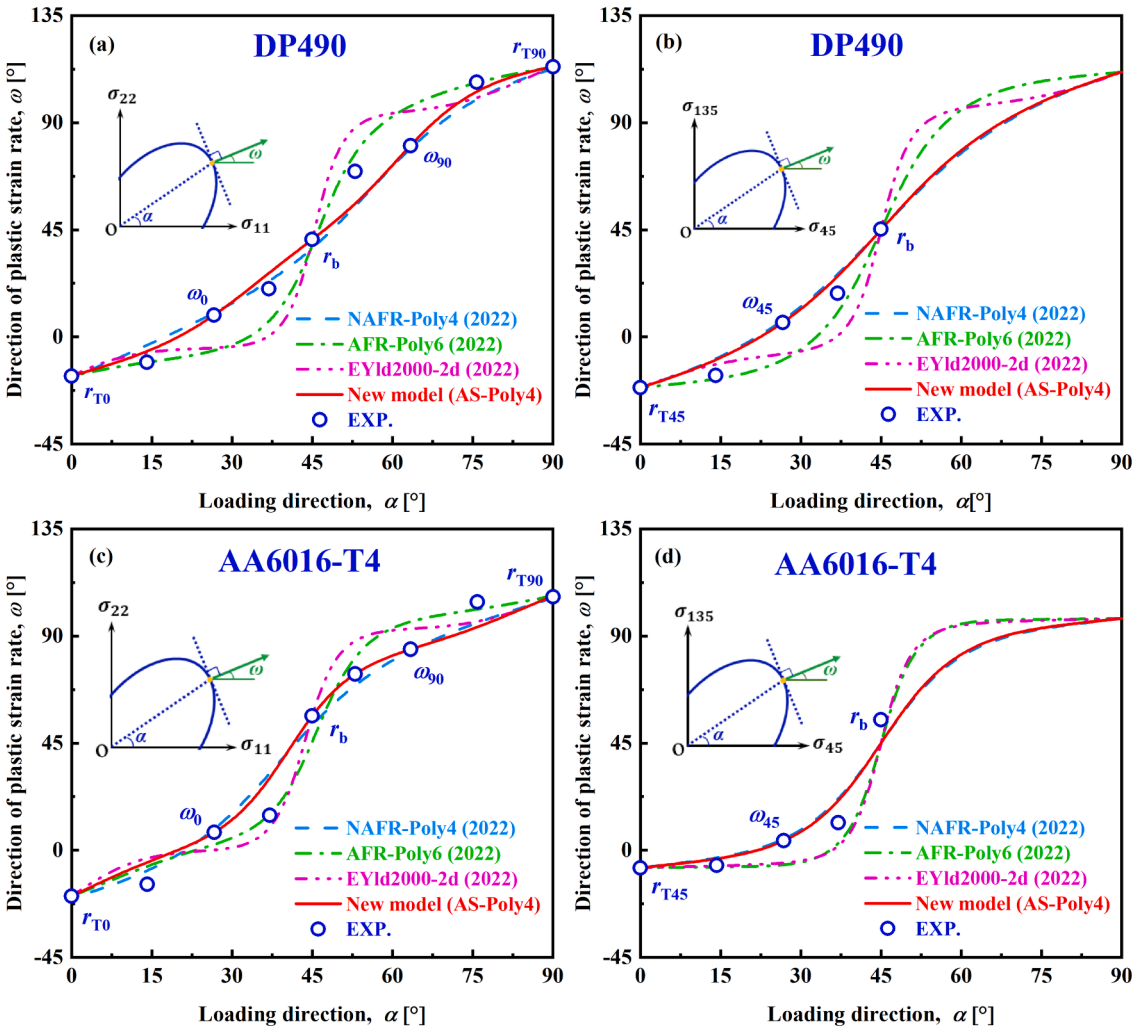

Fig. 11. DPSRs in the normal and diagonal planes of (a-b) DP490 and (c-d) AA6016-T4 at the initial yielding point, predicted by of the NAFR-Poly4, EYld2000-2d, AFR-Poly6, and new symmetric model.

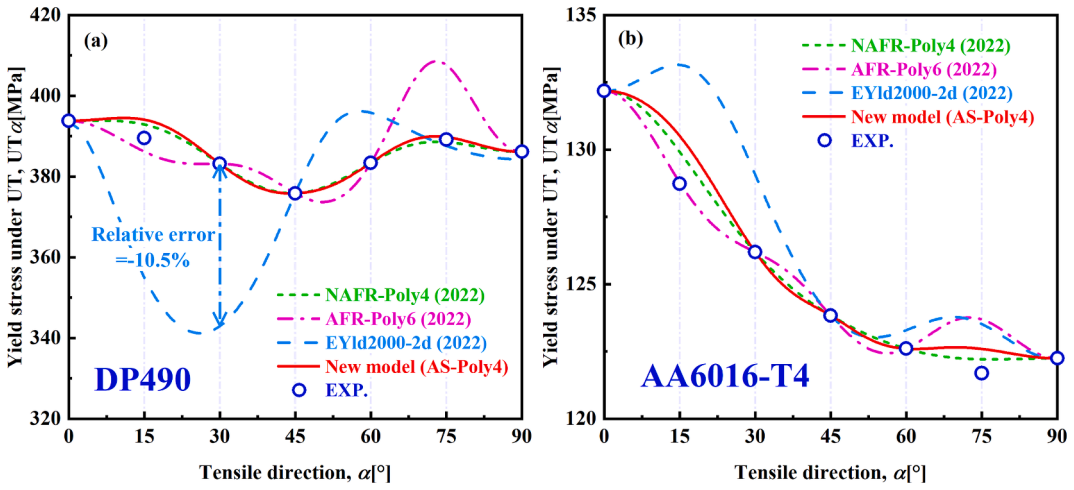

Fig. 12. UT yield stresses of (a) DP490 and (b) AA6016-T4 at the initial yielding point, predicted by the YSFs of the NAFR-Poly4, EYld2000-2d, AFR-Poly6, and new symmetric model.

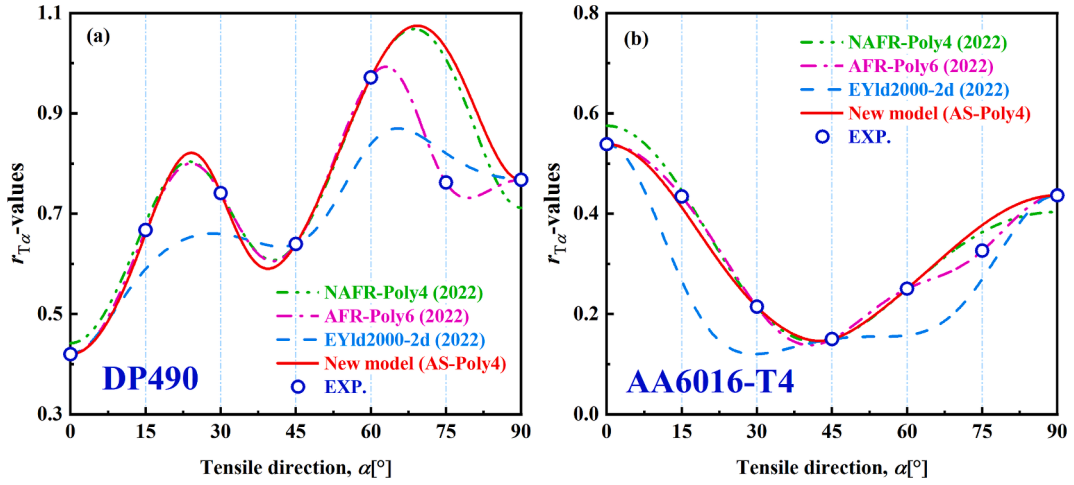

Fig. 13. $r_{T\alpha}$−values of (a) DP490 and (b) AA6016-T4 at the initial yielding point, predicted by the PPFs of the NAFR-Poly4, EYld2000-2d, AFR-Poly6, and new symmetric model.

This indicates that only assessing the prediction accuracy of Δ_{YSF}^{NP} is insufficient to examine the characterization ability of YSF. Incorporating Δ_{YSF}^{DP} into the evaluation standard based on Δ_{YSF}^{NP} can effectively reduce the risk of misjudging the description accuracy of YSF. To further examine the description ability of the four YSFs for DP490 and AA6016-T4, $\Delta_{YSF}^{\Omega}(\Omega = \text{UT, e-BT, NPS, SS})$ are quantitatively analyzed under different stress states. It can be observed that the prediction errors are mainly concentrated in Δ_{YSF}^{SS}. Specifically, the Δ_{YSF}^{SS} of DP490 and AA6016-T4 calculated by NAFR-Poly4 and AFR-Poly6 are up to 8.61 % and 6.07 % as well as 10.39 % and 10.76 %, respectively. Meanwhile, the Δ_{YSF}^{UT} calculated by EYld2000-2d reached 5.89 % for DP490 and 1.63 % for AA6016-T4. The calculated Δ_{YSF}^{NPS} reached 4.96 % for DP490 and 2.48 % for AA6016-T4. These prediction errors are significantly higher than those obtained from other YSFs, as shown in Fig. 14**(a2)** and **14 (b2)**. In conclusion, improving the description capability of anisotropic yielding behavior not only ensures the prediction accuracy of UT and e-BT loads and NP-YL but also allows for precise description of the SS stress state and DP-YL.

Subsequently, the ability of the PPFs of the NAFR-Poly4, EYld2000-2d, AFR-Poly6, and new symmetric model to predict the plastic flow behavior of DP490 and AA6016-T4 is quantitatively assessed. Eq. (34a) is used to calculate the *r*-value errors ($\Delta_{PPF}^{r_{T\alpha}}$) for all PPFs, and the prediction errors of DPSRs in the normal (Δ_{PPF}^{NP}) and diagonal planes (Δ_{PPF}^{DP}), and r_b ($\Delta_{PPF}^{r_b}$) are calculated using Eq. (34b).

$$\Delta_{PPF}^{r_{T\alpha}} = \frac{1}{k}\sum_{i=1}^{k}\left|\frac{r^{cal.}(i)}{r^{exp.}(i)} - 1\right| (\zeta = \text{T or C}) \tag{34a}$$

$$\Delta_{PPF}^{\Omega} = \sqrt{\frac{1}{k}\sum_{i=1}^{k}\left\{\frac{\zeta^{cal.}(i)}{\zeta^{exp.}(i)} - 1\right\}^2} (\Omega = \text{NP, DP, } r_b) \tag{34b}$$

$$\Delta_{PPF}^{ALL} = \Delta_{PPF}^{NP} + \Delta_{PPF}^{DP} \tag{34c}$$

where $\zeta^{cal.}$ and $\zeta^{exp.}$ represent calculated and experimental plastic flow-related data, respectively. Δ_{PPF}^{ALL} represents the overall prediction error of Δ_{PPF}^{NP} and Δ_{PPF}^{DP}; *k* is the number of loads employed in the calculation of plastic flow-related errors, where k values corresponding to $\Delta_{PPF}^{\Omega}(\Omega = \text{NP, DP, } r_{T\alpha}, r_b)$ are 9, 5, 7, and 1, respectively.

Fig. 15 shows the plastic flow-related prediction errors of DP490 and AA6016-T4 calculated by the PPFs of the NAFR-Poly4, EYld2000-2d, AFR-Poly6, and new symmetric model. The Δ_{PPF}^{ALL} values provided by the NAFR-Poly4 and new symmetric model are 10.92° and 9.68° for DP490, while 12.94° and 13.23° for AA6016-T4, respectively, indicating similar

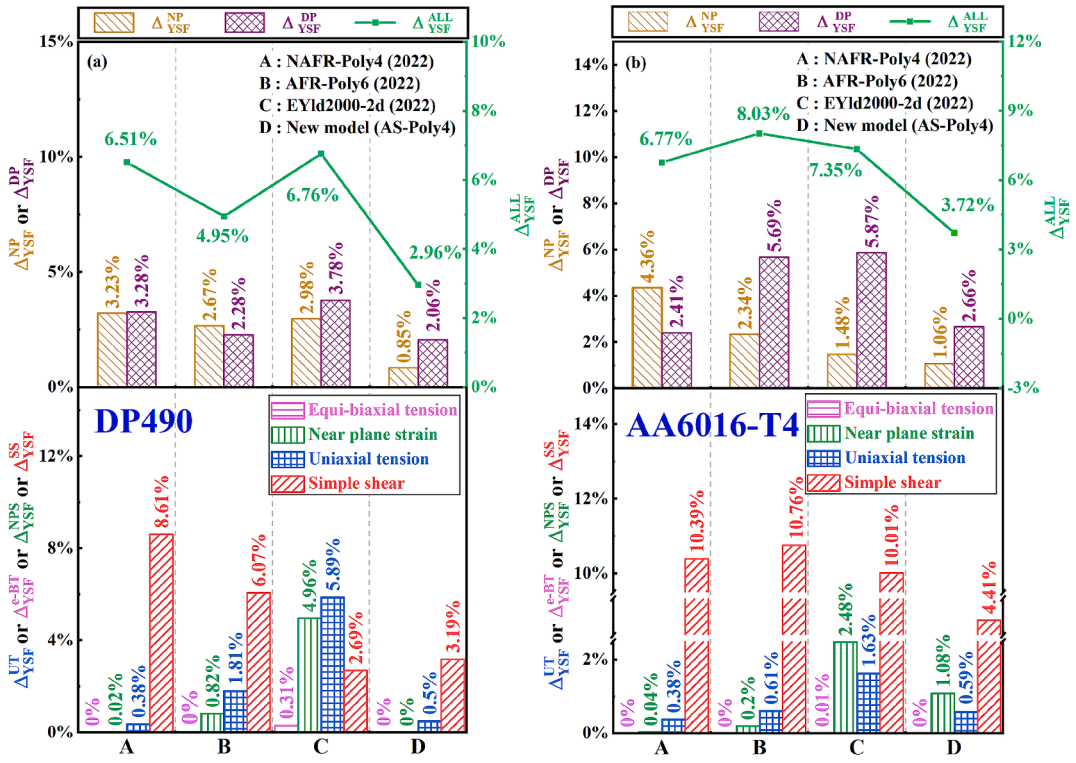

Fig. 14. Prediction errors associated with the yield stresses of (a) DP490 and (b) AA6016-T4 calculated by the YSFs of the NAFR-Poly4, EYld2000-2d, AFR-Poly6, and new symmetric model.

prediction accuracy in characterizing the DPSRs for two PPFs. In contrast, EYld2000-2d and AFR-Poly6 exhibit higher levels of Δ_{PPF}^{ALL}, especially for DP490, as shown in Fig. 15(a). Meanwhile, the Δ_{PPF}^{NP} and Δ_{PPF}^{DP} of the four PPFs follow a similar error distribution pattern as Δ_{PPF}^{ALL}. However, although the NAFR-Poly4 and new symmetric model employ consistent parameter identification procedures, NAFR-Poly4 provides higher $\Delta_{PPF}^{r_{T\alpha}}$ and $\Delta_{PPF}^{r_b}$ compared to the new symmetric model. This discrepancy is attributed to the optimization techniques used by NAFR-Poly4 and the lack of model flexibility. Therefore, the analytical PPF offers a significant advantage in characterizing the plastic anisotropy of the sheet metals. Although AFR-Poly6 achieves a zero-error level of characterization accuracy under UT loadings for both materials, it performs poorly in predicting plastic flow behavior under complex loadings. Considering that components are frequently subjected to complex stress states during the actual forming process, solely examining the $r_{T\alpha}$−value is insufficient to verify the validity of the PPF. Greater attention should be paid to the prediction accuracy in the DPSRs.

6. Results and discussion of the new asymmetric model

This section evaluates the ability of the new asymmetric model to characterize the asymmetric plastic anisotropy of DP490 and AA6016-T4, comparing it with several recently developed advanced yield criteria, i.e., CFI2023 [31], LAA2023 [4], and ZHC2023 [75]. The

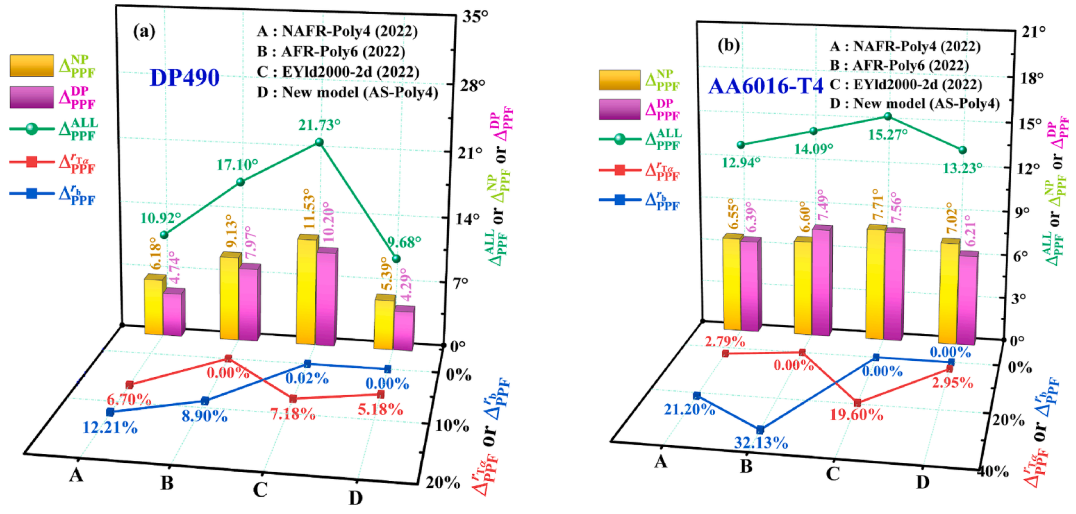

Fig. 15. Prediction errors associated with the plastic flow of (a) DP490 and (b) AA6016-T4 calculated by the PPFs of the NAFR-Poly4, EYld2000-2d, AFR-Poly6, and new symmetric model.

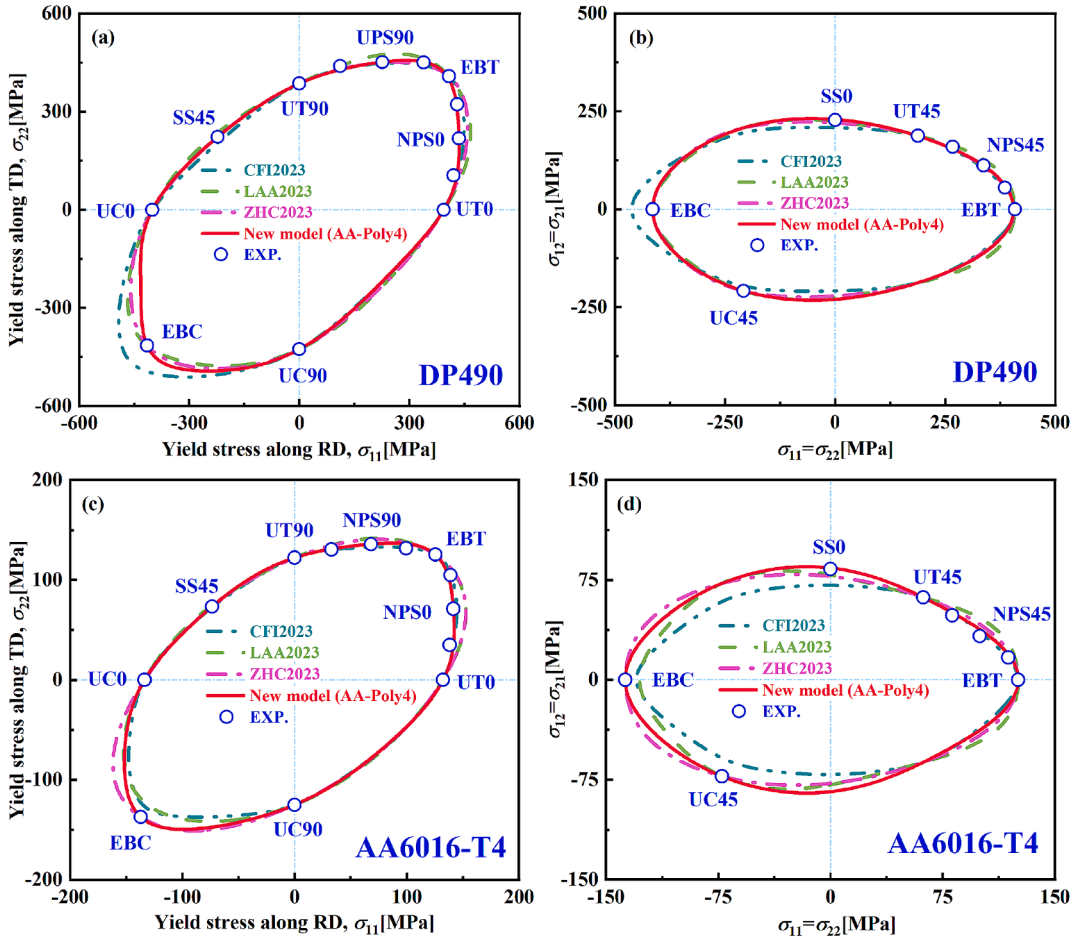

Fig. 16. Asymmetric NP-YLs and DP-YLs of (a-b) DP490 and (c-d) AA6016-T4 at the initial yielding point, predicted by the YSFs of the CFI2023, LAA2023, ZHC2023, and new asymmetric model.

corresponding UC experimental data can be found in Du et al. (2023b). Table 5 lists the compressive yield stresses and $r_{C\alpha}$−values of DP490 and AA6016-T4 at the initial yielding point. The calibration results for the anisotropic coefficients for all the mentioned yield criteria are listed in Tables D5-D8 in Appendix D.

Fig. 16 illustrates the asymmetric NP-YLs and DP-YLs of DP490 and AA6016-T4 at the initial yielding point of EPS = 0.002, as predicted by the YSFs of the CFI2023, LAA2023, ZHC2023, and new asymmetric model, alongside the experimental data for comparison. All examined asymmetric YSFs accurately predict the UT$\alpha(\alpha = 0, 45, 90)$, EBT, UC0, and UC90 of DP490 and AA6016-T4. However, CFI2023 exhibits notable prediction deviations for EBC and UC45 for both DP490 and AA6016-T4. The deviation is considered acceptable, given that these two stress states are not included in its calibration process. Similarly, although LAA2023 undergoes analytical calibration of anisotropic coefficients, it still displays significant prediction deviations for AA6016-T4, as shown in Fig. 16(c)-(d). This divergence may stem from the handling of the concave tendency in LAA2023, addressed through scaling the EBC value. Conversely, the ZHC2023 and new asymmetric model accurately capture the SD effect of two materials. Notably, a high-fidelity asymmetric YSF should not only consider the tension–compression asymmetry but also accurately describe the yield loci between the tensile-tensile and tension–compression regions. However, ZHC2023 deviates in predicting complex stress states between UT and EBT. Only the new asymmetric model maintains high-precision description ability, particularly evident in Fig. 16(a) and 16(c), thanks to the constraining effect of NPS and SS stress states on the yield loci. Hence, an effective asymmetric YSF should balance tension–compression asymmetry and accurately depict yield loci across different stress states.

Fig. 17 illustrates the asymmetric DPSRs in the normal and diagonal planes of DP490 and AA6016-T4 at the initial yielding point of EPS = 0.002, as predicted by the PPFs of the CFI2023, LAA2023, ZHC2023, and new asymmetric model, juxtaposed with the experimental data. ZHC2023 notably deviates from the DPSRs for two materials. While LAA2023 and CFI2023 offer more reasonable predictions for the DPSRs of DP490, as depicted in Fig. 17(a)-(b), their characterization of AA6016-T4 remains unsatisfactory (see Fig. 17(c)-(d)). In addition, only the new asymmetric model achieves highly accurate results for both investigated materials.

Fig. 18 illustrates the UT and UC yield stresses of DP490 and AA6016-T4 at the initial yielding point of EPS = 0.002, as predicted by the YSFs of the CFI2023, LAA2023, ZHC2023, and new asymmetric model, juxtaposed with the experimental data. While CFI2023, LAA2023, and ZHC2023 accurately predict UT$\alpha(\alpha = 0, 45, 90)$, the new asymmetric model excels in providing accurate characterizations of UT$\alpha(\alpha = 0,\ 30,\ 45,\ 60,\ 90)$, as shown in Fig. 18(a) and 18(c), attributed to the employment of more in-plane anisotropic coefficients. CFI2023 exhibits significant deviations in predicting UC anisotropy for both materials (see Fig. 18(b) and 18(d)), likely due to limitations in its

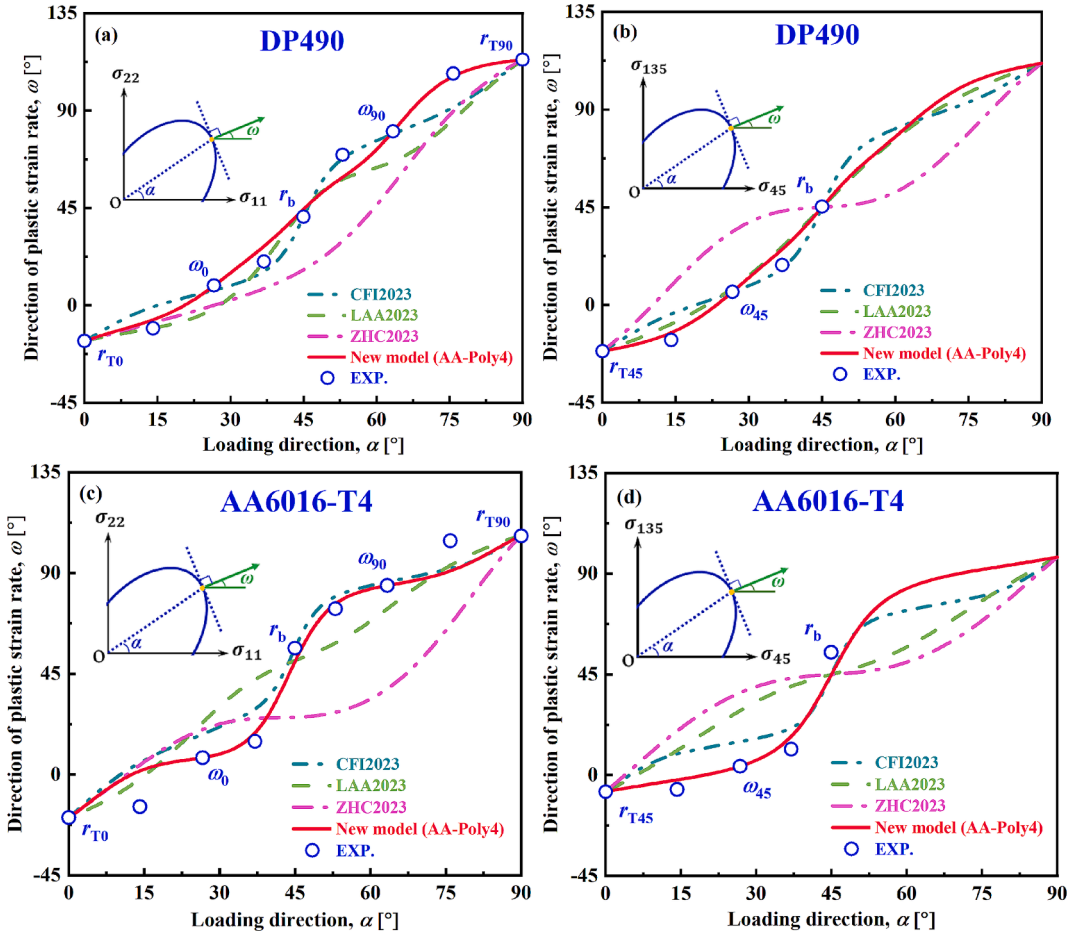

Fig. 17. Asymmetric DPSRs in the normal and diagonal planes of (a-b) DP490 and (c-d) AA6016-T4 at initial yield point, predicted by the PPFs of the CFI2023, LAA2023, ZHC2023, and new asymmetric model.

hydrostatic pressure modeling scheme, particularly in efficiently capturing UC45.

Fig. 19 depicts the $r_{T\alpha}$−values and $r_{C\alpha}$−values of DP490 and AA6016-T4 at the initial yielding point of EPS = 0.002, as predicted by the PPFs of the CFI2023, LAA2023, ZHC2023, and new asymmetric model, compared with the experimental data. There is an obvious deviation between experimental data and the $r_{T\alpha}$−values predicted by CFI2023, LAA2023, and ZHC2023 for DP490 (Fig. 19(a)). Additionally, CFI2023 accurately describes only the r_{C0} and r_{C90}, as shown in Fig. 19(b) and 19 (d), while LAA2023 provides accurate predictions for $r_{C\alpha}$−values due to its comprehensive calculation of both r_{C30} and r_{C60} (as listed in Table 5). ZHC2023 accurately describes $r_{C\alpha}(\alpha = 0, 45, 90)$, but slightly biases r_{C45} of AA6016-T4 (Fig. 19(d)), likely due to its prioritization of satisfying the convexity requirement of the plastic potential surface for AA6016-T4 over r_{C45}−value accuracy. Therefore, among all the examined asymmetric PPFs, only the new asymmetric model achieves accurate characterization of all $r_{C\alpha}$−values, with predicted $r_{T\alpha}$−values closely aligning with the experimental data.

For a quantitative assessment of the description ability regarding the asymmetric plastic anisotropy of DP490 and AA6016-T4 of the CFI2023, LAA2023, ZHC2023, and new asymmetric model, yield stress-related prediction errors, i.e., Δ_{YSF}^{NP}, Δ_{YSF}^{DP}, Δ_{YSF}^{UT}, and Δ_{YSF}^{UC}, as well as plastic flow-related prediction errors, i.e., Δ_{PPF}^{NP}, Δ_{PPF}^{DP}, $\Delta_{PPF}^{r_{T\alpha}}$, and $\Delta_{PPF}^{r_{C\alpha}}$, are computed using Eqs. (33)-(34). While r_{C30} and r_{C60} predicted by LAA2023 are used to calibrate the new asymmetric model, their data serve sorely to demonstrate the flexible characterization of the new asymmetric model and are excluded from error analysis, as is the case for EBC.

Fig. 20 shows predicted errors associated with the yield stress and plastic flow of DP490 and AA6016-T4 calculated by the CFI2023, LAA2023, ZHC2023, and the new asymmetric model. The Δ_{YSF}^{NP} calculated by LAA2023 for DP490 and AA6016-T4 are 3.28 % and 3.47 %, respectively, exhibiting the largest errors compared to other asymmetric YSFs. This is attributed to CFI2023 and ZHC2023 using shape control terms, while the new asymmetric model directly utilizes NPS loadings for parameter identification. However, the Δ_{YSF}^{DP} calculated by CFI2023 for both materials shows the largest error, as its shape control term mainly adjusts NP-YL curvature, neglecting DP-YL control. Comparatively, the Δ_{YSF}^{NP} value of DP490 calculated by CFI2023 compared to LAA2023 decreased by 6.4 %, while Δ_{YSF}^{DP} increased by 102.42 %, as shown in Fig. 20**(a1)**. This indicates that only adopting Δ_{YSF}^{NP} as a criterion to assess the asymmetric YSF has a high probability of triggering a misjudgment of the validity of the plastic models, which can be compensated for by incorporating Δ_{YSF}^{DP} into the assessment system. Regarding the plastic flow, the new asymmetric model exhibits minimal errors compared to other asymmetric PPFs for Δ_{PPF}^{NP} and Δ_{PPF}^{DP} of two materials, especially compared to ZHC2023, the Δ_{PPF}^{NP} and Δ_{PPF}^{DP} of DP490 are reduced by 76.47 % and 81.95 %, respectively, whereas the Δ_{PPF}^{NP} and Δ_{PPF}^{DP} of AA6016-T4 are reduced by 73.89 % and 77.04 %, respectively,

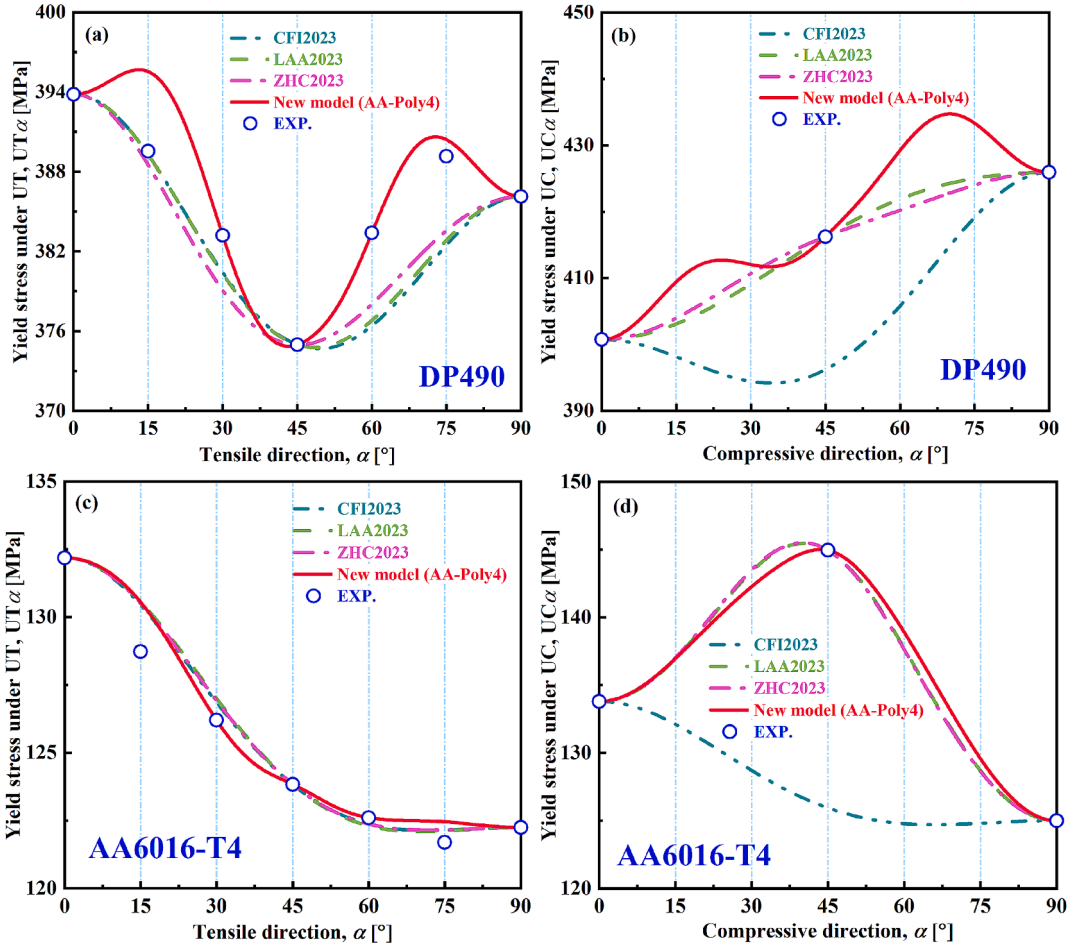

Fig. 18. UT and UC yield stresses of (a-b) DP490 and (c-d) AA6016-T4 at the initial yielding point, predicted by the YSFs of the CFI2023, LAA2023, ZHC2023, and new asymmetric model.

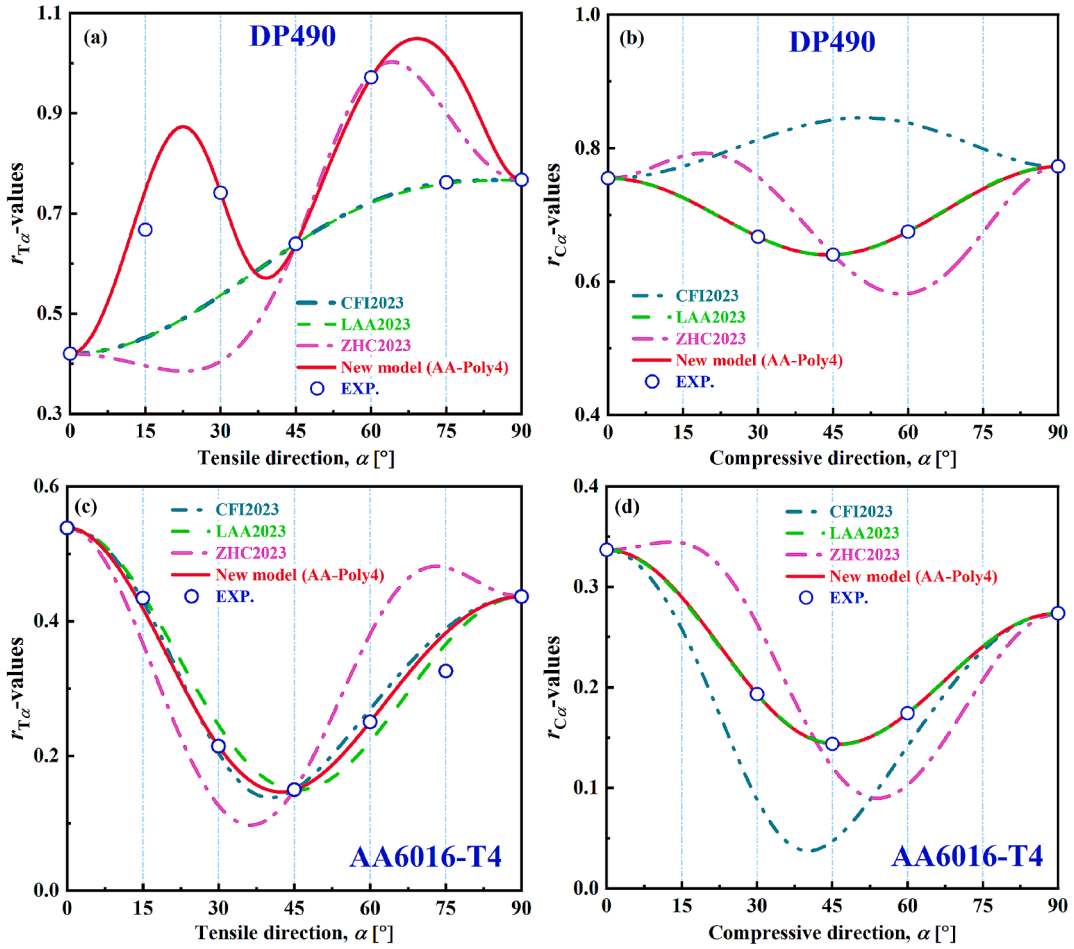

Fig. 19. $r_{T\alpha}$−values and $r_{C\alpha}$−values of (a-b) DP490 and (c-d) AA6016-T4 at initial yield point, predicted by the PPFs of the CFI2023, LAA2023, ZHC2023, and new asymmetric model.

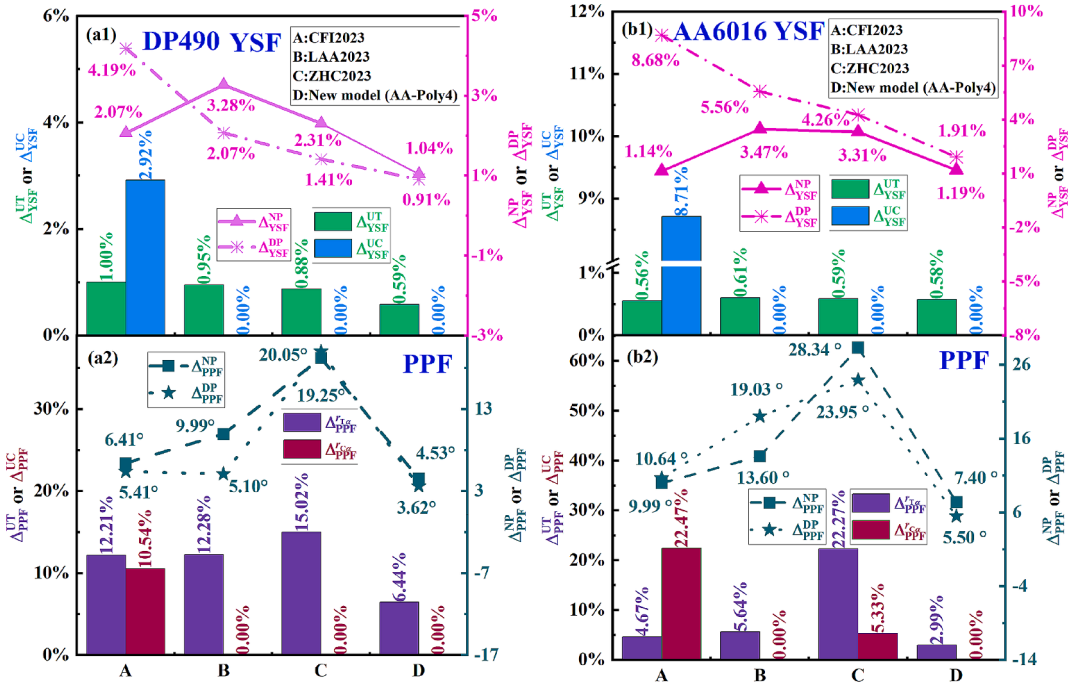

Fig. 20. Prediction errors related to yield stress and plastic flow of (a) DP490 and (b) AA6016-T4 calculated by the CFI2023, LAA2023, ZHC2023, and the new asymmetric model.

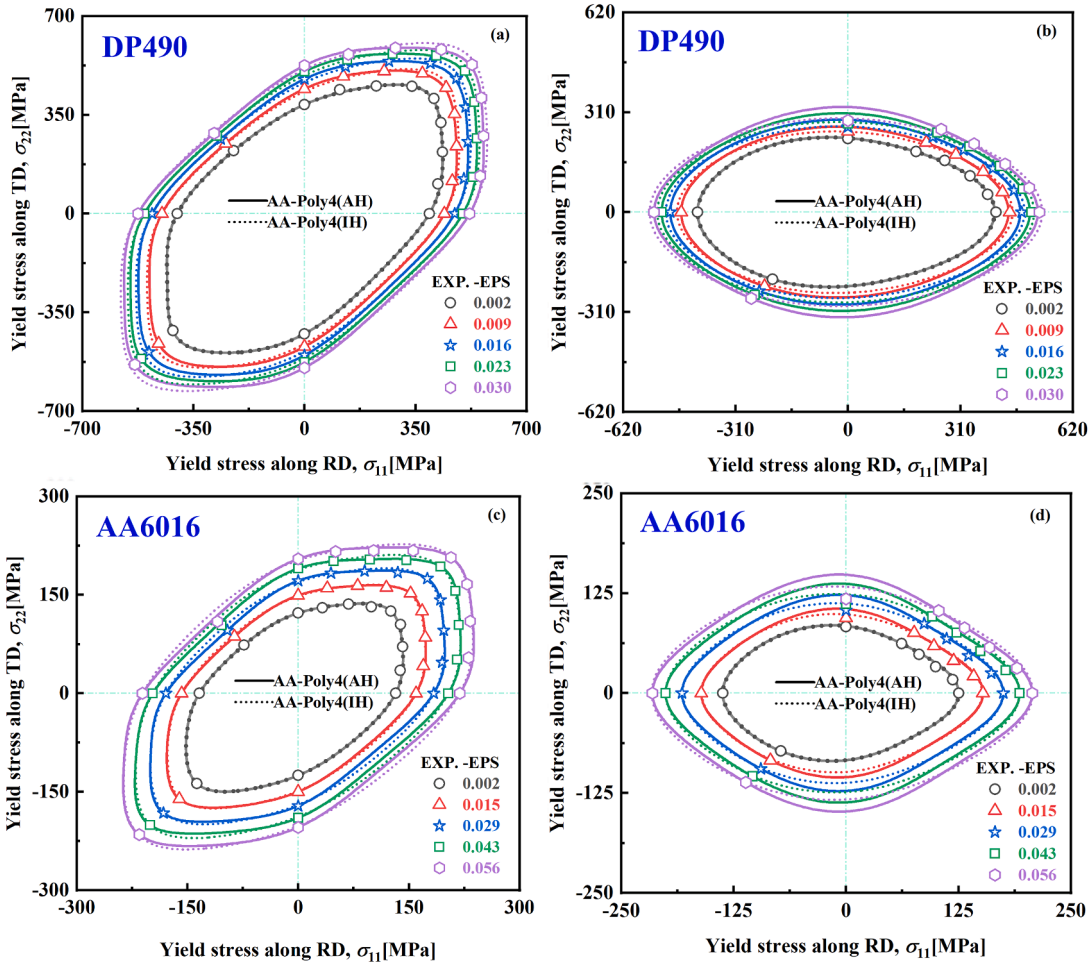

Fig. 21. Asymmetric NP-YLs and DP-YLs of (a-b) DP490 and (c-d) AA6016-T4 at various EPS levels, predicted by the YSF of the new asymmetric model.

as shown in Fig. 20**(a2)** and **20(b2)**. The overall prediction accuracy is greatly improved. In addition, although the four yield criteria show almost consistent Δ_{YSF}^{UT} for AA6016-T4, only the new asymmetric model provides the best characterization accuracy for Δ_{YSF}^{UT} and $\Delta_{PPF}^{r_{T\alpha}}$ of DP490, as well as $\Delta_{PPF}^{r_{T\alpha}}$ of AA6016-T4, at 0.59 %, 6.44 %, and 2.99 % respectively. Simultaneously, the new asymmetric model exhibits superior characterization accuracy for both yield loci and plastic strain rate directions in both normal and diagonal planes under complex loading conditions, as depicted in Figs. 16 and 17. Moreover, it accurately captures the SD effect of the materials with zero error, effectively addressing a significant gap in the current study.

7. Capture of subsequent yielding behavior under a wide range of stress states

This section delves into the capability of the proposed yield criteria to describe the plastic anisotropy of the investigated materials at various EPS levels. The new model has been examined under both isotropic hardening (IH) and anisotropic hardening concepts. Since the new symmetric and asymmetric models employ similar parameter identification procedures, the subsequent yielding behavior of DP490 and AA6016-T4 is solely described using the new asymmetric model. The hardening curves of DP490 and AA6016-T4 can be found in Appendix E.

Fig. 21 illustrates the asymmetric NP-YLs and DP-YLs of DP490 and AA6016-T4 at different EPS levels, as predicted by the YSF of the new asymmetric model, juxtaposed with the experimental data. It can be observed that, compared to experimental data of DP490, AA6016-T4 exhibits a more significant anisotropic evolution behavior, especially under the SS stress state. In addition, for DP490, the NP-YLs depicted by the YSF of the new asymmetric model consistently exhibit a high degree of alignment with the experimental data across all EPS levels, as shown in Fig. 21(a). Although addressing the concave tendency of high-order polynomial YSF, which leads to slight deviations of SS45 for AA6016-T4 under large plastic strain conditions, the characterization accuracy of SS45 remains satisfactory, as illustrated in Fig. 21(c). However, the shear anisotropic hardening behavior of DP490 and AA6016-T4 predicted by the YSF of the new asymmetric model deviates due to the non-employment of SS0 to calibrate the anisotropic coefficients, as observed in Fig. 21(b) and 21(d). In summary, the YSF of the new asymmetric model effectively captures the compressive yield stresses and provides an accurate depiction of subsequent yielding behavior under tensile stress states.

Fig. 22 displays the DPSRs in the normal and diagonal planes of DP490 and AA6016-T4 at two EPS levels, as predicted by the PPF of the new asymmetric model, juxtaposed with the experimental data. the new asymmetric model demonstrates commendable overall prediction

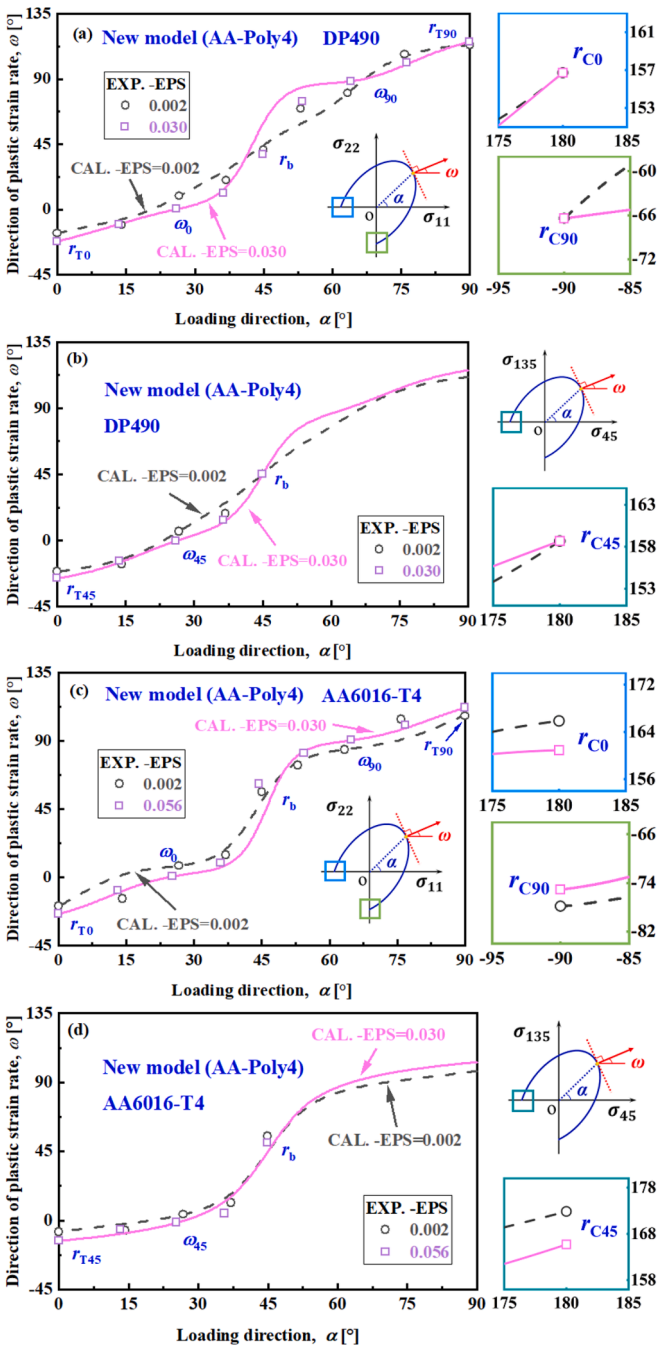

Fig. 22. DPSRs in the normal and diagonal planes of (a-b) DP490 and (c-d) AA6016-T4 at two EPS levels, predicted by the PPF of the new asymmetric model.

accuracy for both DPSRs in the normal plane (see Fig. 22(a) and 22(c)) and DPSRs in the diagonal plane (see Fig. 22(b) and 22(d)) of two metallic sheets. This accuracy can be attributed to the dynamic pinning effect of EPS-related $\omega_\alpha(\alpha = 0, 45, 90)$ on the DPSRs, particularly evident between UT to e-BT loadings. Moreover, the characterization results of the PPF of the new asymmetric model for the DPSRs under the UC stress state align perfectly with the experimental data. This indicates that the newly developed the PPF of the new asymmetric model not only consider the tension–compression asymmetry under different EPSs but also delivers high-precision characterization results for the DPSRs under complex stress states.

8. Conclusions

The new symmetric and asymmetric models are developed under the non-associated flow rule to characterize the anisotropy, strength differential (SD) effect, and subsequent yielding behavior of sheet metals, particularly enhancing the description ability under near-plane strain (NPS) and simple shear (SS) loadings. The new symmetric and asymmetric models offer a direct approach to determine the anisotropic coefficients of the yield stress and plastic potential functions using experimental sampling points, eliminating the need for interpolation and optimization techniques. Furthermore, the new convexity proof method is developed and evaluated against the Hessian matrix and GINCA methods to assess its advancement in describing the upper and lower limits of the anisotropic coefficients. The conclusions drawn are as follows:

(1) The new symmetric and asymmetric models outperform other investigated yield criteria in describing yield loci and directions of plastic strain rate for DP490 and AA6016-T4. The new asymmetric model excels in characterizing the SD effect and accurately describing anisotropic yield and plastic flow behavior under complex stress states.

(2) The new convexity proof method overcomes ambiguous identification results with the GINCA method, providing accurate convexity identification through simple geometric analysis while maintaining user-friendliness.

(3) Incorporating anisotropic yield and plastic flow test data under NPS stress state into the parameter calibration process improves the description accuracy of yield stress and plastic potential functions for plastic anisotropy under uniaxial tension to equi-biaxial tension loadings.

(4) The yield stress functions of the new symmetric and asymmetric models offer the most reasonable prediction of SS yield stresses compared to other yield criteria examined. However, further refinement is needed to enhance accuracy in characterizing anisotropy under SS loadings.

(5) Relying solely on the prediction error of yield locus in the normal plane for evaluating yield criterion modeling accuracy may lead to misjudgments. A comprehensive evaluation should also consider yield locus in the diagonal plane.

(6) The analytical technique in the parameter calibration procedure enables accurate prediction of selected loads, compensating for potential inconsistencies between experimental sampling points and mechanical properties calculated through optimization techniques. Additionally, it provides an accurate characterization of anisotropic hardening behavior across all equivalent plastic strain levels.

CRediT authorship contribution statement

Yanqiang Ren: Writing – original draft, Validation, Formal analysis, Data curation. **Kai Du:** Writing – review & editing, Visualization, Methodology, Funding acquisition. **Yong Hou:** Writing – review & editing, Visualization, Validation, Investigation, Funding acquisition. **Liying Song:** Visualization, Supervision. **Liang Sun:** Software. **Yanfeng Yang:** Investigation. **Wentao Zheng:** Supervision. **Xiaoguang Yuan:** Project administration, Funding acquisition.

Declaration of competing interest

The authors declare that they have no known competing financial interests or personal relationships that could have appeared to influence the work reported in this paper.

Acknowledgments

KD, XY, and YY acknowledge the financial support from the National Natural Science Foundation of China (Grant No. 52305396, 52371116 & 52205418). YH would like to thank the generous support from Alexander von Humboldt Foundation who awarded him a research fellowship at TU Dortmund.

Appendix A. Analytical anisotropic coefficient identification procedure for the YSF of the new asymmetric model

According to Eqs. (2) and (20a) and the stress components of UT0 and UT90, there are

$$A_1\mathrm{UT0}^6(\bar{\varepsilon}^{\mathrm{p}}) = \bar{\sigma}^6(\bar{\varepsilon}^{\mathrm{p}}) \tag{A1a}$$

$$A_7\mathrm{UT90}^6(\bar{\varepsilon}^{\mathrm{p}}) = \bar{\sigma}^6(\bar{\varepsilon}^{\mathrm{p}}) \tag{A1b}$$

Under e-BT stress state, combining Eqs. (2) and (20b), we have

$$A_1 + A_2 + A_3 + A_4 + A_5 + A_6 + A_7 = \left[\frac{\bar{\sigma}(\bar{\varepsilon}^{\mathrm{p}})}{\mathrm{EBT}(\bar{\varepsilon}^{\mathrm{p}})}\right]^6 \tag{A2}$$

Bringing the stress components of NPS0 and NPS90 into Eq. (2), we have

$$A_1 + p_0(\bar{\varepsilon}^{\mathrm{p}})A_2 + p_0^2(\bar{\varepsilon}^{\mathrm{p}})A_3 + p_0^3(\bar{\varepsilon}^{\mathrm{p}})A_4 + p_0^4(\bar{\varepsilon}^{\mathrm{p}})A_5 + p_0^5(\bar{\varepsilon}^{\mathrm{p}})A_6 + p_0^6(\bar{\varepsilon}^{\mathrm{p}})A_7 = \left[\frac{\bar{\sigma}(\bar{\varepsilon}^{\mathrm{p}})}{\mathrm{NPS0}(\bar{\varepsilon}^{\mathrm{p}})f_{\mathrm{TC}}(\boldsymbol{\sigma}_{\mathrm{NPS0}}, \bar{\varepsilon}^{\mathrm{p}})}\right]^6 \tag{A3a}$$

$$p_{90}^6(\bar{\varepsilon}^{\mathrm{p}})A_1 + p_{90}^5(\bar{\varepsilon}^{\mathrm{p}})A_2 + p_{90}^4(\bar{\varepsilon}^{\mathrm{p}})A_3 + p_{90}^3(\bar{\varepsilon}^{\mathrm{p}})A_4 + p_{90}^2(\bar{\varepsilon}^{\mathrm{p}})A_5 + p_{90}(\bar{\varepsilon}^{\mathrm{p}})A_6 + A_7 = \left[\frac{\bar{\sigma}(\bar{\varepsilon}^{\mathrm{p}})}{\mathrm{NPS90}(\bar{\varepsilon}^{\mathrm{p}})f_{\mathrm{TC}}(\boldsymbol{\sigma}_{\mathrm{NPS90}}, \bar{\varepsilon}^{\mathrm{p}})}\right]^6 \tag{A3b}$$

Under SS45 loading, Eq. (2) is re-expressed as

$$A_1 - A_2 + A_3 - A_4 + A_5 - A_6 + A_7 = \left[\frac{\bar{\sigma}(\bar{\varepsilon}^{\mathrm{p}})}{\mathrm{SS45}(\bar{\varepsilon}^{\mathrm{p}})f_{\mathrm{TC}}(\boldsymbol{\sigma}_{\mathrm{SS45}}, \bar{\varepsilon}^{\mathrm{p}})}\right]^6 \tag{A4}$$

The asymmetric anisotropic coefficients are defined as explicit expressions related to the EPS according to Eqs. (A1) − (A4).

$$A_1 = \left[\frac{\bar{\sigma}(\bar{\varepsilon}^{\mathrm{p}})}{\mathrm{UT0}(\bar{\varepsilon}^{\mathrm{p}})}\right]^6 = 1 \tag{A5a}$$

$$A_7 = \left[\frac{\bar{\sigma}(\bar{\varepsilon}^{\mathrm{p}})}{\mathrm{UT90}(\bar{\varepsilon}^{\mathrm{p}})}\right]^6 \tag{A5b}$$

$$\begin{bmatrix} A_2 \\ A_4 \\ A_5 \\ A_6 \end{bmatrix} = \begin{bmatrix} 1 & 1 & 1 & 1 \\ -1 & -1 & 1 & -1 \\ p_0(\bar{\varepsilon}^{\mathrm{p}}) & p_0^3(\bar{\varepsilon}^{\mathrm{p}}) & p_0^4(\bar{\varepsilon}^{\mathrm{p}}) & p_0^5(\bar{\varepsilon}^{\mathrm{p}}) \\ p_{90}^5(\bar{\varepsilon}^{\mathrm{p}}) & p_{90}^4(\bar{\varepsilon}^{\mathrm{p}}) & p_{90}^3(\bar{\varepsilon}^{\mathrm{p}}) & p_{90}(\bar{\varepsilon}^{\mathrm{p}}) \end{bmatrix}^{-1} \begin{bmatrix} \Gamma_{\mathrm{EBT}} \\ \Gamma_{\mathrm{SS45}} \\ \Gamma_{\mathrm{NPS0}} \\ \Gamma_{\mathrm{NPS90}} \end{bmatrix} \tag{A5c}$$

with

$$\Gamma_{\mathrm{EBT}} = \left[\frac{\bar{\sigma}(\bar{\varepsilon}^{\mathrm{p}})}{\mathrm{EBT}(\bar{\varepsilon}^{\mathrm{p}})}\right]^6 - A_1 - A_3 - A_7 \tag{A5d}$$

$$\Gamma_{\mathrm{SS45}} = \left[\frac{\bar{\sigma}(\bar{\varepsilon}^{\mathrm{p}})}{\mathrm{SS45}(\bar{\varepsilon}^{\mathrm{p}})f_{\mathrm{TC}}(\boldsymbol{\sigma}_{\mathrm{SS45}}, \bar{\varepsilon}^{\mathrm{p}})}\right]^6 - A_1 - A_3 - A_7 \tag{A5e}$$

$$\Gamma_{\mathrm{NPS0}} = \left[\frac{\bar{\sigma}(\bar{\varepsilon}^{\mathrm{p}})}{\mathrm{NPS0}(\bar{\varepsilon}^{\mathrm{p}})f_{\mathrm{TC}}(\boldsymbol{\sigma}_{\mathrm{NPS0}}, \bar{\varepsilon}^{\mathrm{p}})}\right]^6 - A_1 - p_0^2(\bar{\varepsilon}^{\mathrm{p}})A_3 - p_0^6(\bar{\varepsilon}^{\mathrm{p}})A_7 \tag{A5f}$$

$$\Gamma_{\mathrm{NPS90}} = \left[\frac{\bar{\sigma}(\bar{\varepsilon}^{\mathrm{p}})}{\mathrm{NPS90}(\bar{\varepsilon}^{\mathrm{p}})f_{\mathrm{TC}}(\boldsymbol{\sigma}_{\mathrm{NPS90}}, \bar{\varepsilon}^{\mathrm{p}})}\right]^6 - p_{90}^6(\bar{\varepsilon}^{\mathrm{p}})A_1 - p_{90}^4(\bar{\varepsilon}^{\mathrm{p}})A_3 - A_7 \tag{A5g}$$

The shear stress function of the YSF of the new asymmetric model possesses four anisotropic coefficients and will be analytically calibrated using experimental UT30, UT45, UT60, and NPS45. Combining Eqs. (2) and (18), we have

$$\nu_8(\alpha, p)A_8 + \nu_9(\alpha, p)A_9 + \nu_{10}(\alpha, p)A_{10} + \nu_{11}(\alpha, p)A_{11} = \delta_y(\alpha, p) \tag{A6a}$$

with

$$\delta_y(\alpha,p)=\left[\frac{\overline{\sigma}(\overline{\varepsilon}^{\mathrm{p}})}{\mathrm{NPS}\alpha(\overline{\varepsilon}^{\mathrm{p}})f_{\mathrm{TC}}(\boldsymbol{\sigma}_{\mathrm{NPS}\alpha},\overline{\varepsilon}^{\mathrm{p}})}\right]^4-\sum_y(\alpha,p) \tag{A6b}$$

$$\sum_y(\alpha,p)=\begin{bmatrix}A_1\nu_1(\alpha,p)+A_2\nu_2(\alpha,p)+A_3\nu_3(\alpha,p)+A_4\nu_4(\alpha,p)\\+A_5\nu_5(\alpha,p)+A_6\nu_6(\alpha,p)+A_7\nu_7(\alpha,p)\end{bmatrix}^{\frac{2}{3}} \tag{A6c}$$

$$\begin{cases}\nu_1(\alpha,p)=\left[\cos^2\alpha+p_\alpha(\overline{\varepsilon}^{\mathrm{p}})\sin^2\alpha\right]^6\\ \nu_2(\alpha,p)=\left[\cos^2\alpha+p_\alpha(\overline{\varepsilon}^{\mathrm{p}})\sin^2\alpha\right]^5\left[\sin^2\alpha+p_\alpha(\overline{\varepsilon}^{\mathrm{p}})\cos^2\alpha\right]\\ \nu_3(\alpha,p)=\left[\cos^2\alpha+p_\alpha(\overline{\varepsilon}^{\mathrm{p}})\sin^2\alpha\right]^4\left[\sin^2\alpha+p_\alpha(\overline{\varepsilon}^{\mathrm{p}})\cos^2\alpha\right]^2\\ \nu_4(\alpha,p)=\left[\cos^2\alpha+p_\alpha(\overline{\varepsilon}^{\mathrm{p}})\sin^2\alpha\right]^3\left[\sin^2\alpha+p_\alpha(\overline{\varepsilon}^{\mathrm{p}})\cos^2\alpha\right]^3\\ \nu_5(\alpha,p)=\left[\cos^2\alpha+p_\alpha(\overline{\varepsilon}^{\mathrm{p}})\sin^2\alpha\right]^2\left[\sin^2\alpha+p_\alpha(\overline{\varepsilon}^{\mathrm{p}})\cos^2\alpha\right]^4\\ \nu_6(\alpha,p)=\left[\cos^2\alpha+p_\alpha(\overline{\varepsilon}^{\mathrm{p}})\sin^2\alpha\right]\left[\sin^2\alpha+p_\alpha(\overline{\varepsilon}^{\mathrm{p}})\cos^2\alpha\right]^5\\ \nu_7(\alpha,p)=\left[\sin^2\alpha+p_\alpha(\overline{\varepsilon}^{\mathrm{p}})\cos^2\alpha\right]^6\\ \nu_8(\alpha,p)=\left[\cos^2\alpha+p_\alpha(\overline{\varepsilon}^{\mathrm{p}})\sin^2\alpha\right]^2\{[1-p_\alpha(\overline{\varepsilon}^{\mathrm{p}})]\sin\alpha\cos\alpha\}^2\\ \nu_9(\alpha,p)=\left[\cos^2\alpha+p_\alpha(\overline{\varepsilon}^{\mathrm{p}})\sin^2\alpha\right]\left[\sin^2\alpha+p_\alpha(\overline{\varepsilon}^{\mathrm{p}})\cos^2\alpha\right]\\ \cdot\{[1-p_\alpha(\overline{\varepsilon}^{\mathrm{p}})]\sin\alpha\cos\alpha\}^2\\ \nu_{10}(\alpha,p)=\left[\sin^2\alpha+p_\alpha(\overline{\varepsilon}^{\mathrm{p}})\cos^2\alpha\right]^2\{[1-p_\alpha(\overline{\varepsilon}^{\mathrm{p}})]\sin\alpha\cos\alpha\}^2\\ \nu_{11}(\alpha,p)=\{[1-p_\alpha(\overline{\varepsilon}^{\mathrm{p}})]\sin\alpha\cos\alpha\}^4\end{cases} \tag{A6d}$$

Making $p_\alpha=0$ and $f_{\mathrm{TC}}(\boldsymbol{\sigma}_{\mathrm{NPS}\alpha},\overline{\varepsilon}^{\mathrm{p}})=f_{\mathrm{TC}}(\boldsymbol{\sigma}_{\mathrm{UT}\alpha},\overline{\varepsilon}^{\mathrm{p}})=1$, and replacing NPS$\alpha$ with UTα, Eq. (A6) will degenerate into a functional expression of the UT stress state. Under UT and NPS loadings, through Eq. (A10), the explicit expression for the anisotropic coefficients A_8, A_9, A_{10}, and A_{11} is written as

$$\begin{bmatrix}A_8\\A_9\\A_{10}\\A_{11}\end{bmatrix}=\begin{bmatrix}\nu_8(\alpha_1)&\nu_9(\alpha_1)&\nu_{10}(\alpha_1)&\nu_{11}(\alpha_1)\\ \nu_8(\alpha_2)&\nu_9(\alpha_2)&\nu_{10}(\alpha_2)&\nu_{11}(\alpha_2)\\ \nu_8(\alpha_3)&\nu_9(\alpha_3)&\nu_{10}(\alpha_3)&\nu_{11}(\alpha_3)\\ \nu_8(\alpha_4,p_4)&\nu_9(\alpha_4,p_4)&\nu_{10,}(\alpha_4,p_4)&\nu_{11}(\alpha_4,p_4)\end{bmatrix}^{-1}\begin{bmatrix}\delta_8(\alpha_1)\\\delta_9(\alpha_2)\\\delta_{10}(\alpha_3)\\\delta_{11}(\alpha_4,p_4)\end{bmatrix} \tag{A7}$$

where $\{\alpha_1,\alpha_2,\alpha_3,\ \alpha_4\}=\{30,45,60,45\}$. The anisotropic coefficient A_3 will be employed as a convexity control parameter to adjust the convexity of the yield surface, which is similar to the determination of the convexity control parameter κ_3 of the YSF of the new symmetric model. Simultaneously, the yield surface described by the YSF of the new asymmetric model has been examined by the new convexity proof method.

Appendix B. First-order partial derivatives of the PPF of the new symmetric model

The first-order partial derivatives of the normal principal stress function $P_{\mathrm{Principal}}(\boldsymbol{\sigma})$ of the PPF of the new symmetric model are written as

$$\frac{\partial P_{\mathrm{Principal}}(\boldsymbol{\sigma})}{\partial\sigma_{11}}=6\sigma_{11}^5\kappa_1+5\sigma_{11}^4\sigma_{22}\kappa_2+4\sigma_{11}^3\sigma_{22}^2\kappa_3+3\sigma_{11}^2\sigma_{22}^3\kappa_4+2\sigma_{11}\sigma_{22}^4\kappa_5+\sigma_{22}^5\kappa_6 \tag{B1a}$$

$$\frac{\partial P_{\mathrm{Principal}}(\boldsymbol{\sigma})}{\partial\sigma_{22}}=\sigma_{11}^5\kappa_2+2\sigma_{11}^4\sigma_{22}\kappa_3+3\sigma_{11}^3\sigma_{22}^2\kappa_4+4\sigma_{11}^2\sigma_{22}^3\kappa_5+5\sigma_{11}\sigma_{22}^4\kappa_6+6\sigma_{22}^5\kappa_7 \tag{B1b}$$

$$\frac{\partial P_{\mathrm{Principal}}(\boldsymbol{\sigma})}{\partial\sigma_{12}}=0 \tag{B1c}$$

The first-order partial derivatives of the shear stress function $f_{\mathrm{Shear}}(\boldsymbol{\sigma})$ are shown as

$$\frac{\partial P_{\mathrm{Shear}}(\boldsymbol{\sigma})}{\partial\sigma_{11}}=(2\kappa_8\sigma_{11}+\kappa_9\sigma_{22})\sigma_{12}^2 \tag{B2a}$$

$$\frac{\partial P_{\mathrm{Shear}}(\boldsymbol{\sigma})}{\partial\sigma_{22}}=(\kappa_9\sigma_{11}+2\kappa_{10}\sigma_{22})\sigma_{12}^2 \tag{B2b}$$

$$\frac{\partial P_{\mathrm{Shear}}(\boldsymbol{\sigma})}{\partial\sigma_{12}}=2\left(\kappa_8\sigma_{11}^2+\kappa_9\sigma_{11}\sigma_{22}+\kappa_{10}\sigma_{22}^2\right)\sigma_{12}+4\kappa_{11}\sigma_{12}^3 \tag{B2c}$$

Combining Eqs. (B1) − (B2), the first-order partial derivatives of the PPF of the new symmetric model are expressed as

$$\frac{\partial P_{\mathrm{Sym.}}(\boldsymbol{\sigma})}{\partial\sigma_{ij}}=\frac{2}{3f_{\mathrm{Principal}}^{1/3}(\boldsymbol{\sigma})}\frac{\partial f_{\mathrm{Principal}}(\boldsymbol{\sigma})}{\partial\sigma_{ij}}+\frac{\partial f_{\mathrm{Shear}}(\boldsymbol{\sigma})}{\partial\sigma_{ij}} \tag{B3}$$

where $i,j=1,2$ and $\sigma_{12}=\sigma_{21}$.

Appendix C. Identification program of analytical anisotropic coefficients of the PPF of the new asymmetric model

Bringing the stress components of UT0 and UC0 into Eq. (3), it can be determined that the anisotropic coefficients A_1 and A_{10} of the PPF of the new asymmetric model are constantly equal to the constant 1. Under UT loading along RD, according to Eqs. (3) and (22), there is

$$A_2 = 2 - \frac{8r_{\mathrm{T0}}(\bar{\varepsilon}^{\mathrm{p}})}{r_{\mathrm{T0}}(\bar{\varepsilon}^{\mathrm{p}}) + 1} \tag{C1}$$

Similarly, under UC stress state along RD, A_{11} can be explicitly expressed as

$$A_{11} = 2 - \frac{8r_{\mathrm{C0}}(\bar{\varepsilon}^{\mathrm{p}})}{1 + r_{\mathrm{C0}}(\bar{\varepsilon}^{\mathrm{p}})} \tag{C2}$$

Combining r_{C90}, Eqs. (3) and (22), we have

$$A_{13} = 2\frac{1 - 3r_{\mathrm{C90}}(\bar{\varepsilon}^{\mathrm{p}})}{1 + r_{\mathrm{C90}}(\bar{\varepsilon}^{\mathrm{p}})}A_{14} \tag{C3}$$

Bringing the stress components of r_{T90} into Eq. (22), there is

$$\psi_3(r_{\mathrm{T90}})A_3 + \psi_4(r_{\mathrm{T90}})A_4 + \psi_5(r_{\mathrm{T90}})A_5 = \delta_r(r_{\mathrm{T90}}) \tag{C4a}$$

with

$$\delta_r(r_{\mathrm{T90}}) = 0 \tag{C4b}$$

$$\psi_3(r_{\mathrm{T90}}) = 0 \tag{C4c}$$

$$\psi_4(r_{\mathrm{T90}}) = r_{\mathrm{T90}}(\bar{\varepsilon}^{\mathrm{p}}) + 1 \tag{C4d}$$

$$\psi_5(r_{\mathrm{T90}}) = 6r_{\mathrm{T90}}(\bar{\varepsilon}^{\mathrm{p}}) - 2 \tag{C4e}$$

Under NPS stress state, the DPSR is defined as

$$\tan[w_\alpha(\bar{\varepsilon}^{\mathrm{p}})]\frac{\partial P_{\mathrm{Asym.}}(\boldsymbol{\sigma})}{\partial \sigma_x} - \frac{\partial P_{\mathrm{Asym.}}(\boldsymbol{\sigma})}{\partial \sigma_y} = 0 \tag{C5}$$

The derivation of the directions of plastic strain rate under NPS loadings is complex. To facilitate the presentation below, the first-order partial derivatives of the weighting factor w, the fourth-order polynomial function $f^{(-1)}_{\mathrm{Poly4}}(\boldsymbol{\sigma})$, and the stress principal values X_1 and X_2 are provided in advance. Firstly, the first-order partial derivatives of ω are written as

$$\frac{\partial \omega}{\partial \sigma_{ij}} = \frac{3\sqrt{3}}{4J_2^3}\left(\sqrt{J_2^3}\,\frac{\partial J_3}{\partial \sigma_{ij}} - \frac{3J_3\sqrt{J_2}}{2}\frac{\partial J_2}{\partial \sigma_{ij}}\right)(i,j = 1,2) \tag{C6a}$$

with

$$\frac{\partial J_2}{\sigma_{11}} = \frac{2\sigma_{11} - \sigma_{22}}{3} \tag{C6b}$$

$$\frac{\partial J_2}{\sigma_{22}} = \frac{2\sigma_{22} - \sigma_{11}}{3} \tag{C6c}$$

$$\frac{\partial J_2}{\sigma_{12}} = 2\sigma_{12} \tag{C6d}$$

$$\frac{\partial J_3}{\sigma_{11}} = \frac{\sigma_{12}^2}{3} - \frac{2\sigma_{11}\sigma_{22} + \sigma_{22}^2 - 2\sigma_{11}^2}{9} \tag{C6e}$$

$$\frac{\partial J_3}{\sigma_{22}} = \frac{\sigma_{12}^2}{3} - \frac{2\sigma_{11}\sigma_{22} + \sigma_{11}^2 - 2\sigma_{22}^2}{9} \tag{C6f}$$

$$\frac{\partial J_3}{\sigma_{12}} = \frac{2(\sigma_{11} + \sigma_{22})\sigma_{12}}{3} \tag{C6g}$$

The first-order partial derivatives of the fourth-order polynomial function are expressed as:

$$\frac{\partial f^{(-1)}_{\mathrm{Poly4}}(\boldsymbol{\sigma})}{\partial \sigma_{11}} = 4A_{10}\sigma_{11}^3 + 3A_{11}\sigma_{11}^2\sigma_{22} + 2A_{12}\sigma_{11}\sigma_{22}^2 + A_{13}\sigma_{22}^3 + (2A_{15}\sigma_{11} + A_{16}\sigma_{22})\sigma_{12}^2 \tag{C7a}$$

$$\frac{\partial f^{(-1)}_{\mathrm{Poly4}}(\boldsymbol{\sigma})}{\partial \sigma_{22}} = A_{11}\sigma_{11}^3 + 2A_{12}\sigma_{11}^2\sigma_{22} + 3A_{13}\sigma_{11}\sigma_{22}^2 + 4A_{14}\sigma_{22}^3 + (A_{16}\sigma_{11} + 2A_{17}\sigma_{22})\sigma_{12}^2 \tag{C7b}$$

$$\frac{\partial f^{(-1)}_{\mathrm{Poly4}}(\boldsymbol{\sigma})}{\partial \sigma_{12}} = 2\left(A_{15}\sigma_{11}^2 + A_{16}\sigma_{11}\sigma_{22} + A_{17}\sigma_{22}^2\right)\sigma_{12} + 4A_{18}\sigma_{12}^3 \tag{C7c}$$

The first-order partial derivatives of X_1 and X_2 are shown as

$$\frac{\partial X_{1,2}}{\partial \sigma_{11}} = \frac{1}{2} \pm \frac{(\sigma_{11} - \sigma_{22})}{4} \left[\left(\frac{\sigma_{11} - \sigma_{22}}{2} \right)^2 + \sigma_{12}^2 \right]^{-\frac{1}{2}} \tag{C8a}$$

$$\frac{\partial X_{1,2}}{\partial \sigma_{22}} = \frac{1}{2} \mp \frac{(\sigma_{11} - \sigma_{22})}{4} \left[\left(\frac{\sigma_{11} - \sigma_{22}}{2} \right)^2 + \sigma_{12}^2 \right]^{-\frac{1}{2}} \tag{C8b}$$

$$\frac{\partial X_{1,2}}{\partial \sigma_{12}} = \pm \sigma_{12} \left[\left(\frac{\sigma_{11} - \sigma_{22}}{2} \right)^2 + \sigma_{12}^2 \right]^{-\frac{1}{2}} \tag{C8c}$$

By taking Eq. (17) into Eqs. (3), (C5) − (C8), there is

$$\psi_6(\alpha,p)A_6 + \psi_7(\alpha,p)A_7 + \psi_8(\alpha,p)A_8 + \psi_9(\alpha,p)A_9 = \delta_r(\alpha,p) \tag{C9a}$$

with

$$\begin{aligned} \delta_r(\alpha,p) = &-\psi_1(\alpha,p)A_1 - \psi_2(\alpha,p)A_2 - \psi_3(\alpha,p)A_3 - \psi_4(\alpha,p)A_4 \\ &-\psi_5(\alpha,p)A_5 - \mathrm{E_1M_{11}} - \mathrm{E_2M_{22}} - \mathrm{E_3M_{12}} \end{aligned} \tag{C9b}$$

$$\psi_k(\alpha,p) = E_1\Pi_{11,k} + E_2\Pi_{22,k} + E_3\Pi_{12,k} (k = 1,2,\ldots,9) \tag{C9c}$$

with

$$\begin{bmatrix} E_1 \\ E_2 \\ E_3 \end{bmatrix} = \begin{bmatrix} \cos^2\alpha & \sin^2\alpha \\ \sin^2\alpha & \cos^2\alpha \\ \cos\alpha\sin\alpha & -\cos\alpha\sin\alpha \end{bmatrix} \begin{bmatrix} \tan(\omega_\alpha(\bar{\varepsilon}^{\mathrm{p}})) \\ -1 \end{bmatrix} \tag{C9d}$$

$$M_{ij} = \begin{Bmatrix} [1-\omega_\alpha(\bar{\varepsilon}^{\mathrm{p}})] f^{(-1)}_{\mathrm{Hosford}}(\boldsymbol{\sigma}) \dfrac{\partial f^{(-1)}_{\mathrm{Poly4}}(\boldsymbol{\sigma})}{\partial \sigma_{ij}} + \\ \left[[1-\omega_\alpha(\bar{\varepsilon}^{\mathrm{p}})] \dfrac{\partial f^{(-1)}_{1}(\boldsymbol{\sigma})}{\partial \sigma_{ij}} - \dfrac{\partial \omega}{\partial \sigma_{ij}} f^{(-1)}_{\mathrm{Hosford}}(\boldsymbol{\sigma}) \right] \\ \left[f^{(-1)}_{\mathrm{Principal}}(\boldsymbol{\sigma}) + f^{(-1)}_{\mathrm{Shear}}(\boldsymbol{\sigma}) \right] \end{Bmatrix} \left[\frac{\mathrm{UT0}(\bar{\varepsilon}^{\mathrm{p}})}{\mathrm{UC0}(\bar{\varepsilon}^{\mathrm{p}})} \right]^8 (i,j = 1,2) \tag{C9e}$$

$$\begin{cases} \Pi_{11,1} = 4\sigma_{11}^3\omega_\alpha f^{(+1)}_{\mathrm{Hosford}}(\boldsymbol{\sigma}) + \sigma_{11}^4 e_{11}^{(+1)} \\ \Pi_{11,2} = 3\sigma_{11}^2\sigma_{22}\omega_\alpha f^{(+1)}_{\mathrm{Hosford}}(\boldsymbol{\sigma}) + \sigma_{11}^3\sigma_{22} e_{11}^{(+1)} \\ \Pi_{11,\,3} = 2\sigma_{11}\sigma_{22}^2\omega_\alpha f^{(+1)}_{\mathrm{Hosford}}(\boldsymbol{\sigma}) + \sigma_{11}^2\sigma_{22}^2 e_{11}^{(+1)} \\ \Pi_{11,\,4} = \sigma_{22}^3\omega_\alpha f^{(+1)}_{\mathrm{Hosford}}(\boldsymbol{\sigma}) + \sigma_{11}\sigma_{22}^3 e_{11}^{(+1)} \\ \Pi_{11,\,5} = \sigma_{22}^4 e_{11}^{(+1)} \\ \Pi_{11,\,6} = 2\sigma_{11}\sigma_{12}^2\omega_\alpha f^{(+1)}_{\mathrm{Hosford}}(\boldsymbol{\sigma}) + \sigma_{11}^2\sigma_{12}^2 e_{11}^{(+1)} \\ \Pi_{11,\,7} = \sigma_{22}\sigma_{12}^2\omega_\alpha f^{(+1)}_{\mathrm{Hosford}}(\boldsymbol{\sigma}) + \sigma_{11}\sigma_{22}\sigma_{12}^2 e_{11}^{(+1)} \\ \Pi_{11,\,8} = \sigma_{22}^2\sigma_{12}^2 e_{11}^{(+1)} \\ \Pi_{11,\,9} = \sigma_{12}^4 e_{11}^{(+1)} \end{cases} \tag{C9f}$$

$$\begin{cases} \Pi_{22,1} = \sigma_{11}^4 e_{22}^{(+1)} \\ \Pi_{22,2} = \sigma_{11}^3\omega_\alpha f^{(+1)}_{\mathrm{Hosford}}(\boldsymbol{\sigma}) + \sigma_{11}^3\sigma_{22} e_{22}^{(+1)} \\ \Pi_{22,\,3} = 2\sigma_{11}^2\sigma_{22}\omega_\alpha f^{(+1)}_{\mathrm{Hosford}}(\boldsymbol{\sigma}) + \sigma_{11}^2\sigma_{22}^2 e_{22}^{(+1)} \\ \Pi_{22,\,4} = 3\sigma_{11}\sigma_{22}^2\omega_\alpha f^{(+1)}_{\mathrm{Hosford}}(\boldsymbol{\sigma}) + \sigma_{11}\sigma_{22}^3 e_{22}^{(+1)} \\ \Pi_{22,\,5} = 4\sigma_{22}^3\omega_\alpha f^{(+1)}_{\mathrm{Hosford}}(\boldsymbol{\sigma}) + \sigma_{22}^4 e_{22}^{(+1)} \\ \Pi_{22,\,6} = \sigma_{11}^2\sigma_{12}^2 e_{22}^{(+1)} \\ \Pi_{22,\,7} = \sigma_{11}\sigma_{12}^2\omega_\alpha f^{(+1)}_{\mathrm{Hosford}}(\boldsymbol{\sigma}) + \sigma_{11}\sigma_{22}\sigma_{12}^2 e_{22}^{(+1)} \\ \Pi_{22,\,8} = 2\sigma_{22}\sigma_{12}^2\omega_\alpha f^{(+1)}_{\mathrm{Hosford}}(\boldsymbol{\sigma}) + \sigma_{22}^2\sigma_{12}^2 e_{22}^{(+1)} \\ \Pi_{22,\,9} = \sigma_{12}^4 e_{22}^{(+1)} \end{cases} \tag{C9g}$$

$$\begin{cases} \Pi_{12,1} = \sigma_{11}^4 e_{12}^{(+1)} \\ \Pi_{12,2} = \sigma_{11}^3 \sigma_{22} e_{12}^{(+1)} \\ \Pi_{12,\ 3} = \sigma_{11}^2 \sigma_{22}^2 e_{12}^{(+1)} \\ \Pi_{12,\ 4} = \sigma_{11} \sigma_{22}^3 e_{12}^{(+1)} \\ \Pi_{12,\ 5} = \sigma_{22}^4 e_{12}^{(+1)} \\ \Pi_{12,\ 6} = 2\sigma_{11}^2 \sigma_{12} \omega_\alpha f_{\text{Hosford}}^{(+1)}(\boldsymbol{\sigma}) + \sigma_{11}^2 \sigma_{12}^2 e_{12}^{(+1)} \\ \Pi_{12,\ 7} = 2\sigma_{11} \sigma_{22} \omega_\alpha f_{\text{Hosford}}^{(+1)}(\boldsymbol{\sigma}) + \sigma_{11} \sigma_{22} \sigma_{12}^2 e_{12}^{(+1)} \\ \Pi_{12,\ 8} = 2\sigma_{22}^2 \sigma_{12} \omega_\alpha f_{\text{Hosford}}^{(+1)}(\boldsymbol{\sigma}) + \sigma_{22}^2 \sigma_{12}^2 e_{12}^{(+1)} \\ \Pi_{12,\ 9} = 4\sigma_{12}^3 \omega_\alpha f_{\text{Hosford}}^{(+1)}(\boldsymbol{\sigma}) + \sigma_{12}^4 e_{12}^{(+1)} \end{cases} \tag{C9h}$$

with

$$e_{ij}^{(+1)} = \left[\frac{\partial \omega}{\partial \sigma_{ij}} f_{\text{Hosford}}^{(+1)}(\boldsymbol{\sigma}) + \omega_\alpha \frac{\partial f_1^{(+1)}(\boldsymbol{\sigma})}{\partial \sigma_{ij}} \right] (i,j = 1,2) \tag{C9i}$$

$$\frac{\partial f_1^{(\pm 1)}(\boldsymbol{\sigma})}{\partial \sigma_{ij}} = 4^{\frac{k-2}{k}} \left(|X_1|^k + |X_2|^k + |X_1 - X_2|^k \right)^{\frac{4-k}{k}} \left(Y_{1,ij}^{(\pm 1)} + Y_{2,ij}^{(\pm 1)} + Y_{3,ij}^{(\pm 1)} \right) (i,j = 1,2; k = m,n) \tag{C9j}$$

$$\begin{cases} Y_{1,ij}^{(\pm 1)} = sign(X_1) |X_1|^{m,n-1} \dfrac{\partial X_1}{\partial \sigma_{ij}} (i,j = 1,2) \\ Y_{2,ij}^{(\pm 1)} = sign(X_2) |X_2|^{m,n-1} \dfrac{\partial X_2}{\partial \sigma_{ij}} (i,j = 1,2) \\ Y_{3,ij}^{(\pm 1)} = sign(X_1 - X_2) |X_1 - X_2|^{m,n-1} \left(\dfrac{\partial X_1}{\partial \sigma_{ij}} - \dfrac{\partial X_2}{\partial \sigma_{ij}} \right) (i,j = 1,2) \end{cases} \tag{C9k}$$

Different from Eqs. (9) and (17), σ_{ij} in Eqs. (C6) − (C9) is not related to the maximum principal stress and is defined as

$$\begin{cases} \sigma_{11} = \cos^2\alpha + p_\alpha(\bar{\varepsilon}^{\text{p}}) \sin^2\alpha \\ \sigma_{22} = \sin^2\alpha + p_\alpha(\bar{\varepsilon}^{\text{p}}) \cos^2\alpha \\ \sigma_{12} = [1 - p_\alpha(\bar{\varepsilon}^{\text{p}})] \sin\alpha\cos\alpha \end{cases} \tag{C10}$$

Combining Eqs. (C4) and (C9), the explicit function of the anisotropic coefficients is written as

$$\begin{bmatrix} A_3 \\ A_4 \\ A_5 \end{bmatrix} = \begin{bmatrix} \psi_3(r_{\text{T90}}) & \psi_4(r_{\text{T90}}) & \psi_5(r_{\text{T90}}) \\ \psi_3(\alpha_1, p_1) & \psi_4(\alpha_1, p_1) & \psi_5(\alpha_1, p_1) \\ \psi_3(\alpha_2, p_2) & \psi_4(\alpha_2, p_2) & \psi_5(\alpha_2, p_2) \end{bmatrix} \begin{bmatrix} \delta_r(r_{\text{T90}}) \\ \delta_r(\alpha_1, p_1) \\ \delta_r(\alpha_2, p_2) \end{bmatrix} \tag{C11}$$

Under UC stress state, combining Eqs. (3) and (22), there is

$$\psi_6(\alpha) A_{15} + \psi_7(\alpha) A_{16} + \psi_8(\alpha) A_{17} = \delta_r(\alpha) \tag{C12a}$$

with

$$\delta_r(\alpha) = -[\psi_1(\alpha) A_{10} + \psi_2(\alpha) A_{11} + \psi_3(\alpha) A_{12} + \psi_4(\alpha) A_{13} + \psi_5(\alpha) A_{14} + \psi_9(\alpha) A_{18}] \tag{C12b}$$

$$\psi_1(\alpha) = \sigma_{11}^3 \vartheta_1 \left[4 + \sigma_{11} \frac{\partial f_1^{(-1)}(\boldsymbol{\sigma})}{\partial \sigma_{11}} \right] + \vartheta_2 \sigma_{11}^4 \frac{\partial f_1^{(-1)}(\boldsymbol{\sigma})}{\partial \sigma_{22}} - \vartheta_3 \sigma_{11}^4 \frac{\partial f_1^{(-1)}(\boldsymbol{\sigma})}{\partial \sigma_{12}} \tag{C12c}$$

$$\psi_2(\alpha) = \sigma_{11}^2 \sigma_{22} \vartheta_1 \left[3 + \sigma_{11} \frac{\partial f_1^{(-1)}(\boldsymbol{\sigma})}{\partial \sigma_{11}} \right] + \sigma_{11}^3 \vartheta_2 \left[1 + \sigma_{22} \frac{\partial f_1^{(-1)}(\boldsymbol{\sigma})}{\partial \sigma_{22}} \right] - \vartheta_3 \sigma_{11}^3 \sigma_{22} \frac{\partial f_1^{(-1)}(\boldsymbol{\sigma})}{\partial \sigma_{12}} \tag{C12d}$$

$$\psi_3(\alpha) = \sigma_{11} \sigma_{22}^2 \vartheta_1 \left[2 + \sigma_{11} \frac{\partial f_1^{(-1)}(\boldsymbol{\sigma})}{\partial \sigma_{11}} \right] + \sigma_{11}^2 \sigma_{22} \vartheta_2 \left[2 + \sigma_{22} \frac{\partial f_1^{(-1)}(\boldsymbol{\sigma})}{\partial \sigma_{22}} \right] - \vartheta_3 \sigma_{11}^2 \sigma_{22}^2 \frac{\partial f_1^{(-1)}(\boldsymbol{\sigma})}{\partial \sigma_{12}} \tag{C12e}$$

$$\psi_4(\alpha) = \sigma_{22}^3 \vartheta_1 \left[1 + \sigma_{11} \frac{\partial f_1^{(-1)}(\boldsymbol{\sigma})}{\partial \sigma_{11}} \right] + \sigma_{11} \sigma_{22}^2 \vartheta_2 \left[3 + \sigma_{22} \frac{\partial f_1^{(-1)}(\boldsymbol{\sigma})}{\partial \sigma_{22}} \right] - \vartheta_3 \sigma_{11} \sigma_{22}^3 \frac{\partial f_1^{(-1)}(\boldsymbol{\sigma})}{\partial \sigma_{12}} \tag{C12f}$$

$$\psi_5(\alpha) = \vartheta_1 \sigma_{22}^4 \frac{\partial f_1^{(-1)}(\boldsymbol{\sigma})}{\partial \sigma_{11}} + \sigma_{22}^3 \vartheta_2 \left[4 + \sigma_{22} \frac{\partial f_1^{(-1)}(\boldsymbol{\sigma})}{\partial \sigma_{22}} \right] - \vartheta_3 \sigma_{22}^4 \frac{\partial f_1^{(-1)}(\boldsymbol{\sigma})}{\partial \sigma_{12}} \tag{C12g}$$

$$\psi_6(\alpha) = \sigma_{11} \sigma_{12}^2 \vartheta_1 \left[2 + \sigma_{11} \frac{\partial f_1^{(-1)}(\boldsymbol{\sigma})}{\partial \sigma_{11}} \right] + \vartheta_2 \sigma_{11}^2 \sigma_{12}^2 \frac{\partial f_1^{(-1)}(\boldsymbol{\sigma})}{\partial \sigma_{22}} - \sigma_{11}^2 \sigma_{12} \vartheta_3 \left[2 + \sigma_{12} \frac{\partial f_1^{(-1)}(\boldsymbol{\sigma})}{\partial \sigma_{12}} \right] \tag{C12h}$$

$$\psi_7(\alpha)=\sigma_{22}\sigma_{12}^2\vartheta_1\left[1+\sigma_{11}\frac{\partial f_1^{(-1)}(\boldsymbol{\sigma})}{\partial\sigma_{11}}\right]+\sigma_{11}\sigma_{12}^2\vartheta_2\left[1+\sigma_{22}\frac{\partial f_1^{(-1)}(\boldsymbol{\sigma})}{\partial\sigma_{22}}\right]-\vartheta_3\sigma_{11}\sigma_{22}\sigma_{12}\left[2+\sigma_{12}\frac{\partial f_1^{(-1)}(\boldsymbol{\sigma})}{\partial\sigma_{12}}\right] \tag{C12i}$$

$$\psi_8(\alpha)=\vartheta_1\sigma_{22}^2\sigma_{12}^2\frac{\partial f_1^{(-1)}(\boldsymbol{\sigma})}{\partial\sigma_{11}}+\sigma_{22}\sigma_{12}^2\vartheta_2\left[2+\sigma_{22}\frac{\partial f_1^{(-1)}(\boldsymbol{\sigma})}{\partial\sigma_{22}}\right]-\sigma_{22}^2\sigma_{12}\vartheta_3\left[2+\sigma_{12}\frac{\partial f_1^{(-1)}(\boldsymbol{\sigma})}{\partial\sigma_{12}}\right] \tag{C12j}$$

$$\psi_9=\vartheta_1\sigma_{12}^4\frac{\partial f_1^{(-1)}(\boldsymbol{\sigma})}{\partial\sigma_{11}}+\vartheta_2\sigma_{12}^4\frac{\partial f_1^{(-1)}(\boldsymbol{\sigma})}{\partial\sigma_{22}}-\sigma_{12}^3\vartheta_3\left[4+\sigma_{12}\frac{\partial f_1^{(-1)}(\boldsymbol{\sigma})}{\partial\sigma_{12}}\right] \tag{C12k}$$

$$\vartheta_1=r_{\mathrm{C}\alpha}(\overline{\varepsilon}^{\mathrm{p}})+\sin^2\alpha;\vartheta_2=r_{\mathrm{C}\alpha}(\overline{\varepsilon}^{\mathrm{p}})+\cos^2\alpha;\vartheta_3=\sin\alpha\cos\alpha \tag{C12l}$$

$$\sigma_{11}=-\cos^2\alpha;\sigma_{22}=-\sin^2\alpha;\sigma_{12}=-\sin\alpha\cos\alpha \tag{C12m}$$

Through Eq. (C12), we obtain

$$\begin{bmatrix}A_{15}\\A_{16}\\A_{17}\end{bmatrix}=\begin{bmatrix}\psi_3(\alpha_1)&\psi_4(\alpha_1)&\psi_5(\alpha_1)\\\psi_3(\alpha_2)&\psi_4(\alpha_2)&\psi_5(\alpha_2)\\\psi_3(\alpha_3)&\psi_4(\alpha_3)&\psi_5(\alpha_3)\end{bmatrix}\begin{bmatrix}\delta_r(\alpha_1)\\\delta_r(\alpha_2)\\\delta_r(\alpha_3)\end{bmatrix} \tag{C13}$$

where $\{\alpha_1,\alpha_2,\alpha_3\}=\{30,45,60\}$. Under UT stress state, we have

$$\psi_6(\alpha)A_6+\psi_7(\alpha)A_7+\psi_8(\alpha)A_8+\psi_9(\alpha)A_9=\delta_r(\alpha) \tag{C14a}$$

with

$$\delta_r(\alpha)=-[\psi_1(\alpha)A_1+\psi_2(\alpha)A_2+\psi_3(\alpha)A_3+\psi_4(\alpha)A_4+\psi_5(\alpha)A_5] \tag{C14b}$$

$$\psi_1(\alpha)=\sigma_{11}^3\vartheta_1\left[4+\sigma_{11}\frac{\partial f_1^{(+1)}(\boldsymbol{\sigma})}{\partial\sigma_{11}}\right]+\vartheta_2\sigma_{11}^4\frac{\partial f_1^{(+1)}(\boldsymbol{\sigma})}{\partial\sigma_{22}}-\vartheta_3\sigma_{11}^4\frac{\partial f_1^{(+1)}(\boldsymbol{\sigma})}{\partial\sigma_{12}} \tag{C14c}$$

$$\psi_2(\alpha)=\sigma_{11}^2\sigma_{22}\vartheta_1\left[3+\sigma_{11}\frac{\partial f_1^{(+1)}(\boldsymbol{\sigma})}{\partial\sigma_{11}}\right]+\sigma_{11}^3\vartheta_2\left[1+\sigma_{22}\frac{\partial f_1^{(+1)}(\boldsymbol{\sigma})}{\partial\sigma_{22}}\right]-\vartheta_3\sigma_{11}^3\sigma_{22}\frac{\partial f_1^{(+1)}(\boldsymbol{\sigma})}{\partial\sigma_{12}} \tag{C14d}$$

$$\psi_3(\alpha)=\sigma_{11}\sigma_{22}^2\vartheta_1\left[2+\sigma_{11}\frac{\partial f_1^{(+1)}(\boldsymbol{\sigma})}{\partial\sigma_{11}}\right]+\sigma_{11}^2\sigma_{22}\vartheta_2\left[2+\sigma_{22}\frac{\partial f_1^{(+1)}(\boldsymbol{\sigma})}{\partial\sigma_{22}}\right]-\vartheta_3\sigma_{11}^2\sigma_{22}^2\frac{\partial f_1^{(+1)}(\boldsymbol{\sigma})}{\partial\sigma_{12}} \tag{C14e}$$

$$\psi_4(\alpha)=\sigma_{22}^3\vartheta_1\left[1+\sigma_{11}\frac{\partial f_1^{(+1)}(\boldsymbol{\sigma})}{\partial\sigma_{11}}\right]+\sigma_{11}\sigma_{22}^2\vartheta_2\left[3+\sigma_{22}\frac{\partial f_1^{(+1)}(\boldsymbol{\sigma})}{\partial\sigma_{22}}\right]-\vartheta_3\sigma_{11}\sigma_{22}^3\frac{\partial f_1^{(+1)}(\boldsymbol{\sigma})}{\partial\sigma_{12}} \tag{C14f}$$

$$\psi_5(\alpha)=\vartheta_1\sigma_{22}^4\frac{\partial f_1^{(+1)}(\boldsymbol{\sigma})}{\partial\sigma_{11}}+\sigma_{22}^3\vartheta_2\left[4+\sigma_{22}\frac{\partial f_1^{(+1)}(\boldsymbol{\sigma})}{\partial\sigma_{22}}\right]-\vartheta_3\sigma_{22}^4\frac{\partial f_1^{(+1)}(\boldsymbol{\sigma})}{\partial\sigma_{12}} \tag{C14g}$$

$$\psi_6(\alpha)=\sigma_{11}\sigma_{12}^2\vartheta_1\left[2+\sigma_{11}\frac{\partial f_1^{(+1)}(\boldsymbol{\sigma})}{\partial\sigma_{11}}\right]+\vartheta_2\sigma_{11}^2\sigma_{12}^2\frac{\partial f_1^{(+1)}(\boldsymbol{\sigma})}{\partial\sigma_{22}}-\sigma_{11}^2\sigma_{12}\vartheta_3\left[2+\sigma_{12}\frac{\partial f_1^{(+1)}(\boldsymbol{\sigma})}{\partial\sigma_{12}}\right] \tag{C14h}$$

$$\psi_7(\alpha)=\sigma_{22}\sigma_{12}^2\vartheta_1\left[1+\sigma_{11}\frac{\partial f_1^{(+1)}(\boldsymbol{\sigma})}{\partial\sigma_{11}}\right]+\sigma_{11}\sigma_{12}^2\vartheta_2\left[1+\sigma_{22}\frac{\partial f_1^{(+1)}(\boldsymbol{\sigma})}{\partial\sigma_{22}}\right]-\vartheta_3\sigma_{11}\sigma_{22}\sigma_{12}\left[2+\sigma_{12}\frac{\partial f_1^{(+1)}(\boldsymbol{\sigma})}{\partial\sigma_{12}}\right] \tag{C14i}$$

$$\psi_8(\alpha)=\vartheta_1\sigma_{22}^2\sigma_{12}^2\frac{\partial f_1^{(+1)}(\boldsymbol{\sigma})}{\partial\sigma_{11}}+\sigma_{22}\sigma_{12}^2\vartheta_2\left[2+\sigma_{22}\frac{\partial f_1^{(+1)}(\boldsymbol{\sigma})}{\partial\sigma_{22}}\right]-\sigma_{22}^2\sigma_{12}\vartheta_3\left[2+\sigma_{12}\frac{\partial f_1^{(+1)}(\boldsymbol{\sigma})}{\partial\sigma_{12}}\right] \tag{C14j}$$

$$\psi_9(\alpha)=\vartheta_1\sigma_{12}^4\frac{\partial f_1^{(+1)}(\boldsymbol{\sigma})}{\partial\sigma_{11}}+\vartheta_2\sigma_{12}^4\frac{\partial f_1^{(+1)}(\boldsymbol{\sigma})}{\partial\sigma_{22}}-\sigma_{12}^3\vartheta_3\left[4+\sigma_{12}\frac{\partial f_1^{(+1)}(\boldsymbol{\sigma})}{\partial\sigma_{12}}\right] \tag{C14k}$$

$$\vartheta_1=r_{\mathrm{T}\alpha}(\overline{\varepsilon}^{\mathrm{p}})+\sin^2\alpha;\vartheta_2=r_{\mathrm{T}\alpha}(\overline{\varepsilon}^{\mathrm{p}})+\cos^2\alpha;\vartheta_3=\sin\alpha\cos\alpha \tag{C14l}$$

$$\sigma_{11}=\cos^2\alpha;\sigma_{22}=\sin^2\alpha;\sigma_{12}=\sin\alpha\cos\alpha \tag{C14m}$$

Combining Eqs. (C12) and (C14), there is

$$\begin{bmatrix} A_6 \\ A_7 \\ A_8 \\ A_9 \end{bmatrix} = \begin{bmatrix} \psi_6(\alpha_1) & \psi_7(\alpha_1) & \psi_8(\alpha_1) & \psi_9(\alpha_1) \\ \psi_6(\alpha_2) & \psi_7(\alpha_2) & \psi_8(\alpha_2) & \psi_9(\alpha_2) \\ \psi_6(\alpha_3) & \psi_7(\alpha_3) & \psi_8(\alpha_3) & \psi_9(\alpha_3) \\ \psi_6(\alpha_4,p_4) & \psi_7(\alpha_4,p_4) & \psi_8(\alpha_4,p_4) & \psi_9(\alpha_4,p_4) \end{bmatrix} \begin{bmatrix} \delta_r(\alpha_1) \\ \delta_r(\alpha_2) \\ \delta_r(\alpha_3) \\ \delta_r(\alpha_4,p_4) \end{bmatrix} \tag{C15}$$

The convexity control coefficients of the PPF of the new asymmetric model will be solved based on the method mentioned in Section 4.1. In addition, the convexity of the yield surface described by the PPF of the new asymmetric model for DP490 and AA6016-T4 is proved by the new convexity proof method.

Appendix D. Calibration results of anisotropic coefficients for various yield criteria

Table D1
Anisotropic coefficients of NAFR-Poly4 for DP490 and AA6016-T4.

		α_1^y	α_2^y	α_3^y	α_4^y	α_5^y	α_6^y	α_7^y	α_8^y	α_9^y
YSF	DP490	1.0000	−1.2043	1.6434	−1.6552	1.0821	4.9764	−3.5182	5.1294	12.0147
	AA6016	1.0000	−0.8802	1.1880	−1.4401	1.3675	6.0670	1.4675	6.9744	5.0336
		α_1^p	α_2^p	α_3^p	α_4^p	α_5^p	α_6^p	α_7^p	α_8^p	α_9^p
PPF	DP490	1.0000	−1.2256	2.5152	−1.6094	0.9677	5.6119	−11.6879	13.9162	8.7671
	AA6016	1.0000	−1.3997	2.2228	−1.3490	1.1101	4.6803	−0.5447	6.2353	3.6105

Table D2
Anisotropic coefficients of AFR-Poly6 for DP490 and AA6016-T4.

	a_1	a_2	a_3	a_4	a_5	a_6	a_7	a_8
DP490	1.0000	−1.7741	3.0291	−4.3262	4.6836	−2.9322	1.1256	10.1416
AA6016	1.0000	−2.0994	4.8000	−5.6911	4.6791	−2.9149	1.5991	11.4377
	a_9	a_{10}	a_{11}	a_{12}	a_{13}	a_{14}	a_{15}	a_{16}
DP490	−19.9565	23.4335	−4.3043	0.4847	33.3446	−27.3739	50.6119	18.7113
AA6016	−7.8522	20.3341	−0.5374	9.4078	21.1025	1.2191	31.5518	6.6730

Table D3
Anisotropic coefficients of EYld2000-2d for DP490 and AA6016-T4.

	c_{11}	c_{12}	c_{21}	c_{22}	c_{66}	c'_{11}	c'_{12}	c'_{21}	c'_{22}	c'_{66}	n
DP490	0.0393	1.1365	0.8809	−0.0945	1.0531	0.8836	0.3647	0.3647	0.1515	1.4182	6
AA6016	0.0128	1.0867	0.9831	−0.0745	0.6869	1.0872.	0.0323	−0.0323	1.1566	1.4341	8

Table D4
Anisotropic coefficients of the new symmetric model for DP490 and AA6016-T4.

		κ_1	κ_2	κ_3	κ_4	κ_5	κ_6	κ_7	κ_8	κ_9	κ_{10}	κ_{11}
YSF	DP490	1.0000	−2.5676	6.3000	−8.8362	7.2126	−3.4286	1.1256	5.1635	−2.4993	5.3245	10.6135
	AA6016	1.0000	−2.4848	7.0000	−10.0196	8.0454	−3.7674	1.5991	6.3356	1.0156	7.2307	4.9605
		κ_1	κ_2	κ_3	κ_4	κ_5	κ_6	κ_7	κ_8	κ_9	κ_{10}	κ_{11}
PPF	DP490	1.0000	−1.7741	3.4177	−4.5896	4.9388	−2.7613	1.0600	3.0294	−11.6199	16.8367	7.9743
	AA6016	1.0000	−2.0994	4.4962	−5.8610	5.1006	−2.5319	1.3890	5.1210	−0.6112	7.1850	3.4477

Table D5
Anisotropic coefficients of CFI2023 for DP490 and AA6016-T4.

		h_{y1}	h_{y2}	a_y	b_y	c_y	d_y	e_y	ρ_y
YSF	DP490	0.03456	0.1905	0.8688	1.4361	1.3976	0.9210	1.1413	3.6
	AA6016	0.0241	0.0477	0.9072	0.4826	0.3065	1.3093	1.3177	4.1
		h_{p1}	h_{p2}	a_p	b_p	c_p	d_p	ϖ_p	e_p	ρ_p
PPF	DP490	−0.1403	0.3293	1.6910	1.2874	1.3887	0.7462	0.3501	0.8114	3.6000
	AA6016	−0.1777	−0.1512	1.9235	−1.5506	1.4575	1.2529	2.2294	0.2421	4.1100

Table D6
Anisotropic coefficients of LAA2023 for DP490 and AA6016-T4.

		$F_y^{(+1)}$	$G_y^{(+1)}$	$H_y^{(+1)}$	$N_y^{(+1)}$	$F_y^{(-1)}$	$G_y^{(-1)}$	$H_y^{(-1)}$	$N_y^{(+1)}$
YSF	DP490	0.9418	0.8613	1.1387	3.5107	0.8488	1.0783	0.9217	2.7445
	AA6016	1.2431	0.9043	1.0957	3.4846	1.2844	0.9929	1.0071	2.2695
		$F_p^{(+1)}$	$G_p^{(+1)}$	$H_p^{(+1)}$	$N_p^{(+1)}$	$F_p^{(-1)}$	$G_p^{(-1)}$	$H_p^{(-1)}$	$N_p^{(+1)}$
PPF	DP490	0.9418	0.8613	1.1387	3.5107	0.8488	1.0783	0.9217	2.7445
	AA6016	1.6037	1.3002	0.6998	1.8865	1.8418	1.4961	0.5039	2.1484

Table D7
Anisotropic coefficients of ZHC2023 for DP490 and AA6016-T4.

		a_{y0}	a_{y45}	a_{y90}	a_{yEB}	T_{y0}	T_{y45}	T_{y90}	T_{yEB}	k_y
YSF	DP490	0.0174	0.1040	0.0977	0.0158	393.8298	374.9794	386.1390	408.2590	2.1
	AA6016	0.0121	0.1562	0.0223	0.0896	132.1941	165.5808	189.3217	109.7079	−0.4
		a_{p0}	a_{p45}		a_{p90}	a_{pEB}	T_{p0}	T_{p45}	T_{p90}	T_{pEB}
PPF	DP490	0.2798	−0.2800		−0.2393	0.1293	393.8298	552.2273	574.4507	399.2778
	AA6016	0.0308	−0.3157		−0.6145	−0.1190	132.1941	165.5808	189.3217	109.7079

Table D8
Anisotropic coefficients of the new asymmetric model for DP490 and AA6016-T4.

		A_1	A_2	A_3	A_4	A_5	A_6	A_7	A_8	A_9	A_{10}	A_{11}
YSF	DP490	1.0000	−3.1672	8.5187	−11.4528	8.5187	−3.6974	1.1256	5.3507	−3.4609	5.4625	11.2216
	AA6016	1.0000	−2.72756	7.3463	−9.5827	7.3463	−3.6086	1.5986	6.4775	−3.0466	7.2968	8.8090
		A_1	A_2	A_3	A_4	A_5	A_6	A_7	A_8	A_9	m	
PPF	DP490	1.0000	−0.3655	2.8010	−2.2950	1.5577	7.1988	–23.6240	29.7533	9.9795	5.0000	
	AA6016	1.0000	−0.7993	6.5105	−0.6025	1.3997	5.0688	−3.5001	6.6455	3.0171	2.8000	
		A_{10}	A_{11}	A_{12}	A_{13}	A_{14}	A_{15}	A_{16}	A_{17}	A_{18}	n	
	DP490	1.0000	−1.4413	4.0000	−1.2039	0.8100	6.8617	−4.8922	6.6532	9.0000	3.0000	
	AA6016	1.0000	−0.0156	0.4000	0.3940	1.4000	1.8241	2.1544	2.1040	0.7000	2.8000	

Appendix E. The hardening curves of DP490 and AA6016-T4

The hardening curves of DP490 and AA6016-T4 are as follows:

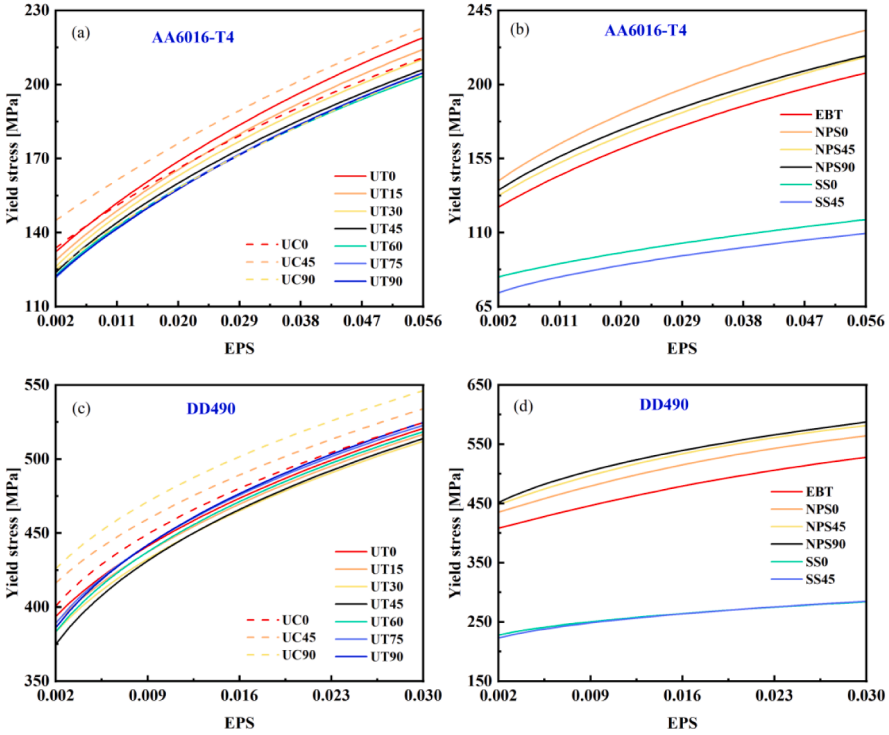

Fig. E1. The hardening curves of DP490 and AA6016-T4.

Data availability

Data will be made available on request.

References

[1] H.R. Dong, X.Q. Li, Y. Li, S.T. Zhao, H.B. Wang, X.C. Liu, B. Meng, K. Du, The anomalous negative electric current sensitivity of a precipitation hardened Al alloy during electrically-assisted forming, J. Mater. Res. Technol. 24 (2023) 9356–9368, https://doi.org/10.1016/j.jmrt.2023.05.161.

[2] Y. Hou, J. Min, M.-G. Lee, Non-associated and non-quadratic characteristics in plastic anisotropy of automotive lightweight sheet metals, Automot, Innovation 6 (2023) 364–378, https://doi.org/10.1007/s42154-023-00232-5.

[3] W. Zhang, J. Xu, Advanced lightweight materials for automobiles: a review, Mater. Des. 221 (2022) 110994, https://doi.org/10.1016/j.matdes.2022.110994.

[4] Y.S. Lou, J.W. Yoon, Lode-dependent anisotropic-asymmetric yield function for isotropic and anisotropic hardening of pressure-insensitive materials. Part I: quadratic function under non-associated flow rule, Int. J. Plast 166 (2023) 103647, https://doi.org/10.1016/j.ijplas.2023.103647.

[5] J.W. Yoon, Y.S. Lou, J. Yoon, M.V. Glazoff, Asymmetric yield function based on the stress invariants for pressure sensitive metals, Int. J. Plast 56 (2014) 184–202, https://doi.org/10.1016/j.ijplas.2013.11.008.

[6] L.H. Zheng, J.W. Yoon, A flexible yield criterion for strength modeling from biaxial compression to biaxial tension, Int. J. Plast 182 (2024) 104113, https://doi.org/10.1016/j.ijplas.2024.104113.

[7] C. Zhang, Y.S. Lou, Influences of the evolving plastic behavior of sheet metal on V-bending and springback analysis considering different stress states, Int. J. Plast 173 (2024) 103889, https://doi.org/10.1016/j.ijplas.2024.103889.

[8] T. Kuwabara, Biaxial stress testing methods for sheet metals, in: Comprehensive Materials Processing, Elsevier, 2014: pp. 95–111. https://doi.org/10.1016/B978-0-08-096532-1.00106-0.

[9] A. Brosius, N. Küsters, M. Lenzen, New method for stress determination based on digital image correlation data, CIRP Ann. 67 (2018) 269–272, https://doi.org/10.1016/j.cirp.2018.04.026.

[10] M. Gotoh, A theory of plastic anisotropy based on a yield function of fourth order (plane stress state)—I, Int. J. Mech. Sci. 19 (1977) 505–512, https://doi.org/10.1016/0020-7403(77)90043-1.

[11] D. Banabic, O. Cazacu, F. Barlat, D.S. Comsa, S. Wagner, K. Siegert, Description of anisotropic behaviour of AA3103-0 aluminium alloy using two recent yield criteria, J. Phys. IV Proc. 105 (2003) 297–304, https://doi.org/10.1051/jp4:20030200.

[12] D. Banabic, An improved analytical description of orthotropy in metallic sheets, Int. J. Plast 21 (2005) 493–512, https://doi.org/10.1016/j.ijplas.2004.04.003.

[13] F. Barlat, J.C. Brem, J.W. Yoon, K. Chung, R.E. Dick, D.J. Lege, F. Pourboghrat, S.-H. Choi, E. Chu, Plane stress yield function for aluminum alloy sheets—part 1: theory, Int. J. Plast 19 (2003) 1297–1319, https://doi.org/10.1016/S0749-6419(02)00019-0.

[14] F. Barlat, H. Aretz, J.W. Yoon, M.E. Karabin, J.C. Brem, R.E. Dick, Linear transfomation-based anisotropic yield functions, Int. J. Plast 21 (2005) 1009–1039, https://doi.org/10.1016/j.ijplas.2004.06.004.

[15] H. Aretz, F. Barlat, New convex yield functions for orthotropic metal plasticity, Int. J. Non-Linear Mech. 51 (2013) 97–111, https://doi.org/10.1016/j.ijnonlinmec.2012.12.007.

[16] O.A.N. Cazacu, F. Barlat, Application of the theory of representation to describe yielding of anisotropic aluminum alloys, Int. J. Eng. Sci. 41 (2003) 1367–1385, https://doi.org/10.1016/S0020-7225(03)00037-5.

[17] O.A.N. Cazacu, New yield criteria for isotropic and textured metallic materials, Int. J. Solids Struct. 139–140 (2018) 200–210, https://doi.org/10.1016/j.ijsolstr.2018.01.036.

[18] Y.S. Lou, C. Zhang, S.J. Zhang, J.W. Yoon, A general yield function with differential and anisotropic hardening for strength modelling under various stress states with non-associated flow rule, Int. J. Plast 158 (2022) 103414, https://doi.org/10.1016/j.ijplas.2022.103414.

[19] H. Vegter, A.H. Van Den Boogaard, A plane stress yield function for anisotropic sheet material by interpolation of biaxial stress states, Int. J. Plast 22 (2006) 557–580, https://doi.org/10.1016/j.ijplas.2005.04.009.

[20] F. Peng, X.H. Dong, X.Y. Tian, H.Y. Xie, K. Liu, An interpolation-type orthotropic yield function and its application under biaxial tension, Int. J. Mech. Sci. 99 (2015) 89–97, https://doi.org/10.1016/j.ijmecsci.2015.05.008.

[21] E.-H. Lee, T.B. Stoughton, J.W. Yoon, A yield criterion through coupling of quadratic and non-quadratic functions for anisotropic hardening with non-associated flow rule, Int. J. Plast 99 (2017) 120–143, https://doi.org/10.1016/j.ijplas.2017.08.007.

[22] Q. Hu, J.W. Yoon, N. Manopulo, P. Hora, A coupled yield criterion for anisotropic hardening with analytical description under associated flow rule: modeling and validation, Int. J. Plast 136 (2021) 102882, https://doi.org/10.1016/j.ijplas.2020.102882.

[23] T. Kuwabara, Anisotropic plastic deformation of extruded aluminum alloy tube under axial forces and internal pressure, Int. J. Plast 21 (2005) 101–117, https://doi.org/10.1016/j.ijplas.2004.04.006.

[24] K. Han, X.Q. Li, X.Y. Peng, H.B. Wang, D.S. Li, Y.L. Li, Q. Li, Experimental and numerical study on the deformation mechanism of straight flanging by incremental sheet forming, Int. J. Mech. Sci. 160 (2019) 75–89, https://doi.org/10.1016/j.ijmecsci.2019.06.024.
[25] Y. Yan, H.B. Wang, Q. Li, The inverse parameter identification of hill 48 yield criterion and its verification in press bending and roll forming process simulations, J. Manuf. Processes 20 (2015) 46–53, https://doi.org/10.1016/j.jmapro.2015.09.009.
[26] Z.H. Du, Z.Q. Yan, X.H. Cui, B.G. Chen, H.L. Yu, D.Y. Qiu, W.Z. Xia, Z.S. Deng, Springback control and large skin manufacturing by high-speed vibration using electromagnetic forming, J. Mater. Process. Technol. 299 (2022) 117340, https://doi.org/10.1016/j.jmatprotec.2021.117340.
[27] J.J. Ha, Y.P. Korkolis, Hole-expansion: sensitivity of failure prediction on plastic anisotropy modeling, J. Manuf. Mater. Process. 5 (2021) 28, https://doi.org/10.3390/jmmp5020028.
[28] M. Gorji, B. Berisha, P. Hora, F. Barlat, Modeling of localization and fracture phenomena in strain and stress space for sheet metal forming, Int. J. Mater. Form. 9 (2016) 573–584, https://doi.org/10.1007/s12289-015-1242-y.
[29] F.H. Shen, Y. Sparrer, J. Rao, M. Könemann, S. Münstermann, J.H. Lian, A forming limit framework accounting for various failure mechanisms: localization, ductile and cleavage fracture, Int. J. Plast 175 (2024) 103921, https://doi.org/10.1016/j.ijplas.2024.103921.
[30] C. Butcher, F. Khameneh, A. Abedini, D. Connolly, S. Kurukuri, On the experimental characterization of sheet metal formability and the consistent calibration of the MK model for biaxial stretching in plane stress, J. Mater. Process. Technol. 287 (2021) 116887, https://doi.org/10.1016/j.jmatprotec.2020.116887.
[31] Y. Hou, J.Y. Min, A.A. El-Aty, H.N. Han, M.-G. Lee, A new anisotropic-asymmetric yield criterion covering wider stress states in sheet metal forming, Int. J. Plast 166 (2023) 103653, https://doi.org/10.1016/j.ijplas.2023.103653.
[32] H.B. Tian, B. Brownell, M. Baral, Y.P. Korkolis, Earing in cup-drawing of anisotropic al-6022-T4 sheets, Int. J. Mater. Form. 10 (2017) 329–343, https://doi.org/10.1007/s12289-016-1282-y.
[33] M.-S. Aydın, J. Gerlach, L. Kessler, A.E. Tekkaya, Yield locus evolution and constitutive parameter identification using plane strain tension and tensile tests, J. Mater. Process. Technol. 211 (2011) 1957–1964, https://doi.org/10.1016/j.jmatprotec.2011.06.018.
[34] K. Du, S.H. Huang, H.B. Wang, F.X. Yu, L. Pan, H.J. Huang, W.T. Zheng, X.G. Yuan, Effect of different yield criteria and material parameter identification methods on the description accuracy of the anisotropic behavior of 5182-O aluminum alloy, J. Mater. Eng. Perform. 31 (2022) 1077–1095, https://doi.org/10.1007/s11665-021-06295-x.
[35] Z.K. Mu, W. Wang, S.J. Zhang, Z.H. Zheng, H.J. Yan, S.S. Liu, S.B. Ma, K. Du, Y. Hou, Towards improved description of plastic anisotropy in sheet metals under biaxial loading: a novel generalization of Hill48 yield criterion, Mater. Today Commun. 41 (2024) 110222, https://doi.org/10.1016/j.mtcomm.2024.110222.
[36] J. Min, J. Kong, Y. Hou, Z. Liu, J. Lin, Application of laser deposition to mechanical characterization of advanced high strength steels subject to non-proportional loading, Exp. Mech. 62 (2022) 685–700, https://doi.org/10.1007/s11340-022-00820-2.
[37] T. Kuwabara, F. Sugawara, Multiaxial tube expansion test method for measurement of sheet metal deformation behavior under biaxial tension for a large strain range, Int. J. Plast 45 (2013) 103–118, https://doi.org/10.1016/j.ijplas.2012.12.003.
[38] M. Lenzen, M. Merklein, Improvement of numerical modelling considering plane strain material characterization with an elliptic hydraulic bulge test, JMMP 2 (2018) 6, https://doi.org/10.3390/jmmp2010006.
[39] C. Butcher, A. Abedini, On anisotropic plasticity models using linear transformations on the deviatoric stress: physical constraints on plastic flow in generalized plane strain, Int. J. Mech. Sci. 161–162 (2019) 105044, https://doi.org/10.1016/j.ijmecsci.2019.105044.
[40] J.-Y. Lee, K.-J. Lee, M.-G. Lee, T. Kuwabara, F. Barlat, Numerical modeling for accurate prediction of strain localization in hole expansion of a steel sheet, Int. J. Solids Struct. 156–157 (2019) 107–118, https://doi.org/10.1016/j.ijsolstr.2018.08.005.
[41] K. Du, S.H. Huang, M.H. Shi, L.J. Li, H.J. Huang, S.J. Zhang, W.T. Zheng, X. G. Yuan, Effects of biaxial tensile mechanical properties and non-integer exponent on description accuracy of anisotropic yield behavior, Mater. Des. 212 (2021) 110210, https://doi.org/10.1016/j.matdes.2021.110210.
[42] Q. Hu, J.W. Yoon, T.B. Stoughton, Analytical determination of anisotropic parameters for Poly6 yield function, Int. J. Mech. Sci. 201 (2021) 106467, https://doi.org/10.1016/j.ijmecsci.2021.106467.
[43] Y. Hou, K. Du, A.A. El-Aty, M.-G. Lee, J.Y. Min, Plastic anisotropy of sheet metals under plane strain loading: a novel non-associated constitutive model based on fourth-order polynomial functions, Mater. Des. 223 (2022) 111187, https://doi.org/10.1016/j.matdes.2022.111187.
[44] Z. Chen, User-friendly anisotropic hardening function with non-associated flow rule under the proportional loadings for BCC and FCC metals, Mech, Mater, 2022.
[45] K. Du, L. Dong, H. Zhang, Z.K. Mu, H.R. Dong, H.B. Wang, Y.Q. Ren, L. Sun, L. Zhang, X.G. Yuan, Modeling of Eyld2000-2d anisotropic yield criterion considering strength differential effect and analysis of optimal calibration strategy, Materials 16 (2023) 6445, https://doi.org/10.3390/ma16196445.
[46] T. Hakoyama, C.S. Hakoyama, T. Kuwabara, Experimental validation of non-associated flow rule and hydraulic bulge forming simulation for a 6000 series aluminum alloy sheet, Int. J. Solids Struct. 311 (2025) 113218, https://doi.org/10.1016/j.ijsolstr.2025.113218.
[47] Q. Hu, J.W. Yoon, J. Chen, Analytically described polynomial yield criterion by considering both plane strain and pure shear states, Int. J. Plast 162 (2023) 103514, https://doi.org/10.1016/j.ijplas.2022.103514.
[48] H.C. Shang, C. Zhang, S.C. Wang, Y.S. Lou, Large strain flow curve characterization considering strain rate and thermal effect for 5182-O aluminum alloy, Int. J. Mater. Form. 16 (2023) 1, https://doi.org/10.1007/s12289-022-01721-4.
[49] G.F. Han, J. He, S.H. Li, Z.Q. Lin, Simple shear methodology for local structure–property relationships of sheet metals: State-of-the-art and open issues, Prog. Mater Sci. 143 (2024) 101266, https://doi.org/10.1016/j.pmatsci.2024.101266.
[50] M. Panchal, L. Kaushik, R. KR, R. Khatirkar, S.-H. Choi, J. Singh, Recent advances in the in-plane shear testing of Mg alloy sheets, J. Magnesium Alloys 11 (2023) 405–424. https://doi.org/10.1016/j.jma.2023.02.006.
[51] Q. Yin, B. Zillmann, S. Suttner, G. Gerstein, M. Biasutti, A.E. Tekkaya, M.-F.-X. Wagner, M. Merklein, M. Schaper, T. Halle, A. Brosius, An experimental and numerical investigation of different shear test configurations for sheet metal characterization, Int. J. Solids Struct. 51 (2014) 1066–1074, https://doi.org/10.1016/j.ijsolstr.2013.12.006.
[52] H. Traphöner, T. Clausmeyer, A.E. Tekkaya, Material characterization for plane and curved sheets using the in-plane torsion test – an overview, J. Mater. Process. Technol. 257 (2018) 278–287, https://doi.org/10.1016/j.jmatprotec.2018.02.030.
[53] A. Brosius, Q. Yin, A. Güner, A.E. Tekkaya, A new shear test for sheet metal characterization, Steel Res. Int. 82 (2011) 323–328, https://doi.org/10.1002/srin.201000163.
[54] A. Abedini, C. Butcher, T. Rahmaan, M.J. Worswick, Evaluation and calibration of anisotropic yield criteria in shear loading: Constraints to eliminate numerical artefacts, Int. J. Solids Struct. 151 (2018) 118–134, https://doi.org/10.1016/j.ijsolstr.2017.06.029.
[55] Y. Hou, J.Y. Min, J.P. Lin, M.-G. Lee, Modeling stress anisotropy, strength differential, and anisotropic hardening by coupling quadratic and stress-invariant-based yield functions under non-associated flow rule, Mech. Mater. 174 (2022) 104458, https://doi.org/10.1016/j.mechmat.2022.104458.
[56] Y.S. Lou, S.J. Zhang, J.W. Yoon, Strength modeling of sheet metals from shear to plane strain tension, Int. J. Plast 134 (2020) 102813, https://doi.org/10.1016/j.ijplas.2020.102813.
[57] Z.B. He, K. Zhang, H.H. Zhu, Y.L. Lin, M.W. Fu, S.J. Yuan, An anisotropic constitutive model for forming of aluminum tubes under both biaxial tension and pure shear stress states, Int. J. Plast 152 (2022) 103259, https://doi.org/10.1016/j.ijplas.2022.103259.
[58] K. Du, S.H. Huang, X.Q. Li, H.B. Wang, W.T. Zheng, X.G. Yuan, Evolution of yield behavior for AA6016-T4 and DP490—towards a systematic evaluation strategy for material models, Int. J. Plast 154 (2022) 103302, https://doi.org/10.1016/j.ijplas.2022.103302.
[59] Y. Hou, J.Y. Min, H.-R. Lee, J.J. Ha, N. Park, M.-G. Lee, A generalized, computationally versatile plasticity model framework - part II: theory and verification focusing on shear anisotropy, Int. J. Plast 183 (2024) 104158, https://doi.org/10.1016/j.ijplas.2024.104158.
[60] L. Sun, K. Du, Y.Q. Ren, Y. Hou, J.Q. You, L. Dong, L. Zhang, H.R. Dong, X.Q. Li, X. G. Yuan, A new coupled yield criterion focusing on the precise description of anisotropic behavior under broader stress states: modeling, validation, and convexity analysis, Int. J. Solids Struct. (2025) 113251, https://doi.org/10.1016/j.ijsolstr.2025.113251.
[61] K. Du, J.H. Cui, Y. Hou, Y.Q. Ren, J.Q. You, L. Ying, X.Q. Li, X.J. Zuo, H.J. Huang, X.G. Yuan, Breaking through the plasticity modeling limit in plane strain and shear loadings of sheet metals by a novel additive-coupled analytical yield criterion, J. Mater. Sci. Technol. 225 (2025) 261–276, https://doi.org/10.1016/j.jmst.2024.12.003.
[62] Y. Hou, J.Y. Min, N. Guo, J.P. Lin, J.E. Carsley, T.B. Stoughton, H. Traphöner, T. Clausmeyer, A.E. Tekkaya, Investigation of evolving yield surfaces of dual-phase steels, J. Mater. Process. Technol. 287 (2021) 116314, https://doi.org/10.1016/j.jmatprotec.2019.116314.
[63] F.W. Sun, S.X. Wang, Q.G. Xie, Role of particles and lattice rotation in tension–compression asymmetry of aluminium alloys, Int. J. Plast 159 (2022) 103464, https://doi.org/10.1016/j.ijplas.2022.103464.
[64] P.F. Wu, Q. Chen, L.C. Zhou, X.Q. Liang, Y.S. Lou, Analytical model to characterize temperature-dependent anisotropic-asymmetric behavior of mg-gd-Y alloy, J. Magnesium Alloys (2024) S2213956724003943, https://doi.org/10.1016/j.jma.2024.11.035.
[65] A.S. Khan, S.J. Yu, Deformation induced anisotropic responses of ti–6Al–4V alloy. Part I: experiments, Int. J. Plast 38 (2012) 1–13, https://doi.org/10.1016/j.ijplas.2012.03.015.
[66] C. Ghnatios, O.A.N. Cazacu, B. Revil-Baudard, F. Chinesta, A new methodology for anisotropic yield surface description using model order reduction techniques and invariant neural network, J. Mech. Phys. Solids 184 (2024) 105542, https://doi.org/10.1016/j.jmps.2024.105542.
[67] G. Joo, H. Huh, M.K. Choi, Tension/compression hardening behaviors of auto-body steel sheets at intermediate strain rates, Int. J. Mech. Sci. 108–109 (2016) 174–187, https://doi.org/10.1016/j.ijmecsci.2016.01.035.
[68] Y.F. Yang, Z.R. He, J. Ma, H. Yang, J.Y. Min, S.L. Zang, H. Li, Evolving asymmetric and anisotropic hardening of CP-ti sheets under monotonic and reverse loading: characterization and modeling, Int. J. Plast 159 (2022) 103445, https://doi.org/10.1016/j.ijplas.2022.103445.
[69] Y.S. Lou, H. Huh, J.W. Yoon, Consideration of strength differential effect in sheet metals with symmetric yield functions, Int. J. Mech. Sci. 66 (2013) 214–223, https://doi.org/10.1016/j.ijmecsci.2012.11.010.

[70] O. Cazacu, A criterion for description of anisotropy and yield differential effects in pressure-insensitive metals, Int. J. Plast 20 (2004) 2027–2045, https://doi.org/10.1016/j.ijplas.2003.11.021.
[71] Q. Hu, X.F. Li, X.H. Han, H. Li, J. Chen, A normalized stress invariant-based yield criterion: modeling and validation, Int. J. Plast 99 (2017) 248–273, https://doi.org/10.1016/j.ijplas.2017.09.010.
[72] B. Plunkett, O. Cazacu, F. Barlat, Orthotropic yield criteria for description of the anisotropy in tension and compression of sheet metals, Int. J. Plast 24 (2008) 847–866, https://doi.org/10.1016/j.ijplas.2007.07.013.
[73] O.A.N. Cazacu, B. Plunkett, F. Barlat, Orthotropic yield criterion for hexagonal closed packed metals, Int. J. Plast 22 (2006) 1171–1194, https://doi.org/10.1016/j.ijplas.2005.06.001.
[74] N. Park, T.B. Stoughton, J.W. Yoon, A criterion for general description of anisotropic hardening considering strength differential effect with non-associated flow rule, Int. J. Plast 121 (2019) 76–100, https://doi.org/10.1016/j.ijplas.2019.04.015.
[75] Y. Zhou, Q. Hu, J. Chen, A concise analytical framework for describing asymmetric yield behavior based on the concept of shape functions, Int. J. Plast 164 (2023) 103593, https://doi.org/10.1016/j.ijplas.2023.103593.
[76] Y. Hou, K. Du, J.Y. Min, H.-R. Lee, Y.S. Lou, N. Park, M.-G. Lee, A generalized, computationally versatile plasticity model framework - part I: theory and verification focusing on tension–compression asymmetry, Int. J. Plast 171 (2023) 103818, https://doi.org/10.1016/j.ijplas.2023.103818.
[77] S. Soare, J.W. Yoon, O.A.N. Cazacu, On the use of homogeneous polynomials to develop anisotropic yield functions with applications to sheet forming, Int. J. Plast 24 (2008) 915–944, https://doi.org/10.1016/j.ijplas.2007.07.016.
[78] J.Y. Min, J.E. Carsley, J.P. Lin, Y.Y. Wen, B. Kuhlenkötter, A non-quadratic constitutive model under non-associated flow rule of sheet metals with anisotropic hardening: modeling and experimental validation, Int. J. Mech. Sci. 119 (2016) 343–359, https://doi.org/10.1016/j.ijmecsci.2016.10.027.
[79] Q. Hu, J.W. Yoon, Analytical description of an asymmetric yield function (Yoon2014) by considering anisotropic hardening under non-associated flow rule, Int. J. Plast 140 (2021) 102978, https://doi.org/10.1016/j.ijplas.2021.102978.
[80] S. Soare, F. Barlat, Convex polynomial yield functions, J. Mech. Phys. Solids 58 (2010) 1804–1818, https://doi.org/10.1016/j.jmps.2010.08.005.
[81] R. Uppaluri, D. Helm, A convex fourth order yield function for orthotropic metal plasticity, Eur. J. Mech. A Solids 87 (2021) 104196, https://doi.org/10.1016/j.euromechsol.2020.104196.
[82] W. Tong, An improved method of determining gotoh's nine material constants for a sheet metal with only seven or less experimental inputs, Int. J. Mech. Sci. 140 (2018) 394–406, https://doi.org/10.1016/j.ijmecsci.2018.03.018.
[83] C. Raemy, N. Manopulo, P. Hora, On the modelling of plastic anisotropy, asymmetry and directional hardening of commercially pure titanium: a planar fourier series based approach, Int. J. Plast 91 (2017) 182–204, https://doi.org/10.1016/j.ijplas.2017.02.010.
[84] Y.S. Lou, C. Zhang, P.F. Wu, J. Whan Yoon, New geometry-inspired numerical convex analysis method for yield functions under isotropic and anisotropic hardenings, Int. J. Solids Struct. 286–287 (2024) 112582, https://doi.org/10.1016/j.ijsolstr.2023.112582.
[85] Y. Hou, J.Y. Min, T.B. Stoughton, J.P. Lin, J.E. Carsley, B.E. Carlson, A non-quadratic pressure-sensitive constitutive model under non-associated flow rule with anisotropic hardening: modeling and validation, Int. J. Plast 135 (2020) 102808, https://doi.org/10.1016/j.ijplas.2020.102808.
[86] H.W. Liu, T. Jin, J. Qiu, L.T. Li, X.F. Shu, X. Li, Anisotropic constitutive modeling with the considerations of two strategies in describing the distorted hardening of AA6061 under tension-dominated loading conditions, J. Mater. Res. Technol. 29 (2024) 571–588, https://doi.org/10.1016/j.jmrt.2024.01.130.
[87] H.B. Wang, M. Wan, X.D. Wu, Y. Yan, The equivalent plastic strain-dependent Yld2000-2d yield function and the experimental verification, Comput. Mater. Sci 47 (2009) 12–22, https://doi.org/10.1016/j.commatsci.2009.06.008.
[88] S.C. Soare, A parameter identification scheme for the orthotropic Poly6 yield function satisfying the convexity condition, Eur. J. Mech. A Solids 92 (2022) 104467, https://doi.org/10.1016/j.euromechsol.2021.104467.
[89] K. Du, S.H. Huang, Y. Hou, H.B. Wang, Y.X. Wang, W.T. Zheng, X.G. Yuan, Characterization of the asymmetric evolving yield and flow of 6016-T4 aluminum alloy and DP490 steel, J. Mater. Sci. Technol. 133 (2023) 209–229, https://doi.org/10.1016/j.jmst.2022.05.040.